IVW - Schriftenreihe Band 101
Institut für Verbundwerkstoffe GmbH - Kaiserslautern

Lars Moser

Experimental Analysis and Modeling of Susceptorless Induction Welding of High Performance Thermoplastic Polymer Composites

Bibliografische Information Der Deutschen Bibliothek

Die Deutsche Bibliothek verzeichnet diese Publikation in der Deutschen Nationalbibliografie; detaillierte bibliografische Daten sind im Internet über <http://dnb.ddb.de> abrufbar.

Bibliographic information published by Die Deutsche Bibliothek

Die Deutsche Bibliothek lists this publication in the Deutsche Nationalbibliografie; detailed bibliographic data is available in the Internet at <http://dnb.ddb.de>.

Herausgeber: Institut für Verbundwerkstoffe GmbH
Prof. Dr.-Ing. Ulf Breuer
Erwin-Schrödinger-Straße
TU Kaiserslautern, Gebäude 58
67663 Kaiserslautern
http://www.ivw.uni-kl.de

Verlag: Institut für Verbundwerkstoffe GmbH

Druck: Technische Universität Kaiserslautern
ZBT – Abteilung Foto-Repro-Druck

D 386

Als Manuskript gedruckt. Printed in Germany.
ISSN 1615-021X
ISBN 978-3-934930-97-1

Experimental Analysis and Modeling of Susceptorless Induction Welding of High Performance Thermoplastic Polymer Composites

Vom Fachbereich Maschinenbau und Verfahrenstechnik

der Technischen Universität Kaiserslautern

zur Erlangung des akademischen Grades

Doktor-Ingenieur (Dr.-Ing.)

genehmigte

Dissertation

von

Herrn

Dipl.-Ing. Lars Moser

aus Gifhorn

Tag der mündlichen Prüfung: 14. Mai 2012

Prüfungsvorsitzender:	Prof. Dr.-Ing. Jan C. Aurich
1. Berichterstatter:	Prof. Dr.-Ing. Peter Mitschang
2. Berichterstatter:	Prof. Dr.-Ing. Paul L. Geiß

Preface

I would like to express deep gratitude to my supervisor Prof. Dr.-Ing. Peter Mitschang. His guidance, motivation, and continuous support were invaluable for my professional and personal development and the successful completion of this thesis.

I am indebted to the members of the examination commission Prof. Dr.-Ing. Paul L. Geiß for the co-reference of my thesis and Prof. Dr.-Ing. Jan C. Aurich for accepting the chairmanship of the examination committee.

My special thanks go to Dr. Ali Yousefpour for providing me the opportunity of a research stay at the National Research Council of Canada. His mentoring and support is greatly acknowledged.

I would like to express my gratitude to all the colleagues at IVW who contributed to this research work. Special thanks go to Dr. Rudi Velthuis for introducing me to induction welding and Dr. Miro Duhovic for his input on modeling issues, time and effort spent on correcting the manuscript, but most importantly for being a close friend. A big thank you goes to Sven Hennes for his assistance. I would like to thank René Holschuh, Mirja Didi, Klaus Hildebrandt, Angelos Miaris, Marcel Christmann, Michael Bierer, Zdravka Rasheva, Dr. Lada Gyurova, Dr. Thomas Bayerl and Dr. Nicole Knör for their friendship and the time we shared both at work and in private.

I would like to thank the partners of the research projects “Induflex” and “Instrukt”. The financial support of Bundesminsterium für Bildung und Forschung (BMBF), Bundesministerium for Wirtschaft und Technologie (BMWi) and Deutscher Akademischer Austauschdienst (DAAD) is greatly acknowledged.

Finally, I would like to thank my family, who always devotedly supported me over the years. There are no words to thank my fiancée Susanne for her incredible love, patience, and support.

Kaiserslautern, June 2012

Table of Contents

Abbreviations and Symbols

Abbreviation	*Description*
CF	Carbon fiber
CF/PEEK	Carbon fiber reinforced polyetheretherketone
CF/PPS	Carbon fiber reinforced polyphenylenesulfide
PEEK	Polyetheretherketone
PPS	Polyphenylenesulfide
RT	Room temperature
UD	Unidirectional

Symbol	*Unit*	*Description*
a	m	Length
A	V·s/m	Magnetic vector potential
A_f	m^2	Cross-sectional area of fiber
A_w	m^2	Overlap weld area
b	m	Width
B	T	Magnetic flux density
c_p	J/(kg·K)	Heat capacity at constant pressure
d_f	m	Fiber diameter
D	A·s/ m^2	Electric flux density
D_{ic}		Degree of intimate contact
D_n	m	Nozzle diameter
E	V/m	Electric field intensity
E_e	J	Electrical energy
f	Hz	Frequency
F_{max}	N	Force at failure

g^*		Geometric parameter
Gr		Grashof number
h	W/(m^2·K)	Heat transfer coefficient
$\bar{h}$	W/(m^2·K)	Averaged heat transfer coefficient
h_f	m	Height of vertical face
H	A/m	Magnetic field intensity
H_{sd}	m	Standoff distance of nozzle
H_{surf}	A/m	Magnetic field intensity at surface
i		Interception
j	A/m^2	Induced current density
J	A/m^2	Current density
J_0	A/m^2	Current density at workpiece surface
J_e	A/m^2	External current density
k	W/(m·K)	Thermal conductivity
$k_{f\parallel}$	W/(m·K)	Thermal conductivity parallel to fiber axis
$k_{f\infty}$	W/(m·K)	Thermal conductivity perpendicular to fiber axis
k_m	W/(m·K)	Thermal conductivity of matrix
k_x	W/(m·K)	Thermal conductivity of composite in x-direction
k_y	W/(m·K)	Thermal conductivity of composite in y-direction
k_z	W/(m·K)	Thermal conductivity of composite in z-direction
l	m	Characteristic length
l_f	m	Fiber length
m		Curve slope
Nu		Nusselt number
p_o	W/m^2	Surface power density
p_{app}	Pa	Applied pressure

P_f	W	Heat generation along a fiber
Pr		Prantl number
P_w	W	Workpiece power
q	W/m^2	Heat flux
q_0	W/m^2	Heat flux entering the domain
Q	W/m^3	Heat source
r	m	Radius
r_{cp}	m	Distance between conductor and a point
R	Ω	Electrical resistivity
Re		Reynolds number
Re_{SRN}		Reynolds number of single round nozzle
R_f	Ω	Electrical resistance of fiber
R_{jc}	Ω	Contact resistance at fiber junctions
R_{jd}	Ω	Junction dielectric impedance
s	m	Curve element
t	s	Time
t_{ic}	s	Time to reach intimate contact
T	°C	Temperature
T_0	°C	Surface temperature
T_∞	°C	Fluid temperature outside boundary layer
T_{amb}	°C	Ambient temperature
T_g	°C	Glass transition temperature
Ti_{nf}	°C	Temperature far away from the modeled domain and the heat transfer coefficient
T_m	°C	Mean fluid temperature
T_{melt}	°C	Melting temperature

T_N	°C	Nozzle temperature
T_s	°C	Surface temperature
T_w	°C	Welding temperature
$T_{w,\ PEEK}$	°C	Welding temperature of PEEK
$T_{w,\ PPS}$	°C	Welding temperature of PPS
u	m/s	Velocity
u_{ind}	V	Induced voltage
V_f	V	Voltage across a fiber
w	m/s	Fluid velocity
x	m	Distance
y	m	Distance to surface
α	m^2/s	Thermal diffusivity
α_{te}	K^{-1}	Coefficient of thermal expansion
β	K^{-1}	Volumetric thermal expansion coefficient
δ	m	Penetration depth
ε	F/m	Relative electric permittivity
ε_e		Emissivity
λ	m	Wavelength
κ		Relative dielectric constant
v	Pa·s	Dynamic viscosity of fluid
ρ	kg/m^3	Density
ρ_{cd}	A·s	Electric charge density
σ	S/m	Electrical conductivity
σ_x	S/m	Electrical conductivity of composite in x-direction
σ_y	S/m	Electrical conductivity of composite in y-direction
σ_f	S/m	Electrical conductivity of fiber

σ_m	S/m	Electrical conductivity of matrix
τ_{max}	MPa	Maximum shear tensile strength
Φ		Fiber volume content
Φ_{fx}		Fiber volume content in x-direction
Φ_{fy}		Fiber volume content in y-direction
η	Pa·s	Viscosity of matrix-fiber system
μ	H/m	Magnetic permeability
μ_r	H/m	Relative magnetic permeability
μ_{surf}	H/m	Relative magnetic permeability at surface
ω	rad/s	Angular frequency
∇		Differential operator
$\Delta\rho_{max}$	K	Maximum difference in density
ΔT_s	K	Difference in surface temperature
$\Delta T_{s,max}$	K	Maximum difference in surface temperature
tanδ		Dissipation factor

Constant	*Value*	*Description*
c	299792458 m/s	Speed of light in vacuum
g	9.80665 m/s^2	Acceleration of gravity
ε_0	$8.85 \cdot 10^{-12}$	Relative electric permittivity of vacuum
μ_0	$4 \cdot \pi \cdot 10^{-7}$ H/m	Permeability of free space

Kurzfassung

Das Induktionsschweißen ist ein Verfahren zum Fügen von thermoplastischen Faser/Kunststoff-Verbunden. Mittels eines elektromagnetischen Wechselfeldes wird die zum Schweißen notwendige Energie berührungslos und schnell in die zu verbindenden Bauteile eingebracht. Bei Vorliegen einer geeigneten Verstärkungsstruktur erfolgt die Wärmeerzeugung direkt im Laminat. Dabei ist das Temperaturfeld durch eine vollständige Erwärmung in Dickenrichtung im Bereich unterhalb der Induktionsspule gekennzeichnet. Die resultierende Temperatur wird durch den Abstand zum Induktor beeinflusst, wobei die Temperatur mit steigendem Abstand abnimmt. Daraus folgt, dass in der dem Induktor zugewandten Seite die höchsten und auf der gegenüberliegenden Seite des Laminates die niedrigsten Temperaturen auftreten.

Das beschriebene Temperaturfeld erschwert den Schweißprozess erheblich. Aufgrund der Durchwärmung muss das Laminat zur Vermeidung von Delaminationen mit Druck beaufschlagt werden, was den Einsatz von komplexen und teuren Schweißvorrichtungen nötig macht. Zudem kann die Temperaturdifferenz zwischen Induktorseite und gegenüberliegender Seite größer als das durch die Eigenschaften des Matrixpolymers vorgegebene Prozessfenster sein.

Der Induktionsschweißprozess wird durch eine Vielzahl von Parametern bestimmt. Aufgrund der Komplexität erfolgt die Prozessentwicklung im Wesentlichen auf Basis experimenteller Studien. Untersuchungen zu Parametereinflüssen und Wechselwirkungen sind somit aufwändig und die Messung von qualitätsrelevanten Parametern, insbesondere in der Fügezone, ist schwierig. Die Prozesssimulation kann dazu beitragen, den Aufwand von Parameterstudien zu verringern und den Induktionsschweißprozess weiter zu analysieren.

Ziel der vorliegenden Arbeit ist die Entwicklung einer Verfahrensvariante des Induktionsschweißens ohne vollständige Durchwärmung des Laminats in Dickenrichtung. Für einen optimalen Schweißprozess muss die Fügezone auf Schweißtemperatur erwärmt werden, während die übrigen Bereiche zur Vermeidung von Delaminationen die Schmelztemperatur des Matrixpolymers nicht überschreiten sollten.

Zur Beeinflussung der Temperaturverteilung wurde eine lokale Kühlung an der dem Induktor zugewandten Seite mittels Druckluftprallströmung realisiert. Zur Beurteilung der Wirkungsweise wurden statische Aufheizversuche an kohlenstofffaserverstärkten

Polyetheretherketon- (CF/PEEK) und Polyphenylensulfid-Laminaten (CF/PPS) durchgeführt.

Durch den Einsatz der lokalen Kühlung konnte die Temperaturverteilung in Dickenrichtung des Laminats an die Erfordernisse des Schweißprozesses angepasst werden. Das Temperaturmaximum wurde von der Induktorseite auf die gegenüberliegende Seite verlagert. Dies ermöglicht die Erwärmung auf Schweißtemperatur in der Fügezone und verhindert gleichzeitig das Aufschmelzen und die damit verbundenen Effekte in den außenliegenden Bereichen.

Die induktive Erwärmung sowie die Verfahrensvariante mit lokaler Kühlung wurden in dreidimensionalen Prozessmodellen mit Hilfe der Finite-Elemente-Methode abgebildet. Hierfür wurden mit der Software Comsol Multiphysics 4.1 vollständig gekoppelte elektromagnetische-thermische Modelle entwickelt und experimentell validiert. In einer Sensitivitätsanalyse wurde der Einfluss von verschiedenen Prozessparametern auf die induktive Erwärmung analysiert. Dabei wurden der Spulenstrom, die Feldfrequenz sowie die Wärmekapazität als signifikante Parameter identifiziert. Die Kühlwirkung der Prallströmung wurde dabei mittels angepasster Konvektionskoeffizienten realisiert.

Zur Übertragung der entwickelten Prozessvariante der induktiven Erwärmung auf den kontinuierlichen Induktionsschweißprozess wurde ein entsprechendes Prozessmodel erstellt. Dieses bildet die Erwärmung einer einfach überlappten Schweißnaht bei kontinuierlichem Vorschub ab. Mit Hilfe der Prozesssimulation wurde ein zum Verschweißen von CF/PEEK geeigneter Parametersatz ermittelt und zur Herstellung von Schweißproben verwendet. Dabei konnte das zum Schweißen optimale Temperaturprofil eingestellt und ein Aufschmelzen der Außenschicht verhindert werden.

Abstract

Induction welding is a technique for joining of thermoplastic composites. An alternating electromagnetic field is used for contact-free and fast heating of the parts to be welded. In case of a suitable reinforcement structure heat generation occurs directly in the laminate with complete heating in thickness direction in the vicinity of the coil. The resulting temperature field is influenced by the distance to the induction coil with decreasing temperature for increasing distance. Consequently, the surface facing the inductor yields the highest, the opposite surface the lowest temperature.

The temperature field described significantly complicates the welding process. Due to complete heating the laminate has to be loaded with pressure in order to prevent delamination, which requires the usage of complex and expensive welding tools. Additionally, the temperature difference between the inductor and the opposite side may be greater than the processing window, which is determined by the properties of the matrix polymer.

The induction welding process is influenced by numerous parameters. Due to complexity process development is mainly based on experimental studies. The investigation of parameter influences and interactions is cumbersome and the measurement of quality relevant parameters, especially in the bondline, is difficult. Process simulation can reduce the effort of parameter studies and contribute to further analysis of the induction welding process.

The objective of this work is the development of a process variant of induction welding preventing complete heating of the laminate in thickness direction. For optimal welding the bondline has to reach the welding temperature whereas the other domains should remain below the melting temperature of the matrix polymer.

For control of the temperature distribution localized cooling by an impinging jet of compressed air was implemented. The effect was assessed by static heating experiments with carbon fiber reinforced polyetheretherketone (CF/PEEK) and polyphenylenesulfide (CF/PPS).

The application of localized cooling could influence the temperature distribution in thickness direction of the laminate, according to the specifications of the welding process. The temperature maximum was shifted from the inductor to the opposite

side. This enables heating of the laminate to welding temperature in the bondline and concurrently preventing melting and effects connected to this on the outer surface.

Inductive heating and the process variant with localized cooling were implemented in three-dimensional finite-element process models. For that purpose, the finite-element-software Comsol Multiphysics 4.1 was used for the development of fully coupled electromagnetic-thermal models which have been validated experimentally. A sensitivity analysis for determination of different processing parameters of inductive heating was conducted. The coil current, field frequency, and heat capacity were identified as significant parameters. The cooling effect of the impinging jets was estimated by appropriate convection coefficients.

For transfer of the developed process variant to the continuous induction welding process, a process model was created. It represents a single overlap joint with continuous feed. With the help of process modeling a parameter set for welding of CF/PEEK was determined and used for joining of specimens. In doing so, the desired temperature field was achieved and melting of the outer layers could be prevented.

1. Introduction

Composites are a class of engineering materials used in a broad range of applications. Furthermore, they can be considerably tailored to suit the service condition [1]. They offer high specific properties and enable new designs for lightweight construction. Continuously reinforced composites are suitable for numerous applications, e.g. in aerospace, automotive, construction, or engineering. Their use has significantly increased in the past decades. As an example, the percentage of composites in Airbus commercial airplanes has grown from less than five percent in the A300 [2] to more than twenty in the A380 and will exceed fifty percent in the anticipated A350-900 XWB [3], allowing for a weight reduction of 20 % [4].

Manufacturing costs for composite structures are higher compared metallic ones [5]. One reason is the complicated and time costly lay-up of thermoset prepregs and subsequent curing for several hours in the autoclave that covers approximately 80 – 90 % of composites manufacturing at Airbus [5]. Therefore, the manufacturing challenge is to enable high volume production, including short cycle times and high production rates [4].

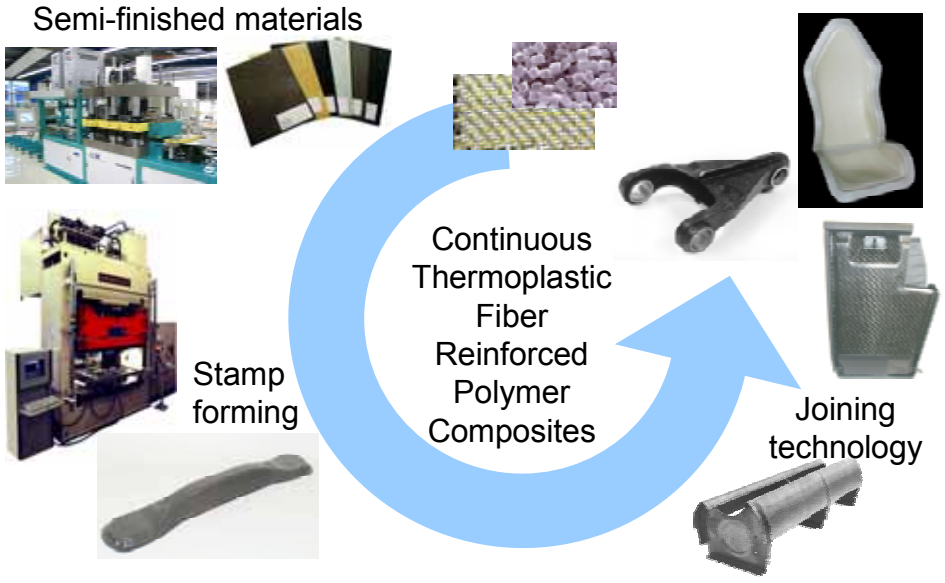

Figure 1: Processing chain for continuously reinforced thermoplastic composites [7]

A processing chain capable of mass production, which enables cost-effective processing and reduced part cost, can be realized by the use of thermoplastic polymer composites [6-8], see Figure 1. Separating the time consuming impregnation step

from the following forming steps (e. g. thermoforming or shaping and joining) allows for short cycle times and high throughput [7].

Because of the limited formability of continuously reinforced thermoplastic composites, complex geometries cannot be efficiently produced and consequently joining operations are necessary for the manufacture of large and complex structures [9,10]. This is due to the inability of continuous fiber reinforcement to stretch in the fiber direction [11], making intraply shear the dominant deformation mechanism for fabric reinforced thermoplastic composites [12].

Established traditional joining technologies for metallic structures, such as mechanical fastening, are not directly transferrable to composites [13,14].

Typical problems include:

- Stress concentrations around holes and cut-outs caused by the lack of plasticity and limited stress redistribution, respectively [13,15]
- Delamination caused by drilling operations [16]
- Added weight due to fastening system [16]
- Temperature induced stresses caused by differential thermal expansion of fasteners and composite [17]
- Possible galvanic corrosion at joints [17]
- Extensive surface preparation and curing times in the case of adhesive bonding [15,18]

Fusion bonding, or welding, is a technique ideally suited for the joining of thermoplastic composites [19] and can eliminate the described problems [20]. It takes advantage of the reprocessability of thermoplastic composites [21]. It is characterized by local melting and reconsolidation of two or more parts at a common interface [13,19] and is capable of producing joints with strength close to the parent material [14]. It enables joining without foreign material at the interface, which increases the long-term integrity of the joint [22], can reduce manufacturing cost [23,24] and is widely considered as an ideally suited technique for the joining of thermoplastic composites [25]. Fusion bonding is expected to replace traditional techniques like the ones mentioned beforehand [24].

Numerous technologies are available for melting the bondline [15,24,26,27]. However, amongst processes such as ultrasonic and resistance welding, induction welding is one of the joining methods being considered to be most suitable for thermoplastic composites [25,28]. It offers advantages such as rapid heating of the laminate to its melting temperature within seconds, heat input directly to the laminate, low thermal inertia, and contact-free localized heating [23,29,30]. Applied as a heat source for welding, it provides great flexibility [31] and is especially suited for long and thin structures [28].

Relative movement between the workpiece and the inductor is used to create a continuous welding process; possible setups include moving platforms [25,31] or automated handling systems such as industrial robots [32,33].

However, the primary advantage of induction welding is the ability of process automation [33]. In susceptorless welding, no foreign auxiliary materials such as heating elements (resistance welding) or energy directors (ultrasonic welding) are needed, which has proven to be the major drawback for those processes. An example is the use of resistance welding in series production of the J-nose for Airbus A340-500/600 and A380-800. In this case, it appeared to be too expensive to manufacture welding stripes comprising the heating element with the required quality at an industrial scale [33].

1.1. Objective

The nature of susceptorless induction welding implies heating through-the-thickness of the laminate in proximity of the induction coil [15,28]. In many cases this is an unwanted effect as it counteracts one of the most appealing characteristics of welding, i. e. localized heating only in the bondline. This significantly complicates the welding process and requires pressure application throughout the process. In order to retain the shape of complex structural parts rather sophisticated pressurized tools have to be used which are accordingly expensive to manufacture. As an example, the welding jig for the production of the Gulfstream G650 rudder torsion box is given in Figure 2.

Figure 2: Induction weld robot and weld jig for Gulfstream G650 rudder torsion box [33,34]

In contrast to the example given in Figure 2, the use of rollers for consolidation is very flexible because a generic welding device can be used for different parts and relatively simple tools suffice for fixation of the workpiece [35,36]. Though, compared to the areal pressure application of a complex jig, the pressure application of a roller system is reduced to a line contact, which makes pressure application and conservation of the original geometry extremely difficult and impedes using this approach for serial production.

In order to combine the advantages of both techniques, an enhanced induction welding process controlling the through-the-thickness heating and limiting melting of the laminate to the bondline has to be developed. This enables usage of comparably economic and very flexible generic welding units for the manufacture of complex components.

Due to the complex nature of the induction heating process and processing conditions for fusion bonding, process design is predominantly based on experimental work. This is expensive, time-consuming, and cumbersome. Parameter interactions are difficult to measure and complicate the assessment of experimental results.

Modeling can be a viable tool for better understanding of the process characteristics and improving the process design of induction welding. Three-dimensional process models enable analysis of the spatial temperature distribution. Inductor design, which is often developed on an empirical basis, can also be improved. Process optimization and assessment of the significance of the parameters involved in the process can be achieved fast and in a very cost efficient way.

The objectives of this study are to:

- Characterize the heating behavior of high performance carbon fiber reinforced polyphenylenesulfide and polyetheretherketone composites
- Introduce an enhanced processing technique controlling the through-the-thickness heating and limiting melting of the laminates to the bondline.
- Develop fully coupled electromagnetic and thermal finite element models of the induction heating process and the enhanced processing technique
- Describe the significance of processing parameters
- Outline a continuous induction welding process that avoids unwanted through-the-thickness heating
- Give a proof of concept of the novel continuous induction welding process

1.2. Approach

Chapter 2 summarizes the state of the art in induction welding of carbon fiber reinforced thermoplastic polymers. Starting from the basics of the fusion bonding process and induction heating, selected aspects relevant to the objectives above are discussed. Furthermore, fundamentals for modeling the process, focusing on the heating step, are presented.

Chapter 3 contains the experimental part of this work. The materials and experimental procedures used for induction heating and welding experiments, respectively, are explained. The heating behavior of polyetheretherketone and polyphenylenesulfide with satin 5 harness reinforcement is characterized.

In Chapter 4, a heating process utilizing localized surface cooling for through-the-thickness temperature control of the laminates is introduced and characterized.

Chapter 5 describes the development and validation of fully coupled electromagnetic/thermal three-dimensional induction heating process models using the commercial FEM package Comsol Multiphysics. A sensitivity analysis gives insight into the significance of the most important input parameters. Thereafter, a process model of the enhanced induction heating process is developed.

In Chapter 6, a three-dimensional process model of an enhanced continuous induction welding process preventing thermal damages is developed. Based on the model, a parameter set is determined and CF/PEEK laminates are welded in a single over-

lap configuration. The resulting joint is characterized by tensile tests, fracture surface analysis and cross-sectional analysis.

Chapter 7 summarizes the main achievements of this work and gives suggestions for further development of the induction welding process.

2. State of the Art

2.1. Fusion Bonding

Fusion bonding of thermoplastic composites is a process of welding two or more components by localized heating and consolidation at their common interface [15,27]. Usually, the resulting quality is comparable to co-consolidated or compression molded parts [24]. The process can be divided into five steps [28] that can either occur sequentially or simultaneously [27]. These steps of surface preparation, heating, pressing, intermolecular diffusion, and cooling [27,28], are explained in more detail below.

2.1.1. Surface Preparation

Surface preparation is commonly the first step in composites welding and typically involves machining or cleaning [11,27]. The first may be necessary to ensure geometrical fit of the parts to be joined whereas the latter is often used for removal of chemical contaminants [27]. Welding of thermoplastic composites seems to have a tolerance towards contaminations. Compared to thermoset adhesives the surface preparation is less critical [37]. Experiments with release agents showed that small amounts of silicone contamination did not affect the quality of the bonds [28].

2.1.2. Heating

A variety of heating methods are available for welding of composites [15]. Often these methods are categorized by the heating mechanism [15,17,27], see Figure 3.

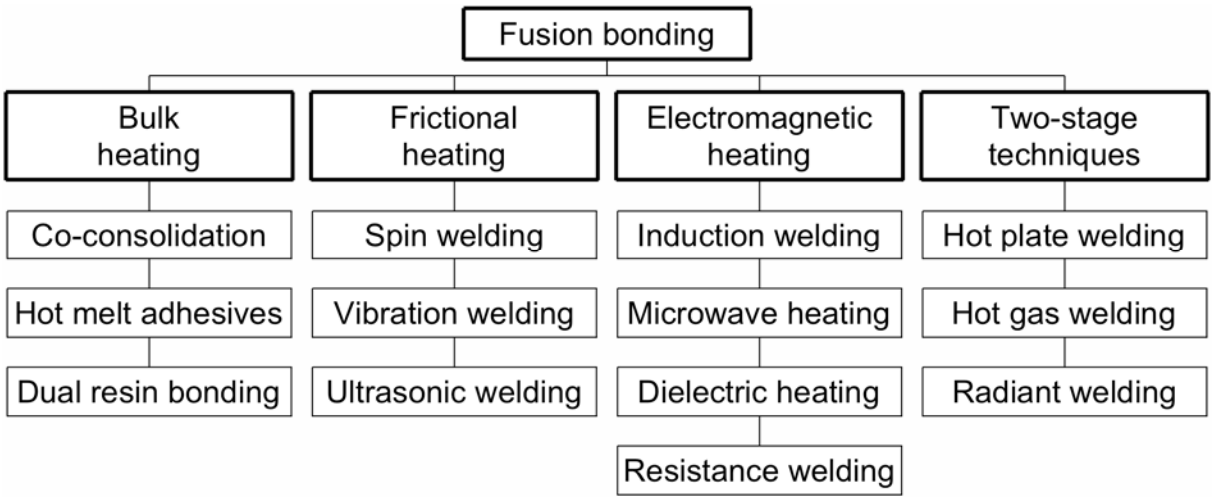

Figure 3: Categorization of fusion bonding techniques by heating mechanism [17]

Generally, the most attractive ones are those that enable local heating and melting of the thermoplastic matrix only in the vicinity of the bond [11]. The heating method applied influences the heating rate and therefore the welding speed and additionally the heat distribution in the bondline. From the categories listed above, see Figure 3, frictional heating yields the highest heating rates, shortest cycle times, and thinnest melt or softened layers [27]. The two-stage methods that use external heating show the lowest heating rates, long cycle times and thickest melt layers; whereas electromagnetic heating is characterized by medium heating rates, cycle times, and melt layer thickness, respectively [27].

2.1.3. Pressing

After heating of the bondline, intimate contact has to be established between the components to be welded. The contact area is reduced due to imperfections of contacting technical surfaces, see Figure 4, even in the molten or softened state, respectively [27].

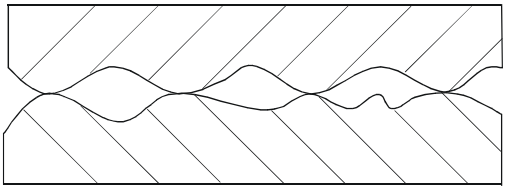

Figure 4: Schematic of two surfaces in contact [27]

In order to increase the contact area and maximize the quality of the joint, pressure is applied [27,28]. This can be divided into two phases: (i) First, surface asperities are deformed and intimate contact is developed. (ii) Thereafter, molten or softened matrix is squeezed out, displacing entrapped gases [27,28] and contaminated polymer [27]. The squeeze-out should occur as fast as possible during the welding process [27]. The presence of a resin rich layer may be beneficial for the matrix flow [28]. Consequently, reaching a low viscosity state is substantially important, especially for composites with high fiber volume contents [27]. This illustrates the importance of the heating step, since viscosity is temperature dependent. A resin rich surface or the application of additional polymer, e. g. in the form of film, may be beneficial to the formation of a polymer-polymer bond [28] because deformation and squeeze-out of neat resin can be achieved more easily compared to composites.

The effect of pressure and temperature on intimate contact generation can be assessed using consolidation process models, see [15,38,39] for an overview. According to [38] the formation of intimate contact can be described as Equation (1),

$$D_{ic} = g^* \left[\int_0^{t_c} \frac{p_{app}}{\eta} dt \right]^{\frac{1}{5}} \quad (1)$$

where D_{ic} is degree of intimate contact, g^* a geometric parameter representing the surface topology, t_c the contact time, p_{app} the applied pressure, and η the viscosity of the matrix-fiber system. Thermoplastic polymer melts normally exhibit viscoelastic behavior, but the assumption of a Newtonian fluid model is sufficient in most cases [27]. Intimate contact may be reached even for low consolidation pressures. However, this may imply relatively long times until intimate contact is reached. Figure 5 shows an example for the influence of the consolidation pressure on the formation of intimate contact for resistance welding of APC-2. In this study, a threshold of 1 MPa, resulting in less than approximately 200 s to reach intimate contact (t_{ic}), was recommended for this material system [40].

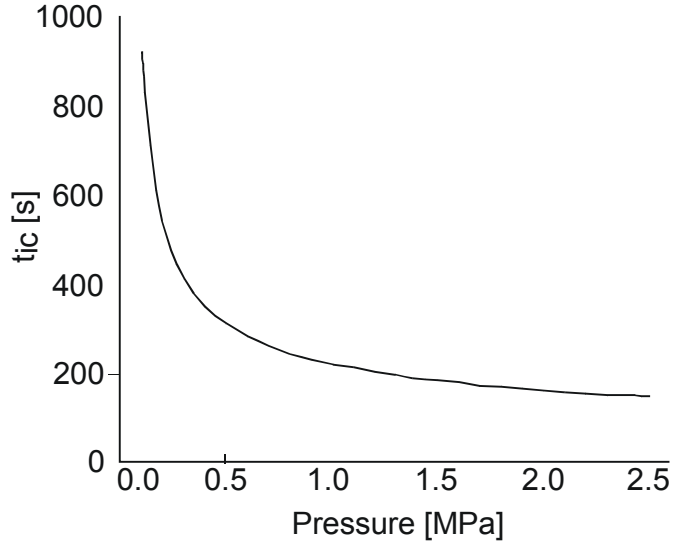

Figure 5: Time to achieve intimate (t_{ic}) contact versus consolidation pressure for an APC2 laminate/PEEK film lap-shear coupon [40]

2.1.4. Intermolecular Diffusion

After establishing intimate contact at the interface, intermolecular diffusion and entanglement of polymer chains is necessary to form the weld [27]. The interface gradually disappears and the mechanical strength at the polymer interface develops [11,15]. This process, which is referred to as autohesion can be divided into five dif-

ferent phases [41]: (i) Surface rearrangement, (ii) surface approach, (iii) wetting, (iv) diffusion, and (v) randomization. In welding, the first three phases are part of the pressing step whereas phases (iv) and (v) are parts of the diffusion step [27]. Under ideal conditions, the interface is not discernable from the bulk at the end of the process [42].

For amorphous thermoplastic polymers, intermolecular diffusion is possible at temperatures above T_g [27]. For semi-crystalline polymers T_{melt} has to be exceeded. Below this temperature no welding can be achieved because crystallites bind the molecules; whereas above T_{melt}, intermolecular diffusion is very rapid [27].

2.1.5. Cooling

Cooling is the final step in the fusion bonding process and the material undergoes resolidification. Amorphous polymers retain the molecular orientation previously obtained whereas semi-crystalline materials re-crystallize. Here, the cooling rate determines the crystallinity and the formation of spherulites in and near the weld [11,27] and will affect the solvent resistance and mechanical properties of the joint [15]. Thermally induced residual stresses and distortion may remain frozen in the component [27].

2.2. Theory of Induction Heating

Induction heating is a technology widely used in industry for a multitude of applications and the basic physics are comprehensively described in various references. [43-47]. Hence, only selected aspects will be covered here.

Heating of carbon fiber reinforced polymer composites occurs due to different mechanisms to varying degrees. Volumetric heat is generated dependent on the reinforcement type and the processing conditions [30]. Because of different electromagnetic phenomena, the current distribution is non-uniform within the inductor and the workpiece, resulting in temperature gradients in the workpiece [47].

2.2.1. Basic Concept

An induction coil connected to an alternating voltage will carry an alternating current in the coil that produces a time-variable magnetic field of the same frequency in its surrounding [47].

2.2.2. Estimation of Workpiece Power

The workpiece power P_w can be estimated as the product of the surface power density and the workpiece surface exposed to the magnetic field [47]. Precise calculation of the surface power density can only be obtained from numerical computations [47]; however, a rough estimation is given in Equation (2). For a magnetic body heated inside an infinitely long solenoid inductor the power surface density is proportional to the square of magnetic field intensity and the square root of the electrical resistivity, relative magnetic permeability, and the frequency, see Equation (2) [47],

$$p_0 \propto H_{surf}^2 \sqrt{R \mu_{surf} f} \tag{2}$$

where p_0 is surface power density, H_{surf} is magnetic field intensity at the surface, R is electrical resistivity, μ_{surf} is relative magnetic permeability at the surface, and f is frequency.

The magnetic field intensity **H** (which is not affected by the surrounding medium [48]) of a current carrying thin conductor can be calculated with the Biot-Savart law, see Equation (3) [49],

$$\boldsymbol{H} = \frac{I}{4\pi} \oint \frac{d\boldsymbol{s} \times \boldsymbol{r}_{\mathbf{cp}}}{\boldsymbol{r}_{\mathbf{cp}}^3} \tag{3}$$

where **H** is magnetic field intensity, I is current, d**s** is a curve element of the conductor, and $\mathbf{r_{cp}}$ is the distance between the conductor and a point. Relative magnetic permeability μ_r represents the ability of a material to conduct the magnetic flux in comparison to vacuum or air; relative permittivity ε represents the ability of a material to conduct the electric field in comparison to vacuum or air [47]. Relative magnetic permeability is a significant parameter for all basic induction heating phenomena, e. g. skin effect or edge effect whereas relative permittivity is not as important [47]. Relative magnetic permeability of non-magnetic materials such as carbon fiber reinforced thermoplastic composites is 1[1] [36,47]; relative permittivity of carbon fiber reinforced PEEK, which is assumed to be comparable to other carbon fiber reinforced high performance thermoplastic composites is 3.7 [51,52].

[1] Carbon fiber reinforced polymer composites are weakly diamagnetic with relative susceptiblity in the order of -10^{-7}. It can be assumed that the permeability of free space is applicable without significant loss in accuracy [50].

2.2.3. Skin Effect

When alternating current flows through a conductor, a non-uniform current distribution can be observed with the maximum located on the surface whereas the current density decreases from the surface towards the center of the component [47]. This phenomenon is also present in induction heating and referred to as skin effect, see Equation (4). The degree of skin effect, i. e. the characteristic depth of penetration, relates to the frequency and material properties electrical conductivity and magnetic permeability [43,45]. It describes the distance to the surface in normal direction, where the flux density drops to 1/e of its value at the surface [43,45],

$$\delta = \sqrt{\frac{1}{\pi f \mu_0 \mu_r \sigma}} \tag{4}$$

where f is field frequency,μ_0 is permeability of free space, μ_r is relative magnetic permeability, and σ is electrical conductivity.

The current density along a round workpiece thickness (radial direction) can be estimated by Equation (5) [47],

$$\boldsymbol{J} = \boldsymbol{J}_0 e^{\frac{y}{\delta}} \tag{5}$$

where J is current density at distance y from the surface, J_0 is current density at the workpiece surface, y is distance from the surface, and δ is penetration depth.

2.3. Induction Welding Process

The term induction welding of composites is used for a variety of process variants. Common advantages are contact-free, localized, and fast heating. However, the underlying heating mechanisms and electromagnetic parameters field frequency significantly differ from each other. Traditionally, it implies using a heating element, or susceptor, in order to dissipate the magnetic energy into thermal energy [53]. For joining, the susceptor is normally applied in the form of particles [53-58], weaves made from metal [53,59,60] allowing the resin to flow around the susceptor [53], or commingled carbon and polymer fibers [61].

Induction welding can be applied in both discontinuous (static) and continuous (moving) mode [31]. The first mode limits the weld design to the size of the coil whereas the latter one allows manufacturing of much larger joints by relative movement between the induction coil and the component.

2.3.1. Susceptorless Induction Heating

A problem inextricably linked with embedded susceptors is that they introduce stress concentrations and lower the possible strength, can cause wicking of moisture, are prone to corrosion, and increase the radar signature [53]. However, since carbon fibers are electrically conductive, they can be applied as the heating element [23,30,31,33,36,53,62-64], accepting that this implies complete heating of the composite [15,28].

A general condition for susceptorless induction heating is the availability of closed circuits of electrically conductive material [23,30,36,65]. This is fulfilled when the electrically conductive carbon fibers are either in direct electrical contact or are separated by a small gap of dielectric matrix [30]. A global current circuit of roughly the size of the coil is created within the material [23,65]. For this to occur, close proximity between adjacent plies is necessary [23]. Unidirectional laminates cannot be heated by induction because paths of sufficient electrical conductivity only exist along the fibers [23]. In a multi-ply non-unidirectional laminate the current has to be transferred between the layers in order to form the circuit.

Heating due to induced eddy currents occurs wherever a voltage drop is caused by electrical resistivity [30]. The internal heat generation mechanism is dependent on the architecture and the intrinsic properties of the carbon fiber reinforced polymer composite; this can either be in the fibers or at the junctions of adjacent fibers [30].

The electrical conductivity of carbon fibers is influenced by the type of precursor used for manufacturing and the heat treatment temperature [66]. Carbon fibers show semiconductor behavior regarding the resistivity [67,68], which results in an increase of electrical conductivity with temperature [68,69]. When characterizing polymer composites with continuous carbon fiber reinforcement the type of circuit has to be considered since DC conductivity of carbon fibers differs from the AC one, which may depend on frequency [66].

2.3.2. Influence of Induction Coil

In induction heating, coils must be designed according to the component geometry [23,44] as different coil shapes exhibit specific heating patterns [28,29,36]. Normally, an empirical approach is used in the development of induction heating coils [70].

However, due to the complexity of the problem, empirical methods are considered insufficient and a computer aided approach is necessary [23].

The coil tends to induce eddy currents mirroring its shape [36,63]. In carbon fiber reinforced composites, currents can only flow along electrically conductive paths, i. e. along carbon fibers, and the heating pattern may deviate from the expected shape [23]. The size of the global current loop is the coil or workpiece size, depending on which is smaller [23]. For woven reinforcements, fibers in the two directions are in good enough electrical contact to provide a network of electrically conductive paths, creating a mirror image of the coil [23].

For most induction welding applications usage of one coil, i. e. single-sided heating is necessary, even though one-sided coils are sensitive to variations in the coupling distance [23,35,36]. Due to their low thermal conductivity, composites sustain high thermal gradients and provide strong heat localization [23], especially in the thickness direction. Consequently, they cannot compensate for uneven heating patterns in the bondline [71].

2.3.3. Edge Effect

In induction heating of carbon fiber reinforced polymer composites an eddy current pattern similar to the applied inductor coil geometry is induced, flowing in a global current loop [23]. In the case of woven reinforcements with sufficient electrical contact between the carbon fibers currents can take zig-zag-paths, forming a mirror image of the coil [23].

If the coil size is larger than the material to be heated or the edges of the laminate are positioned close the coil; inhomogeneous heating is noticeable [23].

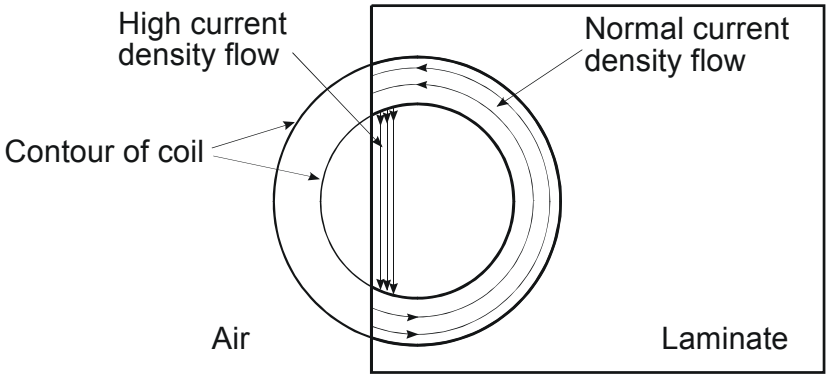

Figure 6: Edge effect in induction heating (schematic)

The reason for this effect is an uneven current distribution in the component. As the current flows in a global loop, there are high current densities in regions with small cross-sectional area and low current densities in regions with large cross-sectional area [23], see Figure 6. Due to the global current loop, both areas carry the same current, which results in a current density gradient. Since the temperature is proportional to the current density this results in an inhomogeneous temperature distribution.

2.3.4. Continuous Welding Process with Consolidation Rollers

The continuous induction welding process applies relative movement between the heating/consolidation unit and the workpiece, producing the weld. Figure 7 shows a two-dimensional setup with fixed coil, consolidation roller, moving platform, and the corresponding typical temperature graph measured below the surface [35]. The material passes below the coil and is subsequently charged with pressure. The temperature rises as the material is approaching the coil and the maximum temperature T_1 is reached. On the way from the heating position to the consolidation roller heat is transferred to the surrounding and jig by convection and conduction, respectively, and the laminate cools down to T_2. During consolidation heat is transferred from the laminate to the consolidation roller, lowering the laminate temperature to T_3. After passing the roller, the temperature rises up to T4, due to heat stored in the laminate. Table 1 summarizes the influencing parameters of the continuous process.

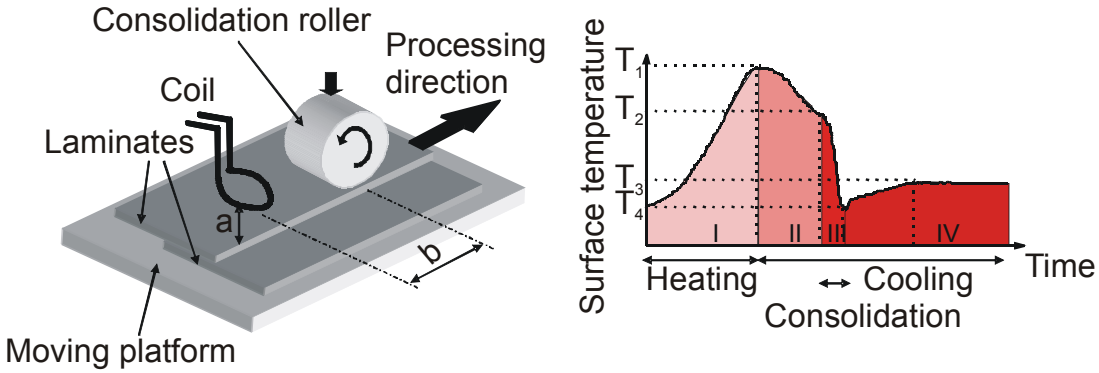

Figure 7: Continuous induction welding process scheme [35]

Table 1: Characteristic temperature and influencing factors in continuous induction welding [35]

Temperature	Description	Influencing parameters
T_1	Peak temperature	Generator power, frequency, coupling distance a, coil geometry, feed velocity, laminate
T_2	Roller contact temperature	Feed velocity, Distance from roller to coil b, welding jig
T_3	Temperature after roller contact	Roller temperature, Roller contact area, feed velocity
T_4	Steady state temperature	Feed velocity, cooling (if applicable)

Due to the generic design of the process, it is ideally suited for flexible production. As no part specific tools are used in the welding unit, it is capable of welding a variety of components in arbitrary order. Consequently the process has been adapted to a robotic induction welding system, see Figure 8.

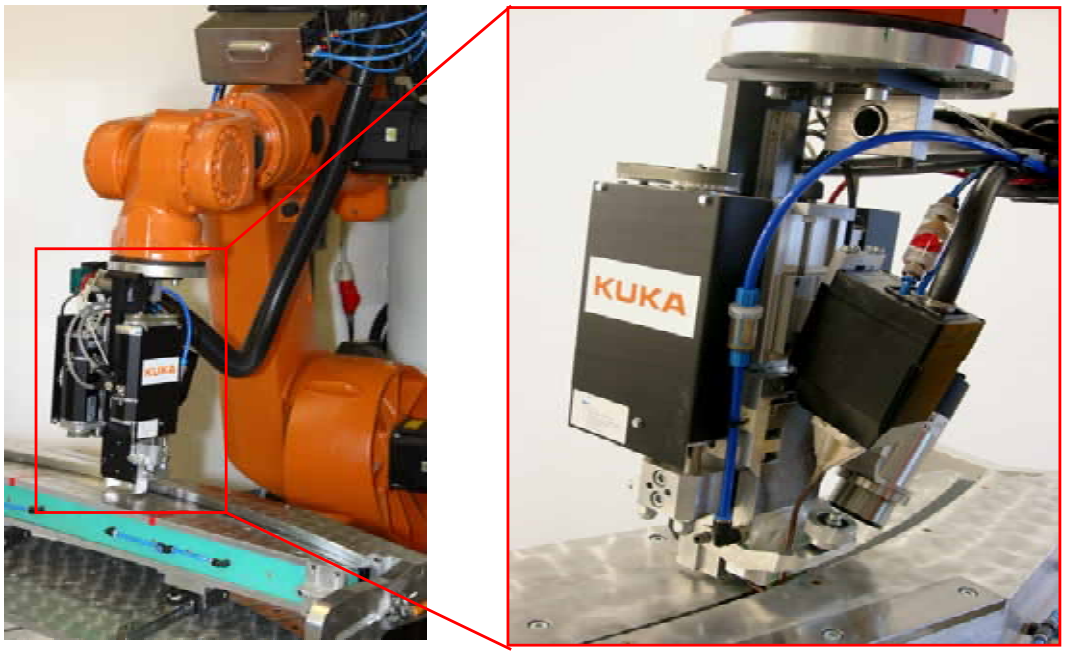

Figure 8: Induction welding robot at the Institut für Verbundwerkstoffe

Differing from the two-dimensional setup, the workpiece is fixed, whereas the welding unit, consisting of coil and consolidation rollers, is moved by a robot. This enables welding of very large parts, if appropriate handling systems, such as gantry robots, are available [32].

2.4. Process-Induced Defects in Induction Welding

The anisotropic structure of fiber reinforced polymer composites and resulting heat transfer properties, in combination with typically inherent uneven heating patterns, often result in temperature gradients over- or undershooting the defined processing window. Furthermore, the bulk heating characteristic in the top laminate inevitably causes delamination effects that can boost temperature gradients due to a change of heat transfer from conduction as dominant heat transfer mode to convection.

2.4.1. Thermal Damage

Generally, solid polymeric materials under heat impact are subject to chemical and physical changes. Opposed to thermoset matrices, thermoplastic materials can be softened by heating without irreversible changes provided the heat input stays below the degradation threshold [72]. Contrary to melting, which is a necessary change in welding of composites, changes above the degradation threshold such as thermal degradation and thermal decomposition, are normally undesired. Thermal degradation is a drop of physical, mechanical, or electrical properties due to heat or elevated temperature. Thermal decomposition characterizes the extensive chemical species change caused by heat ([73] as cited in [72]). Typical transitions at higher temperatures are chain scissoring, splitting-off of substituents, and oxidation [74].

Commonly, maximum temperatures [22,29,75,76] or maximum exposure times as a function of temperature [77] are defined for estimation of thermal damage. Threshold temperatures for thermal decomposition are between 450 °C [75], 475 °C [29] and 550 °C [22,77] for CF/PEEK and 370 °C [76] for CF/PPS. For more precise analysis, the degradation reaction can be described by an Arrhenius expression of first order in the remaining polymer mass [10,72,74,78], which takes the residence time into account. Experimental characterization of the degradation behavior of polymeric materials can be accomplished by thermal analysis.

2.4.2. Deconsolidation

Induction heating of composites is inevitably characterized by through-the-thickness heating of the laminate [23,71]. At temperatures close to the melting temperature, laminates start to deconsolidate, which can involve void formation and growth, buckling, delamination, or similar effects [21,23,63,79], mainly due to localized thermal stresses [63,71]. Generally, thermal deconsolidation effects can be characterized by

an increase of the void content [21]. In case of local intraply separation excessive overheating occurs. In order to prevent deconsolidation during the welding process, pressure has to be applied [11,53,80,81]

2.5. Processing Window

In general, a joint of highest quality possible produced in minimal processing time is desirable. In welding of composites, the requirements of full consolidation and limited thermal damage set the constraints to the process [10]. Amorphous polymers have to exceed the glass transition temperature T_g [11,27], see 2.1.4. However, at temperatures close to T_g, flow and diffusion are rather slow. Therefore, for most amorphous thermoplastic matrices, a temperature level of 100 K above T_g is recommended [27]. Semi-crystalline polymers must exceed the melting temperature T_{melt} as most molecules are still bound in crystallite regions at temperatures between T_g and T_{melt}, preventing flow and diffusion [27]. A usual recommendation for the target temperature is 50 K above the melting temperature [27], where 343 °C and 280 °C are the melt temperatures for CF/PEEK [75] and CF/PPS [76], respectively. If the heat input is limited in order to prevent thermal damage, consolidation is adversely affected [10]. For best consolidation quality, low viscosity values that can be achieved by high temperature levels are required. Contradictory, large amounts of heat facilitate degradation.

Using the recommended target temperature as the lower and the decomposition temperature as the upper threshold, the processing window for CF/PEEK spans between 400 °C and (depending on the reference) 450 °C to 550 °C, whereas the processing temperature for CF/PPS should be between 330 °C and 370 °C. Consequently, the maximum allowed temperature gradient in the bondline is about 50 K-150 K for CF/PEEK and 40 K for CF/PPS.

2.6. Process Modeling of Induction Welding

Inductive heating is a complex technique, involving and coupling electromagnetics and heat transfer phenomena [47,82]. Therefore, analytical models or simplified approaches enable only estimations and involve numerous simplifications [35]. Process development is often achieved by time-consuming trial and error procedures with various degrees of success [82].

Process modeling can be a viable tool for an in-depth understanding of the process. Most of the studies available (see [25] for an overview) focus on the heat generation mechanism and only limited work has been published on modeling of the process on the macro-level in order to cover design aspects of induction welding systems such as coil design or tooling. Lin et al. used the Finite-Difference-Method to calculate two-dimensional (in-plane) heating patterns for different coil designs [29,62,65]. Rudolf et al. showed the adequacy of the Finite-Element-Method using a monolithic material model for the induction heating process [31,35]. Bensaid et al. modeled the inductive heating of a multi-axial CF/PPS laminate [83].

2.6.1. Basic Equations for Process Modelling

For analysis of electromagnetics on a macroscopic level Maxwell's equations need to be solved as given by Equation (6) to Equation (9) [84],

$$\nabla \times \boldsymbol{H} = \boldsymbol{J} + \frac{\partial \boldsymbol{D}}{\partial t} \tag{6}$$

$$\nabla \times \boldsymbol{E} = -\frac{\partial \boldsymbol{B}}{\partial t} \tag{7}$$

$$\nabla \cdot \boldsymbol{D} = \rho_{\mathrm{cd}} \tag{8}$$

$$\nabla \cdot \boldsymbol{B} = 0 \tag{9}$$

where **H** is magnetic field intensity, **J** is current density, **D** is electric flux density, **E** is electric field intensity, **B** is magnetic flux density, and ρ is electric charge density.

Generally, changes in time of currents and charges are synchronized with changes of the electromagnetic field. The changes of the fields are delayed to the changes of the sources due to finite speed of propagation of electromagnetic waves [84]. However, if the variations in time are small and the studied geometries are considerably smaller than the wavelength, which is calculated by Equation (10) [45,85],

$$\lambda = \frac{c}{f} \tag{10}$$

where λ is wavelength in m, c is speed of light in vacuum, and f is frequency, a quasi-static approximation is valid [84]. Then Equation (6) can be rewritten as Equation (11).

$$\nabla \times \boldsymbol{H} = \boldsymbol{J} \tag{11}$$

Introducing Ohm's law, which is appropriate for fiber heating dominated induction heating of composites, gives Equation (12) [62],

$$\boldsymbol{J} = \sigma \cdot \boldsymbol{E} \tag{12}$$

where **J** is current density, σ is electrical conductivity, **E** is electrical field intensity, and adding external current density $\mathbf{J}_e$ Equation (11) results in Equation (13).

$$\nabla \times \boldsymbol{H} = \sigma \boldsymbol{E} + \boldsymbol{J}_e \tag{13}$$

Magnetic field intensity **H** and magnetic flux density **B** can be coupled using magnetic permeability μ, see Equation (14) and Equation (15). The absolute value of B accounts for the magnetic properties of the material present in the magnetic field [48],

$$\boldsymbol{B} = \mu \boldsymbol{H} \tag{14}$$

$$\mu = \mu_0 \mu_r \tag{15}$$

where μ_0 is permeability of vacuum and μ_r is relative magnetic permeability.

Using the definition of the magnetic vector potential **A**, see Equation (16),

$$\boldsymbol{B} = \nabla \times \boldsymbol{A} \tag{16}$$

and combining with Equation (14) and Equation (15) yields Equation (17).

$$\nabla \times \left(\mu^{-1} \nabla \times \boldsymbol{A} \right) = \sigma \boldsymbol{E} + \boldsymbol{J}_e \tag{17}$$

Additionally, a thermal model has to be solved. The heat equation is based on the first law of thermodynamics, rewritten in terms of temperature [86]. For a solid, the resulting equation is given by Equation (18),

$$\rho c_p \left(\frac{\partial T}{\partial t} + (\boldsymbol{u} \nabla) T \right) = -(\nabla \boldsymbol{q}) + Q \tag{18}$$

where ρ is density, c_p specific heat capacity at constant pressure, T is absolute temperature, t is time, **u** is velocity vector, q is heat flux vector, and Q is heat source. The velocity vector **u** is used in order to model translational movement, such as a moving heat source [86].

Fourier's law is used to describe the relationship between the heat flux vector **q** and the temperature gradient, see Equation (19),

$$\boldsymbol{q} = -k \nabla T \tag{19}$$

where **q** is the heat flux vector, k is thermal conductivity and T is absolute temperature. For anisotropic materials, k becomes a vector [86].

Heat fluxes, e. g. from convection and radiation are estimated by boundary conditions. The heat flux across a boundary can be described by Equation (20) [86],

$$\boldsymbol{n} \cdot \left(k \nabla T\right) = q_0 + h\left(T_{\inf} - T\right) + \varepsilon_e \sigma_{SB}\left(T_{amb}^4 - T^4\right) \tag{20}$$

where **n** is the vector normal to the boundary, q_0 is heat flux entering the domain, h is heat transfer coefficient, T_{inf} is the temperature far away from the modeled domain and heat transfer coefficient, T_{amb} is ambient bulk temperature, ε_e is surface emissivity, σ_{SB} is Stefan-Boltzmann constant, and T is absolute temperature. The heat flux q_0 is interpreted in the direction of the inward normal whereas convection and radiation terms are in the direction of the outward normal.

2.6.2. Convective Cooling

Free convection heat transfer is mostly caused by density gradients caused by temperature differences [87]. For a known Nusselt number, the heat transfer coefficient can be calculated by Equation (21) [87],

$$h = \frac{Nu \cdot k}{l} \tag{21}$$

where h is convective heat transfer coefficient, Nu is Nusselt number, k is thermal conductivity of the fluid, and l is characteristic length.

The Nusselt number is a function of the Grashof number and the Prandtl number. The Grashof number is defined by Equation (22) [87],

$$Gr = \frac{g l^3 \beta \Delta T}{\nu^2} \tag{22}$$

where g is acceleration of gravity, l is characteristic length, β is volumetric thermal expansion coefficient, ΔT is temperature difference between the surface and the fluid, and v is dynamic viscosity of the fluid. The material properties for the fluid can be taken from literature (e. g. [87-89]) with respect to the mean temperature, see Equation (23),

$$T_m = \frac{1}{2}\left(T_0 + T_\infty\right) \tag{23}$$

where T_m is mean temperature, T_0 is surface temperature, and T_∞ is temperature in the fluid outside the boundary layer.

For a horizontal plate, different cases have to be considered when calculating the Nusselt number:

Upside of a Horizontal Plate

The characteristic length for rectangular horizontal plates is given by Equation (24) [87],

$$l = \frac{a \cdot b}{2(a+b)} \tag{24}$$

where a and b are length and width or the plate. The effect of the Prantl number is accounted for by Equation (25) [87],

$$f_2(Pr) = \left[1 + \left(\frac{0.322}{\mathrm{Pr}}\right)^{\frac{11}{20}}\right]^{-\frac{20}{11}} \tag{25}$$

where Pr is the Prantl number. Depending on whether the flow is laminar, defined by Equation (26) [87],

$$Gr \cdot Pr \cdot f_2(Pr) \leq 7 \cdot 10^4 \tag{26}$$

or turbulent, the Nusselt Number can be calculated with Equations (27) or (28) [87].

$$Nu_{laminar} = 0.766\left[Gr \cdot Pr \cdot f_2(Pr)\right]^{\frac{1}{5}} \tag{27}$$

$$Nu_{turbulent} = 0.15\left[Gr \cdot Pr \cdot f_2(Pr)\right]^{\frac{1}{3}} \tag{28}$$

Downside of a Horizontal Plate

While the characteristic length is identical to the upside of the horizontal plate, see Equation (24), the contribution of the Prandtl number is calculated differently, see Equation (29) [87].

$$f_1(Pr) = \left[1 + \left(\frac{0.492}{Pr}\right)^{\frac{9}{16}}\right]^{-\frac{16}{9}} \tag{29}$$

For a laminar flow, defined by Equation (30),

$$10^3 < Gr \cdot Pr \cdot f_1(Pr) < 10^{10} \tag{30}$$

the Nusselt number is given by Equation (31).

$$Nu = 0.6\left[Gr \cdot Pr \cdot f_1(Pr)\right]^{\frac{1}{5}} \tag{31}$$

Vertical Faces

For vertical faces the height of the face h_f defines the characteristic length l, see Equation (32) [87],

$$l = h \tag{32}$$

and the Nusselt number is calculated by Eqation (33) [87].

$$Nu = \left(0.825 + 0.387 \left[Gr \cdot Pr \cdot f_1(Pr) \right]^{\frac{1}{6}} \right)^2 \tag{33}$$

Impinging Jets

Gas jets (single jets or arrays) impinging in normal direction on a surface are an effective method for achieving enhanced convection coefficents and are used in numerous applications, e. g. cooling of heated components in gas turbine engines [88]. Figure 9 shows a jet from a round single nozzle width diameter D_n and standoff distance H_{sd}.

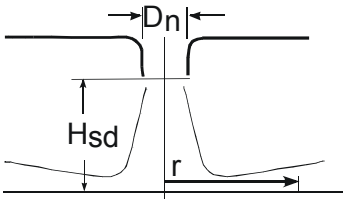

Figure 9: Single round impinging jet [87]

The averaged heat transfer coefficient for an area of diameter 2·r around the nozzle centerline can be calculated by Equation (34) [87],

$$\bar{h} = \frac{Nu \cdot k}{D_n} \tag{34}$$

where $\bar{h}$ is averaged heat transfer coefficient, Nu is Nusselt number, k is thermal conductivity of the material to be cooled, and D_n is nozzle diameter.

The flow becomes turbulent for Reynolds numbers of approximately Re≥100, which is the chase in most technical relevant applications [87]. For the single round nozzle, the Reynolds number is achieved by Equation (35) [87],

$$\mathrm{Re}_{SRN} = \frac{wD_n}{\nu} \tag{35}$$

where Re_{SRN} is Reynolds number of single round nozzle, w is fluid velocity, D_n is nozzle diameter and v is dynamic viscosity.

With Equation (36) to (38)

$$F(Re) = 2\left[Re \cdot \left(1 + 0.005 \cdot Re^{0.55}\right)\right]^{0.5} \tag{36}$$

$$r^* = \frac{r}{D_n} \tag{37}$$

$$h^* = \frac{H_{sd}}{D_n} \tag{38}$$

the Nusselt number can be found by Equation (39),

$$Nu_{SRN} = \frac{1 - 1.1/r^*}{r^* + 0.1\left(h^* - 6\right)} \cdot F(Re) \cdot Pr^{0.4} \tag{39}$$

where Nu_{SRN} is Nusselt number of single round nozzle, Re is Reynolds number, and Pr is Prandtl number. Equation (39) is valid in the range defined by Equation (40) to Equation (42) [87].

$$2.5 < r^* < 7.5 \tag{40}$$

$$2 < h^* < 12 \tag{41}$$

$$2 \cdot 10^3 < Re < 4 \cdot 10^5 \tag{42}$$

Calculating the Nusselt number, the fluid properties have to be related to the mean fluid temperature [87], see Equation (43),

$$T_m = \frac{1}{2}\left(T_N + T_S\right) \tag{43}$$

where T_m is mean fluid temperature between nozzle outlet and surface, T_N is temperature at nozzle outlet, and T_S is surface temperature.

2.6.3. Heating Mechanisms in Susceptorless Induction Heating

Different heating mechanisms with varying contributions, dependent on the architecture, processing, and consolidation of composite, are possible. Fiber heating due to Joule losses, dielectric hysteresis, and contact resistance heating; the first occurring along the carbon fibers, the latter ones at fiber crossover junctions, see Figure 10 [30], are described in detail below.

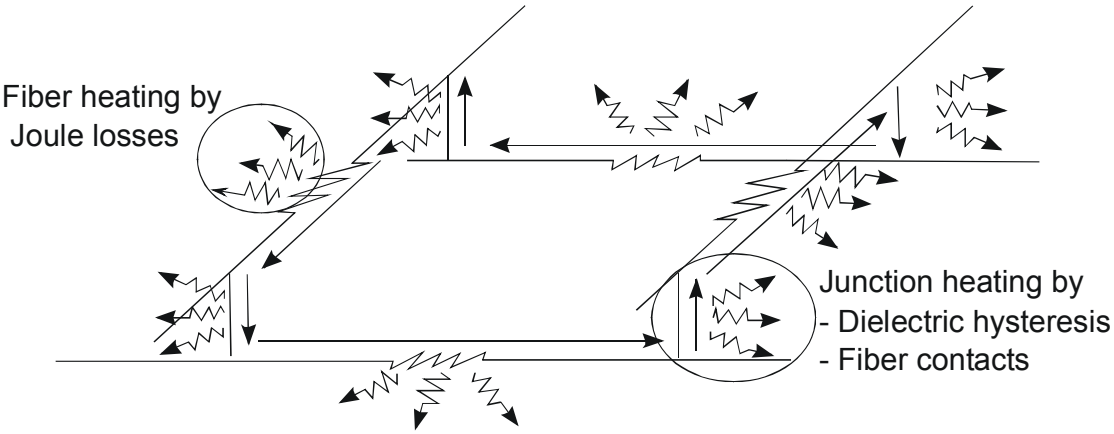

Figure 10: Heating mechanisms of carbon fiber reinforced polymer composites [30]

Fiber heating

Cross-ply, pre-consolidated materials with good electrical contact between the plies or laminates with woven reinforcement show temperature increase due to fiber heating [23,29,31,35,36]. A contact resistance of 10^3 Ω was suggested as threshold for the dominance of fiber heating [30]. The voltage drop across the fiber (ΔV_f) and fiber length (l_f) are determined by the induction parameters and reinforcement architecture; electrical resistance (R_f) and heat generation (P_f) are dependent on the cross-sectional area (A_f), fiber resistivity (ρ_f), and length (l_f) see Figure 11 and Equation (44) [30].

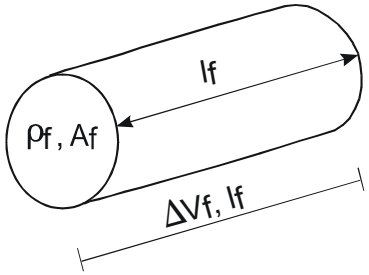

Figure 11: Joule heating in the conductive fiber as a function of its intrinsic resistance [30]

$$R_f = \rho_f \frac{l_f}{A_f} \tag{44}$$

Junction heating

Other heating mechanisms occur at the fiber junctions. If the carbon fibers are not in good contact (contact resistance > 10^3-10^4 Ω [30]) junction heating dominates.

Two different mechanisms can be effective, dependent on the electrical contact between the fibers. If a small layer of matrix material separates these, no direct contact is possible and the matrix material acts like a dielectric [30,51,90] The fibers with the dielectric in between can be modeled as capacitor (C_{jd}) and resistor (R_{jd}) in parallel and heating occurs due to dielectric losses, see Figure 12 and Equation (45) [30],

$$R_{jd} = \frac{h}{\omega \varepsilon_0 \kappa (\tan \delta) d_f^2} \tag{45}$$

where R_{jd} is junction dielectric impedance, h is fiber to fiber separation between to fibers at the ply interface, d_f the fiber diameter, tanδ the dissipation factor, ω the angular frequency, κ the dielectric constant, and ε_0 the permittivity of vacuum.

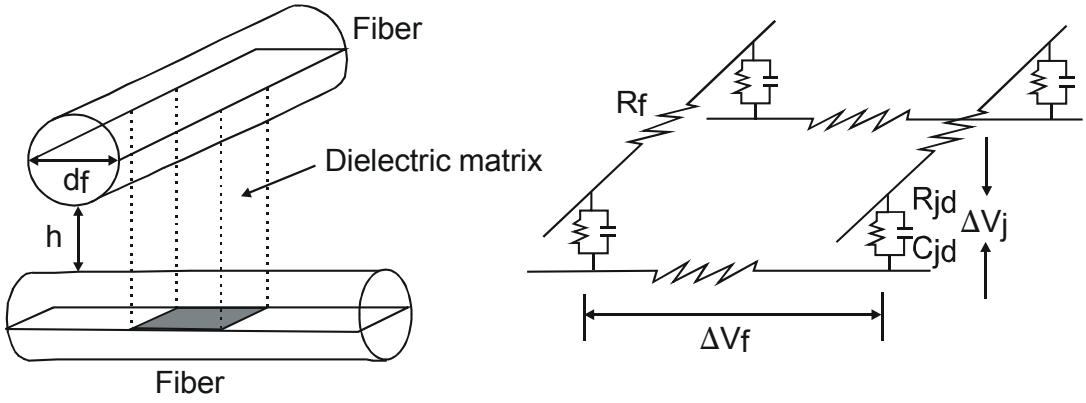

Figure 12: Dielectric heating at a junction [30]

In case of fiber cross-over points in a non-unidirectional composite heating occurs due to voltage drop at the junctions, see.Figure 13.

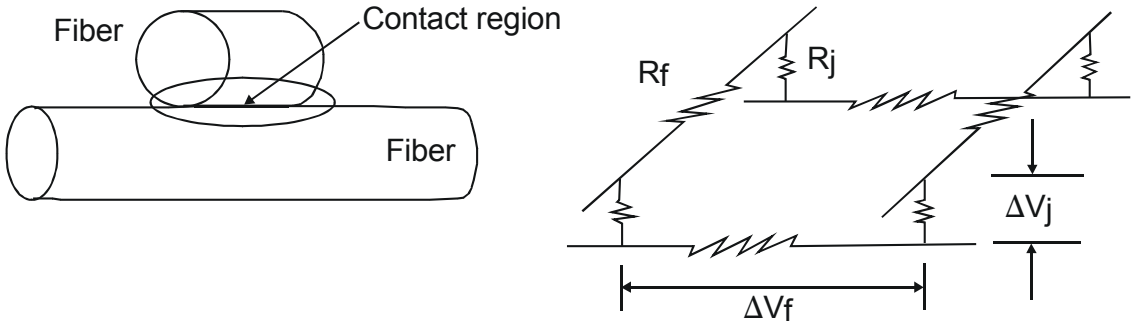

Figure 13: Contact resistance heating at a junction [30]

The heat generation depends on the contact resistance at the junctions, see Equation (46) [30],

$$R_j = R_{jc} \tag{46}$$

where R_{jc} is contact resistance at the junctions.

For modeling of the induction heating process, it is necessary to determine the dominant heating mechanism for the system under analysis. Unconsolidated materials heat up differently from consolidated composites, or UD-layers from cross-ply laminates or weaves. Other influencing factors are the fiber or matrix type and the induction parameters [30]. Weaves or knitted fabrics show fiber heating dominance due to direct fiber contact [30,36] whereas junction heating is the major mechanism for unconsolidated prepreg stacks [91].

Heat is generated according to Joules law, see Equation (47).

$$P = I^2 \cdot R \tag{47}$$

The heat generation due to the individual mechanisms can be described with Equation (47), using the appropriate resistance value, see Equations (44) to (46). The induced current has to be determined from Farady's law of induction [30], see Equation (7). Precise calculations of the heat generation require numerical methods; however, Equation (48) gives an estimate [36]:

$$P = \frac{4 \cdot \pi^2 \cdot f^2 \cdot \mu^2 \cdot H^2 \cdot A^2}{R} \tag{48}$$

where P is power, f is the field frequency, μ is the permeability of the workpiece material, H is the magnetic field intensity, A is the area enclosed by conductive fiber loop, and R is the resistance.

3. Induction Heating Characterization of Carbon Fiber Reinforced Laminates

3.1. Materials

Two different pre-consolidated high performance carbon fiber reinforced thermoplastic composites were used in this study. Both carbon fiber reinforced polyetheretherketone (CF/PEEK) and carbon fiber reinforced polyphenylenesulfide (CF/PPS) were manufactured by the Institut für Verbundwerkstoffe using the identical satin 5 harness carbon fiber weave type CD 0282.040.000.0000, supplied by Ten Cate Advanced Composites, made from Toray 3k T300 fibers. Table 2 gives an overview of the fabric and the polymers used for production of the laminates.

Table 2: Fabric and polymers used for manufacturing of the laminates

Material	CF-Fabric	PPS	PEEK
Designation	CD 0282.040.000.0000,	Fortron	Victrex 150PF
Type	Satin 5H, 3k, 285 g/m^2	Film	Granule
Supplier	Ten Cate Advances Composites B. V., The Netherlands	Ticona GmbH, Germany	Victrex Europa GmbH, Germany

The CF/PEEK laminates were produced from powder prepregs (manufactured at the Institut für Verbundwerkstoffe) as intermediate step with subsequent pressing at 25 bars in a continuous compression molding machine. The CF/PPS laminates were produced by film stacking with subsequent processing in an autoclave at 20 bars. Polymer suppliers were Victrex (PEEK) and Ticona (PPS). Both laminate types are composed of six plies with a fiber volume content of 50 %. The equipment used is covered in detail in [7,92].

Table 3: Manufacturing processes for the laminates used

Material	CF/PEEK	CF/PPS
Manufacturing process	Continuous compression molding	Autoclave
Fiber volume content [%]	50	50
Consolidation pressure [bar]	25	20
Manufacturer	Institut für Verbundwerkstoffe GmbH, Germany	

3.2. Experimental Setup

Static heating experiments were performed in order to assess the heating behavior of the preconsolidated laminates. For this purpose, specimens of 100 mm x 100 mm x 2 mm were placed into a test bed with wooden sample carrier. Four polymer clamps were used to ensure coplanar orientation of the laminate. An induction generator CEIA Power Cube 32/400 was used as the heat source. Its nominal operating frequency is 400 kHz; the maximum input power is 2800 W. The oscillating circuit consists of an induction coil and a capacitor package. The output power is controlled by percentage power, which ranges from 10 % to 99 % output power. A two-turn pancake induction coil (outer diameter 25 mm) was manufactured from copper tube (diameter 3 mm), see Figure 14

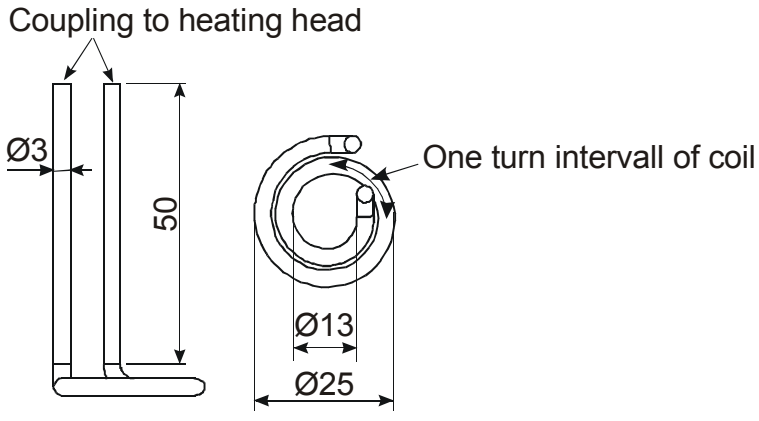

Figure 14: Geometry of pancake coil

The coil geometry consists of a horizontal part that is oriented parallel to the laminates and a vertical part that is coupled to the heating head of the generator. The vertical part of the coil features a bend of 90° and does not contribute to the heating.

Consequently, approximately one quarter of the pancake coil has only one effective turn.

In order to assess the temperature gradient through-the-thickness of the laminates, point temperature measurements were performed on both sides of the laminate. The locations of maximum temperature were shaded by the coil. Therefore, the temperature was measured besides the outer diameter of the induction coil and at the corresponding spot on the opposite side using pyrometers (Raytec RAYMMLTSCF1L). The coil position, the pyrometer spot measurement locations (up- and downside), and the laminate are shown in Figure 15.

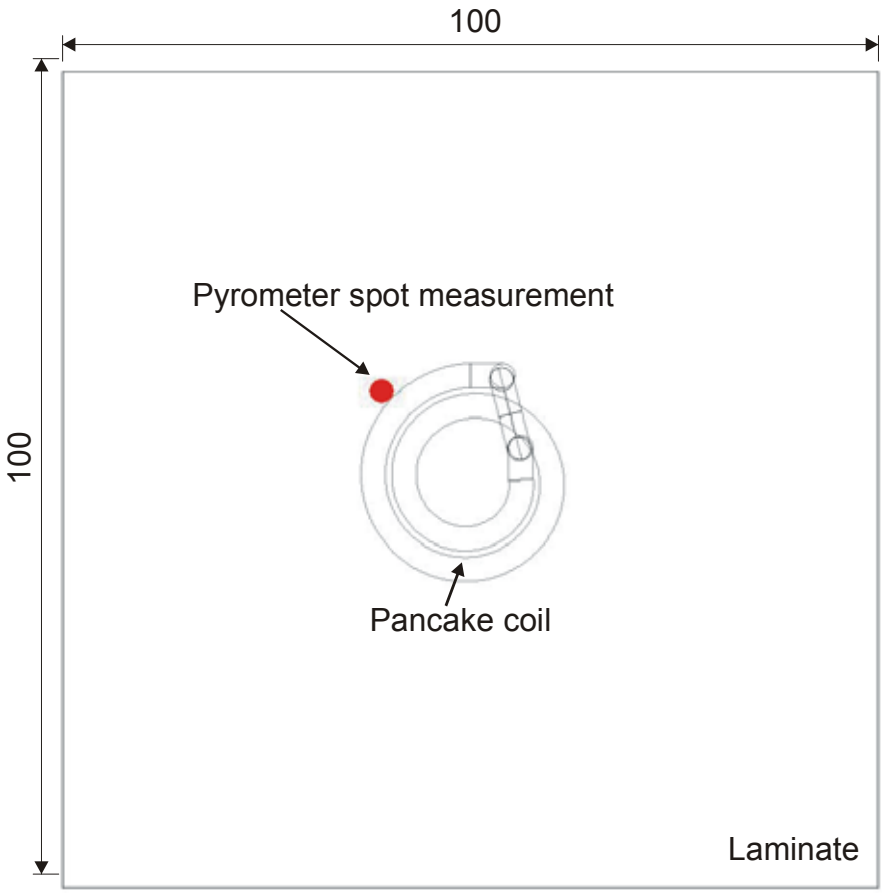

Figure 15: Pancake coil and spot measurement locations (schematic)

For evaluation of the in-plane heating patterns, a thermal camera (Infratec Infracam Head) was used to capture areal thermal images of the surface opposite to the induction coil. The emission factor of the laminates was set to 0.95. The complete setup is shown in Figure 16.

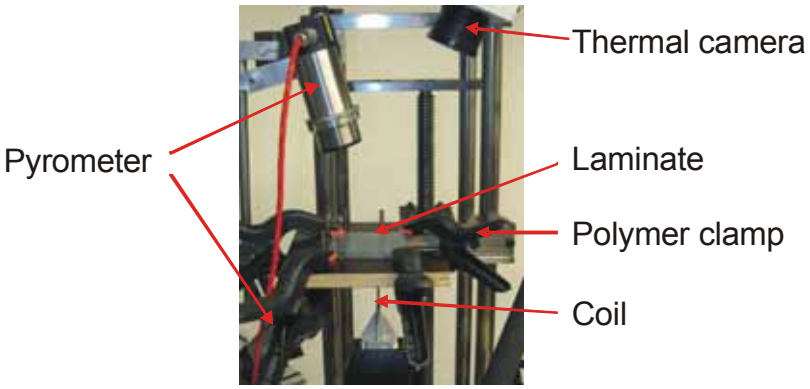

Figure 16: Test bed for validation of single sheet induction heating model

Heating experiments with two different coupling distances and three different power settings were performed, see Table 4. Three experiments per parameter combination using a new specimen for each test were executed.

Table 4: Parameters for induction heating characterization

Coupling Distance [mm]	Generator Power [%]
2	10
	20
	30
3	10
	20
	30

The samples were heated up to the welding temperature T_w, which is approximately 50 °C above melting temperature, see Table 5. Either exceeding T_w or the maximum heating time of 14 seconds, depending on which criteria was reached at first, terminated the experiments.

Table 5: Welding temperature for CF/PEEK and CF/PPS

Material	Welding temperature [°C]
CF/PEEK	400
CF/PPS	330

3.3. Results

The heating behavior of CF/PEEK and CF/PPS laminates is similar; therefore the details below apply to both materials. The heating behavior through-the-thickness and in-plane is discussed separately below.

3.3.1. Through-the-Thickness Temperature Distribution

For each temperature graph the mean value from three measurements and sample standard deviation were calculated, see Equation (47).

$$s = \sqrt{\frac{1}{N-1}\sum_{i=1}^{N}\left(x_i - \bar{x}\right)^2} \tag{49}$$

where s is sample standard deviation, N is number of samples, x_i are individual values, and $\bar{x}$ is the mean value.

Assuming an adiabatic system, constant input values for the estimation of the input power, see Equation (48), and neglecting effects such as melting, deconsolidation, or degradation, the electrical energy coupled into the laminate is a function of time, see Equation (50)

$$E_e = \int P \cdot dt \tag{50}$$

where E_e is electrical energy, P is power, and t is time. Thus, in order to determine the approximate averaged heating rates, linear trendlines were used. The equations of the trendlines are in the form of Equation (51),

$$y = mx + c \tag{51}$$

where m is slope and c is intercept. The intercept was set to 25 °C whereas the slope represents the heating rate.

The mean temperature profiles of the spot measurement positions, see Figure 15, both the side facing the induction coil and the side opposite to the coil (referred to as

“Inductor” and “Opposite” in the graphs) are plotted with respect to heating time and grouped by coupling distance and materials, see Figures 16 to 19.

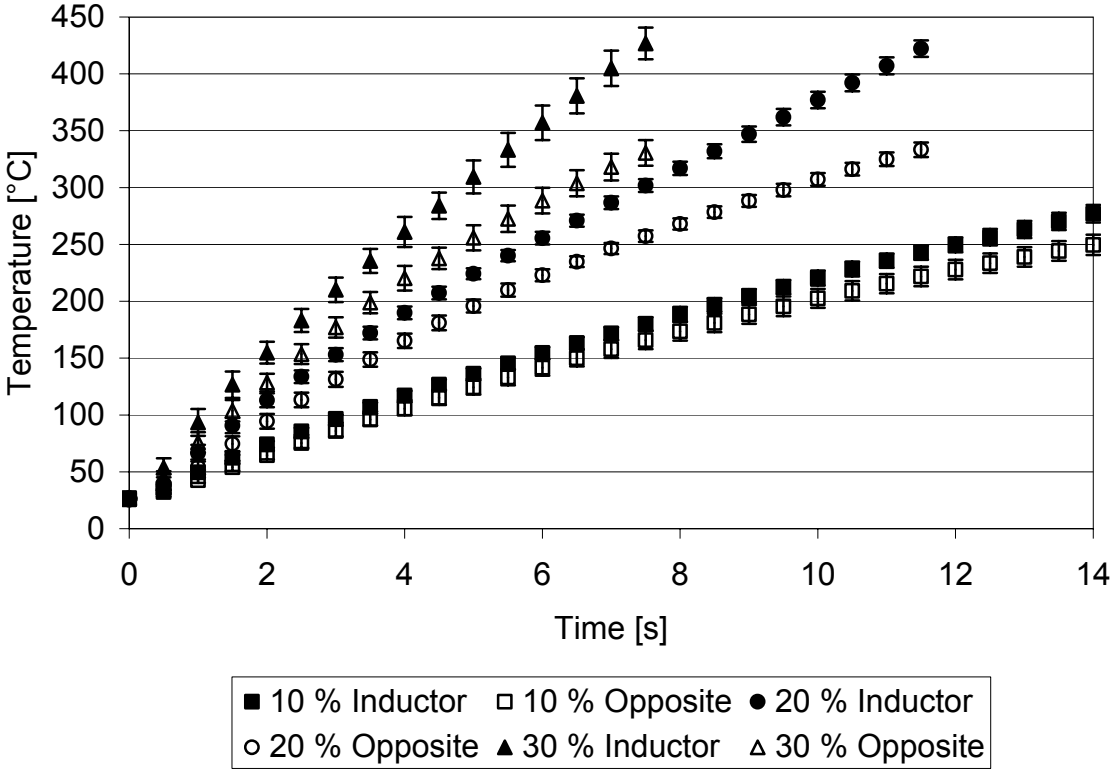

Figure 17: Inductive heating of CF/PEEK, 2 mm coupling distance

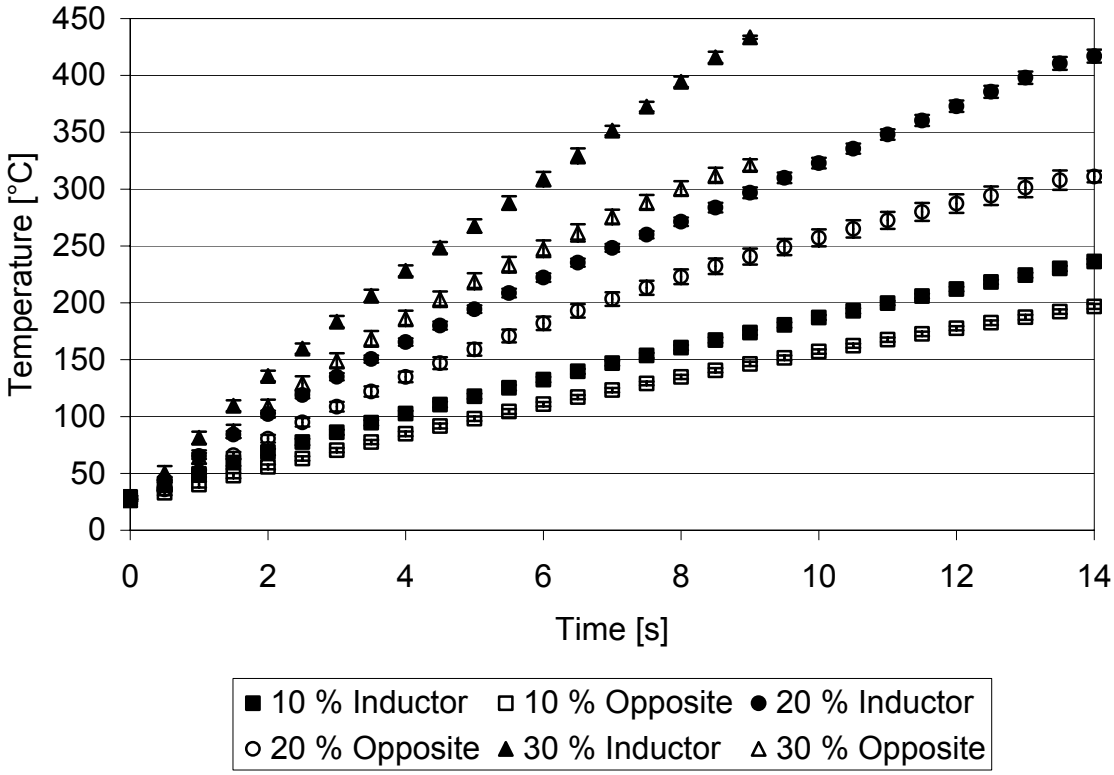

Figure 18: Inductive heating of CF/PEEK, 3 mm coupling distance

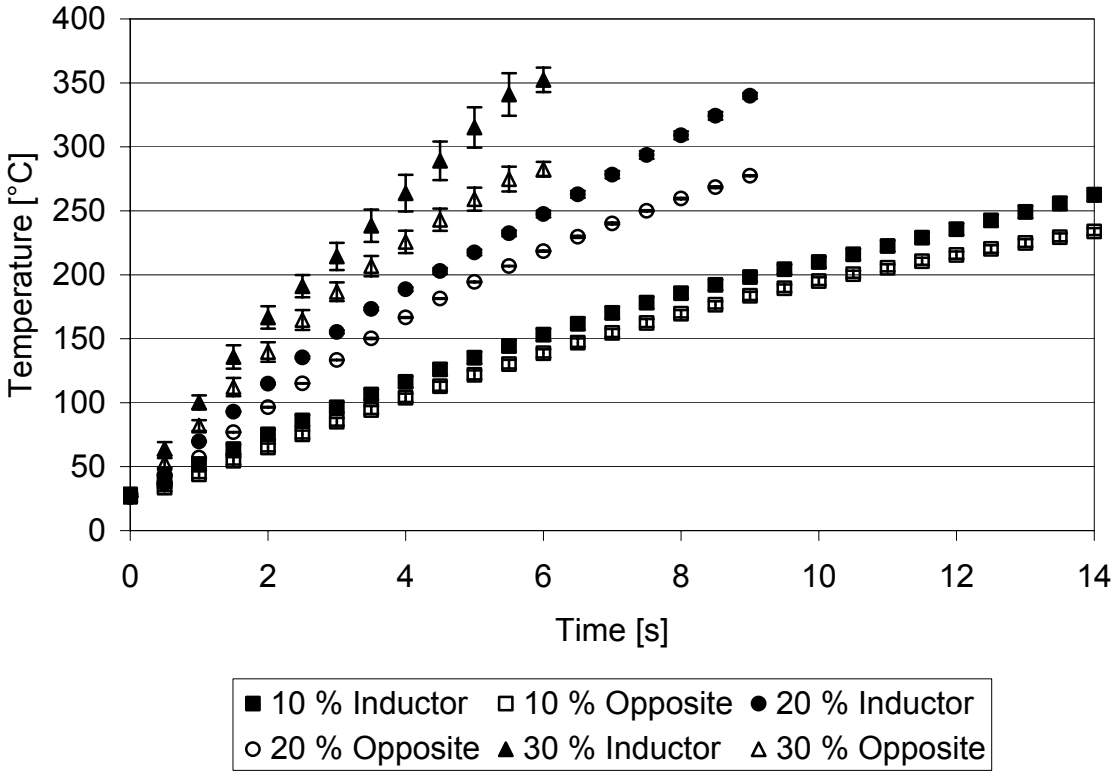

Figure 19: Inductive heating of CF/PPS, 2 mm coupling distance

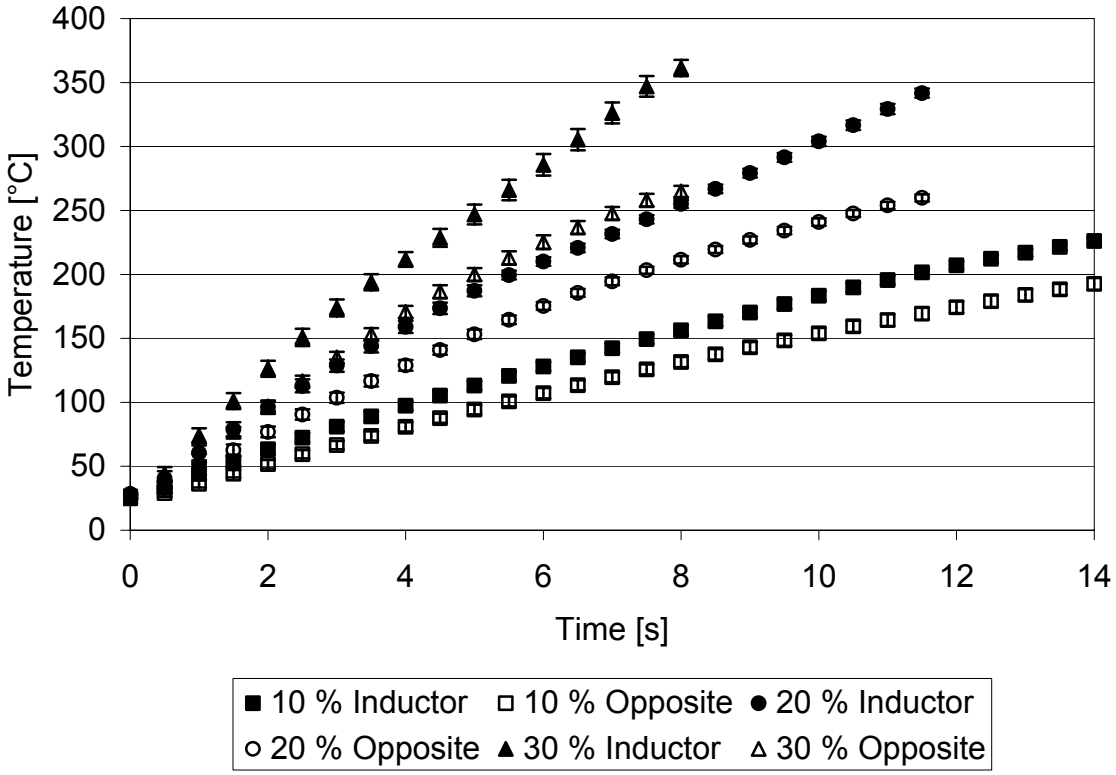

Figure 20: Inductive heating of CF/PPS, 3 mm coupling distance

In all experiments, the inductor side yielded higher heating rates compared to the opposite side. A 10 % generator power lead to low heating rates compared to medium ones for 20 % and high ones for 30 % generator power. The 2 mm coupling distance yielded higher heating rates compared to a 3 mm coupling distance. The values range from 14 K/s (3 mm coupling distance and 10 % power) to 56 K/s (2 mm coupling distance and 30 % power) on the inductor side and 11 K/s (3 mm coupling distance and 10 % power) to 44 K/s (2 mm coupling distance and 30 % power) on the opposite side for CF/PEEK. For CF/PPS the values range from 14 K/s (3 mm coupling distance and 10 % power) to 59 K/s (2 mm coupling distance and 30 % power) on the inductor side and 11 K/s (3 mm coupling distance and 10 % power) to 48 K/s (2 mm coupling distance and 30 % power) on the opposite side. Table 6 summarizes the effect of the processing parameters on the heating rates, which are almost identical for CF/PEEK and CF/PPS.

Table 6: Heating rates for static induction heating

Coupling Distance [mm]	Generator power [%]	Heating rate [K/s]		
		Side	CF/PEEK	CF/PPS
2	10	Inductor	17	17
		Opposite	15	15
	20	Inductor	36	37
		Opposite	30	31
	30	Inductor	56	59
		Opposite	44	48
3	10	Inductor	14	14
		Opposite	11	11
	20	Inductor	30	29
		Opposite	23	23
	30	Inductor	47	44
		Opposite	36	33

Higher power settings and therefore higher heating rates yield shorter heating times to reach welding temperature T_w with the exception of 10% power, which proves to be insufficient to heat the laminates to the desired temperature in the maximum heating time. Likewise, a closer coupling of 2 mm between the inductor and the laminate results in shorter heating times compared to the greater coupling distance of 3 mm.

As a consequence of the heating rate difference between inductor and opposite side, the surface facing the inductor reaches a higher temperature compared to the opposite side and a through-the-thickness temperature gradient ΔT_s between the surfaces is observed. The maximum differences (referred to as $\Delta T_{s,max}$) are present at the end of the heating cycle. ΔT_s is influenced by the power setting and the heating time. The temperature difference is influenced by the applied power; which means that 10 % power yields the lowest difference, whereas 20 % leads to medium, and 30 % to the highest values of ΔT_s. The coupling distance also influences the temperature distribu-

tion in the laminate. A smaller coupling distance of 2 mm produces a smaller temperature difference compared to the greater one of 3 mm. Table 7 summarizes the heating times and maximum temperature differences.

Table 7: Times to reach welding temperature and maximum temperature difference between inductor and opposite side of laminate

Coupling Distance [mm]	Power [%]	CF/PEEK		CF/PPS	
		Time to T_w [s]	$\Delta T_{s,max}$ [K]	Time to T_w [s]	$\Delta T_{s,max}$ [K]
2	10	Insufficient heating			
	20	11	82	9	63
	30	7	87	5.5	66
3	10	Insufficient heating			
	20	13.5	102	11.5	82
	30	8.5	104	7.5	89

Heating times to exceed the desired processing temperature are in the range of 7 seconds (2 mm coupling distance and 30 % power) to 13.5 seconds (3 mm coupling distance and 20 % power) for CF/PEEK and in the range of 5.5 seconds (2 mm coupling distance and 30 % power) to 11.5 seconds (3 mm coupling distance and 20 % power) for CF/PPS. The respective temperature differences $\Delta T_{s,max}$ are in the range of 82 K (2 mm coupling distance and 20 % power) to 104 K (3 mm coupling distance and 30 % power) for CF/PEEK and in the range of 63 K (2 mm coupling distance and 20 % power) to 89 K (3 mm coupling distance and 30 % power) for CF/PPS.

The effects of the processing parameters under inspection on the through-the-thickness temperature distribution are summarized in Table 8, where ↑ represents an increasing and ↓ a decreasing value.

Table 8: Effects of processing parameters on through-the-thickness temperature distribution

Parameter	Heating time	Heating rate	Temperature gradient
Coupling distance ↑	↑	↓	↓
Power ↑	↓	↑	↑

3.3.2. In-Plane Temperature Pattern

In all experiments a significant in-plane temperature gradient is noticeable. An area of higher temperature, which represents the global current loop of the approximate size of the induction coil, is surrounded by colder areas at the outer diameter and a cold spot in the center of the specimen's surface. Due to the geometry of the woven reinforcement the global current loop is not ideally circular. It rather follows two main directions that are parallel to the warp and weft direction, respectively, resulting in a square heating pattern with rounded edges. In case of rotated (around an axis normal to the center of the cold spot) specimens, the square heating pattern follows the warp and weft direction, respectively, see Figure 21.

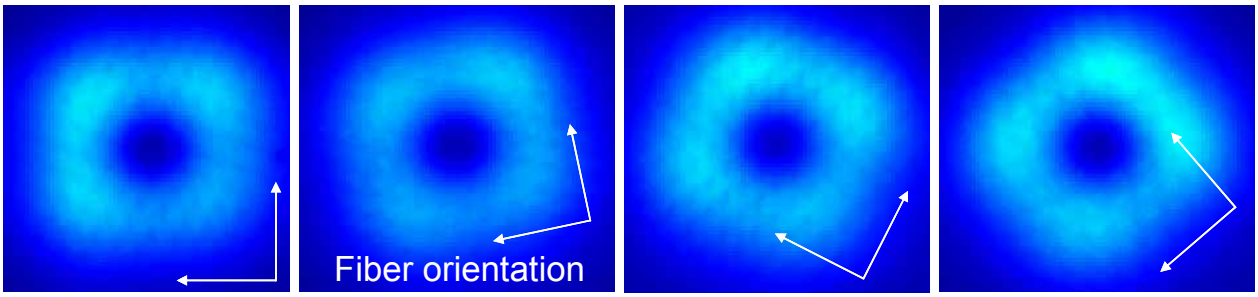

Figure 21: Comparison of heating patterns of different rotated CF/PEEK specimens

Table 9: Heating patterns of surface opposite to induction coil, CF/PEEK laminates

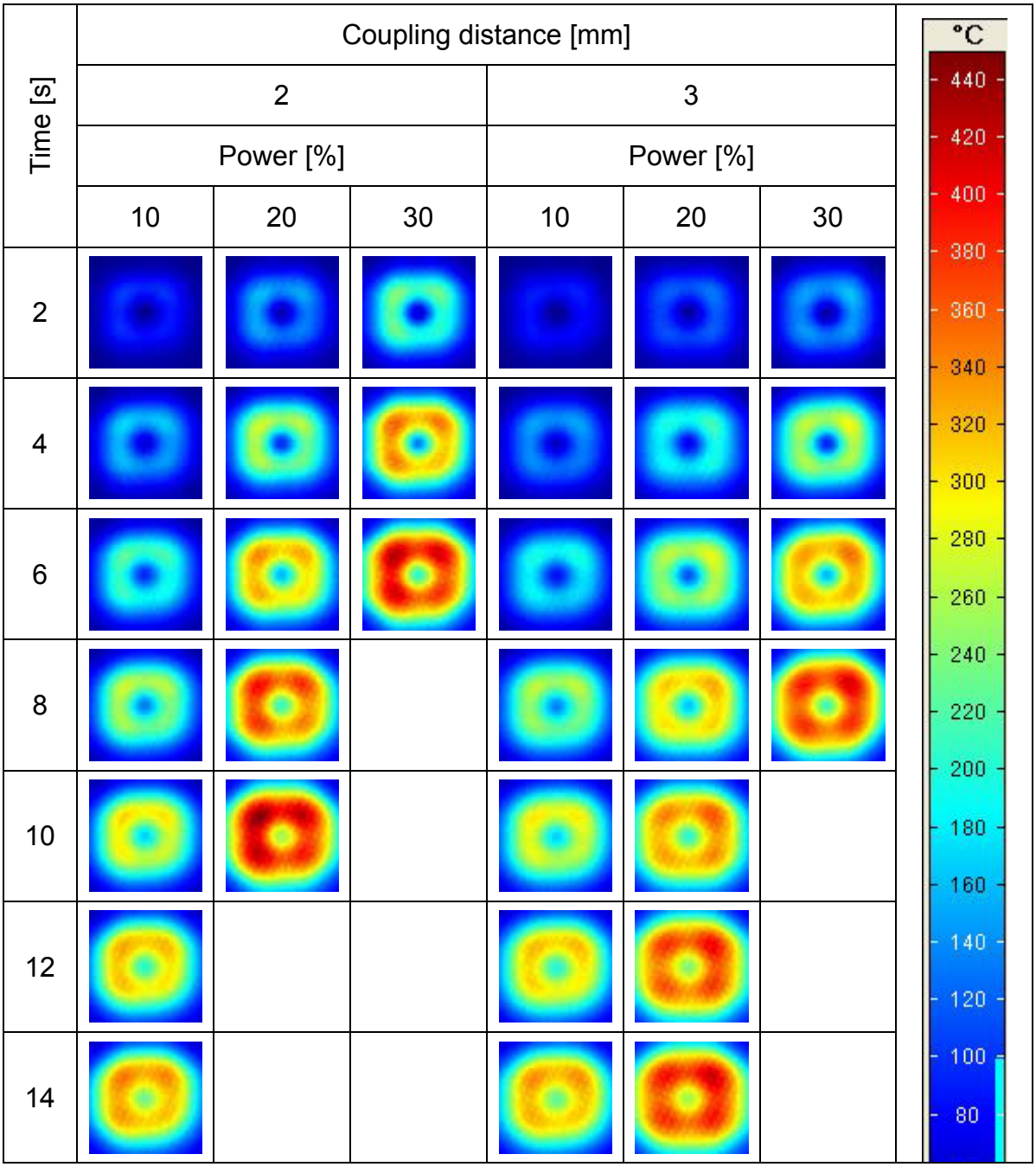

Table 9 and Table 10 present the surface temperature heating patterns in intervals of two seconds of the surface opposite to the induction coil for CF/PEEK and CF/PPS specimens. Due to the global current loop the surface temperature patterns are characterized by a significantly uneven distribution throughout the heating cycle. The peak temperature is always located in the area of the global current loop whereas the center and the outer areas show considerably lower temperatures. Because of the low thermal diffusivity of polymers no compensation by heat transfer occurs.

Table 10: Heating patterns of surface opposite to induction coil, CF/PPS laminates

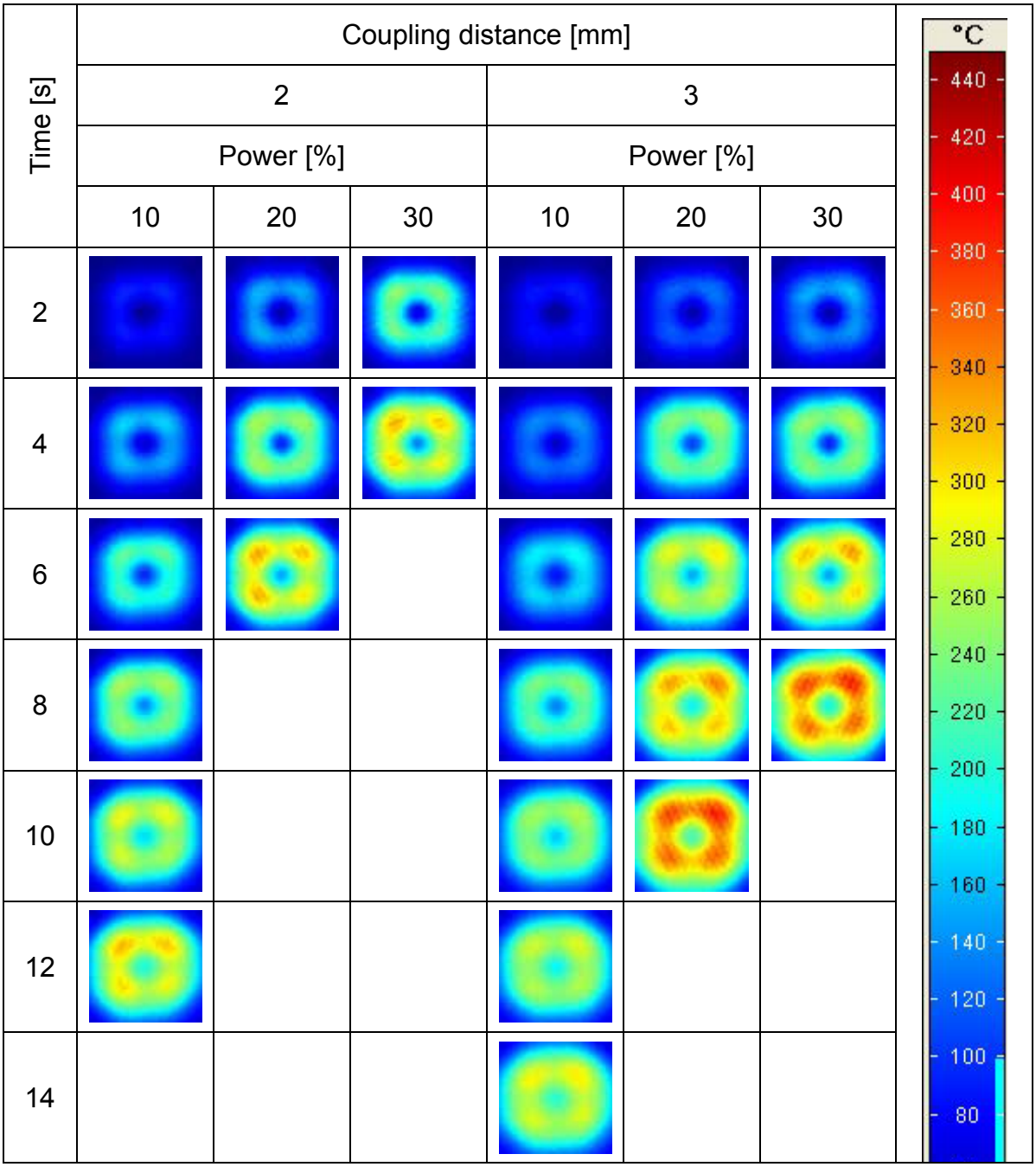

Figure 22 shows a representative close-up of two heating patterns below and above the melting temperature of the matrix (CF/PPS, 2mm coupling distance, 20 % generator power, heating time 2 s and 4 s). The temperature pattern below T_{melt} shows an even temperature in the global current loop, indicating fiber heating as dominant heating mechanism. At temperatures above T_{melt} regions of higher temperature at the junctions are visible, indicating junction heating as dominant heating mechanism. Thermal deconsolidation, which is present at temperatures above T_{melt} yield an increase in thickness [63] and growth of voids [79] and therefore an increased contact

resistance between adjacent plies, which results in a change of the dominant heating mechanism, see Chapter 2.6.3.

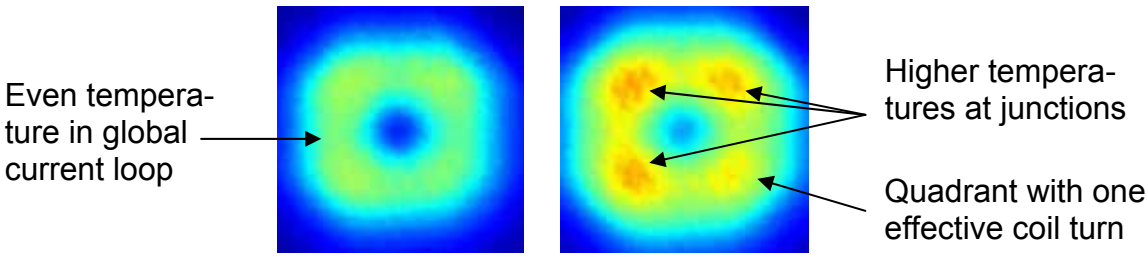

Figure 22: Surface temperature of CF/PPS, 2 mm coupling distance, 20 % generator power, heating time 4 s (left) and 6 s (right), see Table 10 for temperature scale

Because the coil geometry has one quarter turn which features only one effective turn, see Chapter 3.2, the bottom right quadrants of the heating patterns for both CF/PEEK and CF/PPS for the 2 mm coupling distance show lower temperatures (see Figure 22 for a close-up). In contrast, for the 3 mm coupling distance this effect is not noticeable, which may be attributed to the overall lower current densities present for this greater coupling distance.

3.3.3. Cross-Sectional Analysis

During thermal reprocessing of pre-consolidated laminates without the application of pressure deconsolidation occurs. Since no compaction pressure was used formation of voids occurred in all samples.

Figure 23 shows a cross-sectional image of a CF/PEEK sample heated with 20 % generator power at 2 mm coupling distance and the position of the coil during heating as an example for the deconsolidation patterns.

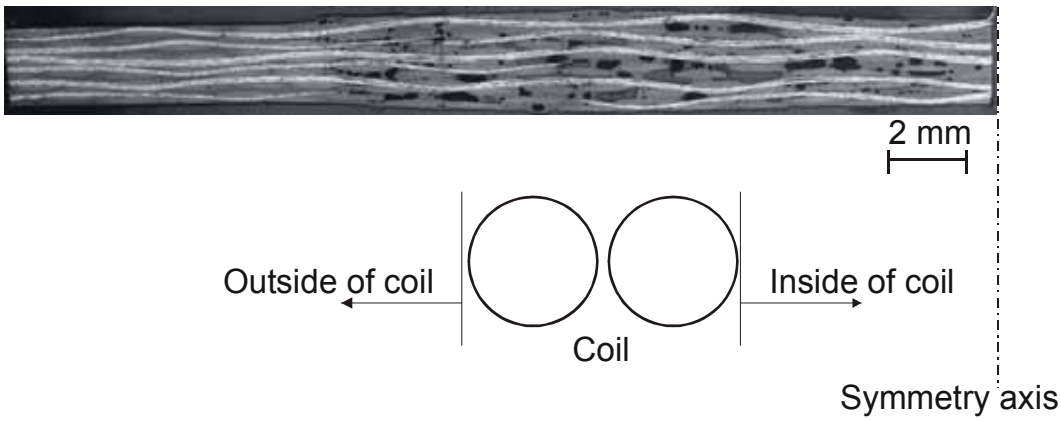

Figure 23: Cross-section of CF/PEEK, 2 mm coupling distance, 20 % generator power with indication of coil position (schematic)

The most significant void formation is visible in the coil region, i. e. the area of the global current loop, showing the highly localized heating behavior.

3.4. Temperature Field

Single-sided induction heating of carbon fiber reinforced laminates with a two-turn pancake coil results in a highly anisotropic temperature field both through-the-thickness and in-plane.

The ideal heating process would yield localized heating in the bondline, which means a high temperature at the side opposite to the coil and low temperature at the coil side, see Figure 24 (a). However, the contrary situation is present; see Figure 24 (b). Gradients in heating rate and consequently surface temperatures between the inductor and the opposite side are present. For all parameter sets the inductor side yields higher temperatures whereas the opposite side, which will be at the interface of the bondline in an overlap joint, reaches lower temperatures.

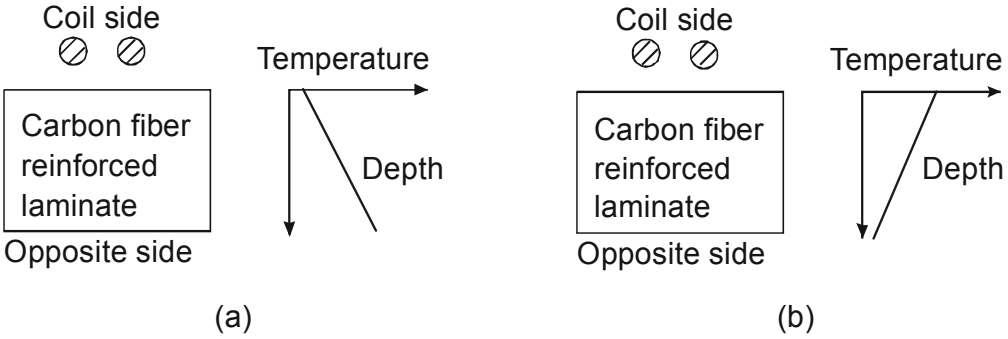

Figure 24: Qualitative through-the-thickness temperature distribution in single-sided induction heating: (a) Optimum distribution (b) Real distribution

Taking into account the processing window for CF/PEEK (see Chapter 2.5), the temperature gradient at the welding temperature $\Delta T_{s,max}$ (almost) exceeds the processing window, just as in case of CF/PPS, see Table 11, making welding difficult.

Table 11: Maximum temperature differences in the thickness direction and processing window

Material	Processing range [K]	Maximum temperature difference [K]
CF/PEEK	50-100	82-104
CF/PPS	40	63-89

During execution of the heating experiments under the conditions described it was not possible to heat the laminates to the required welding temperature on the opposite side without distinct thermal degradation of the specimens on the inductor side. Therefore, the need for an enhanced processing technique eliminating this problem arises.

In contrast, the in-plane temperature gradient does not impede the welding process as severly as the though the thickness temperature field because it can be leveled out by the relative movement in feed direction which is involved in the continuous welding process, see Figure 25. Since the coil geometry consists of a horizontal part parallel to the laminate which contributes to the heating and a vertical part that does not, approximately one quarter of the coil has only one effective turn. This clearly influences the heating pattern in case of the 2 mm coupling distance but is not visible for the 3 mm coupling distance. It is assumed that due to the overall higher current densities this effect is more severe for the smaller coupling distance. A change of the dominant heating mechanism due to thermal delamination above T_{melt} from fiber to junction heating is present, which is in accordance to the theoretical work presented in [30].

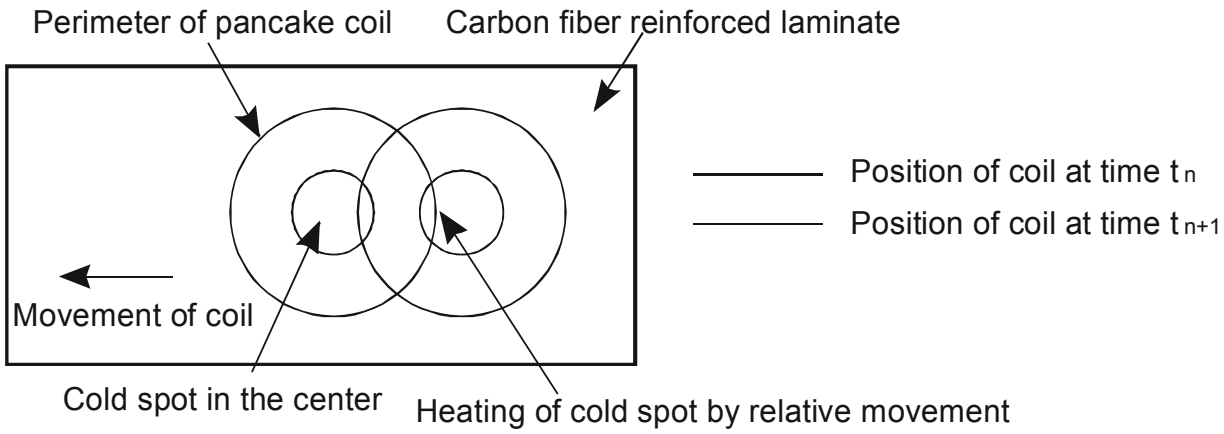

Figure 25: Attenuation of cold spot by relative movement

4. Enhanced Induction Heating Process with Localized Surface Cooling

4.1. Experimental Setup

In order to optimize the through-the-thickness temperature profile and to allow fast processing times required by industry, localized surface cooling on the inductor side was utilized. An impinging jet of compressed air was directed through the center opening of the induction coil perpendicular to the surface. A pneumatic tube with an inner diameter 6 mm made from material unaffected by the electromagnetic field was placed inside the pancake coil, at a stand-off distance of 17 mm to the laminate, see Figure 26.

Figure 26: Coil with pneumatic tube for localized surface cooling with impinging air jet

The volume flow was controlled by a proportional control valve Festo MPYE-5. Two laboratory power supplies (Iso-Tech IPS 303DD and Oltronix B700D) were used to provide operating (24 V) and control voltage (0 V .. 5 V) for the valve. The input pressure was 5 bars and the maximum volume flow of the setup is 350 l/min. Except the addition of the air cooling in the center of the pancake coil the setup was identical to the experiments without surface cooling. Two different power settings and three different compressed air volume flows were used, see Table 12. Three measurements were done for each parameter set and mean values as well as sample standard deviation were calculated, see Equation (47).

Table 12: Parameters for characterization of heating with impinging air jet

Power [%]	Coupling distance [mm]	Tube standoff distance [mm]	Volume flow [l/min]
20	2	17	167
			240
			304
30			167
			240
			304

4.2. Results

4.2.1. Through-the-Thickness Temperature Distribution

The surface cooling significantly changes the temperature field in the laminate. Without cooling, the surface facing the induction coil (inductor side) yields higher temperatures than the surface opposite to the coil (opposite side). With an impinging air jet on the inductor side, the temperature gradient ΔT_s is reversed and the inductor side yields lower temperatures and heating rates, respectively, compared to the opposite side.

In the heating experiments 20 % generator power did not suffice to reach the welding temperature t_w within the defined heating time of 14 s. Figure 27 and Figure 28 show the temperature profiles of the heating experiments with 30 % generator power and localized surface cooling.

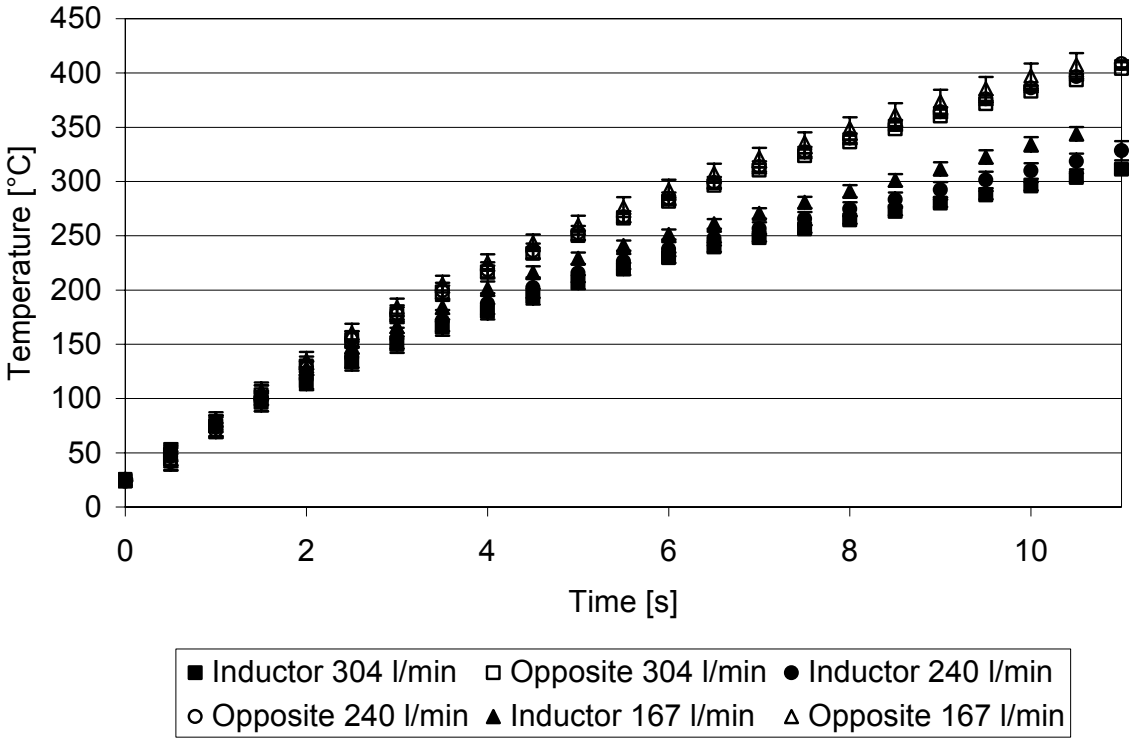

Figure 27: Inductive heating of CF/PEEK with compressed air impinging jet surface cooling at different volume flow rates, 2 mm coupling distance, 30% generator power

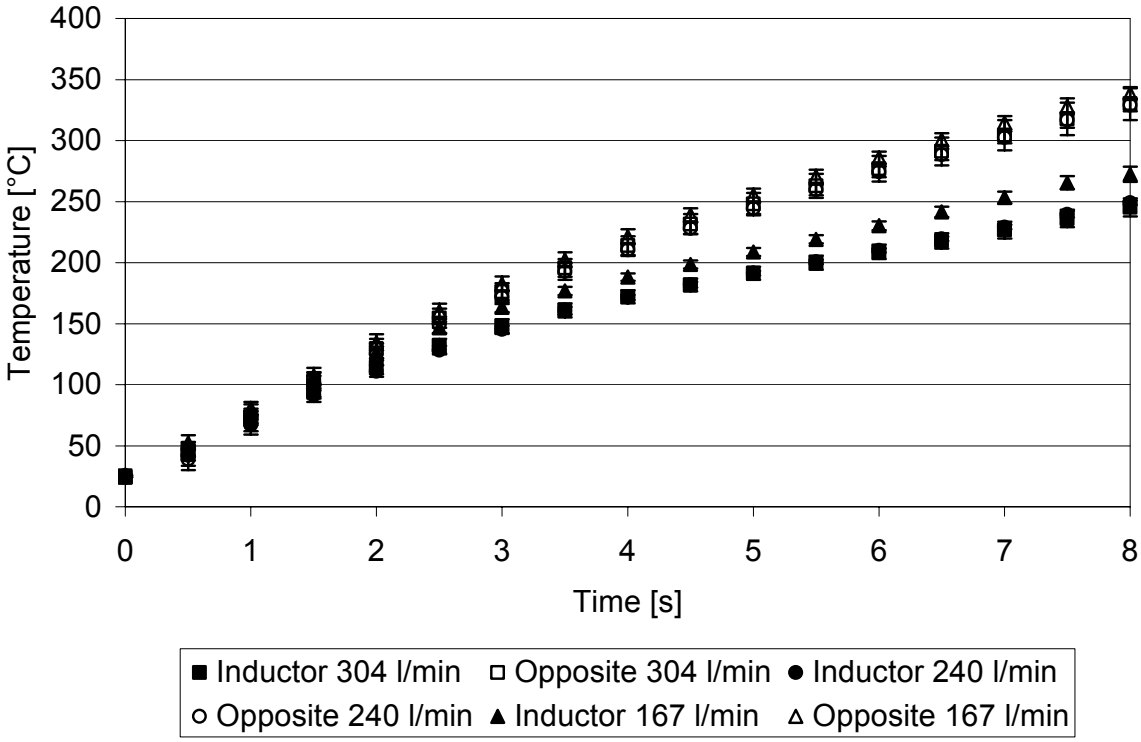

Figure 28: Inductive heating of CF/PPS with compressed air impinging jet surface cooling at different volume flow rates, 2 mm coupling distance, 30% generator power

The heating rate gradient through-the-thickness is influenced by the volume flow of the impinging air jet and ranges between 7 K/s (167 l/min) and 9 K/s (304 l/min) for CF/PEEK and 8 K/s (167 l/min) and 11 K/s (304 l/min) for CF/PPS. The volume flows of 240 l/min and 304 l/min yield almost identical gradients. Table 13 summarizes the heating rates of static heating with the impinging jet. Assuming linearity of the heating curves, the heating rates with an impinging jet of CF/PEEK and CF/PPS are almost identical.

Table 13: Heating rates of static induction heating with localized surface cooling

Distance [mm]	Power [%]	Volume flow [l/min]	Heating rate [K/s]		
			Side	CF/PEEK	CF/PPS
2	30	167	Inductor	34	35
			Opposite	41	43
		240	Inductor	31	31
			Opposite	39	41
		304	Inductor	30	30
			Opposite	39	41

Both for CF/PEEK and CF/PPS the temperature curves of the opposite side show remarkably close progression whereas the characteristics of the temperature curves on the inductor side are influenced more significantly by the air jet. With a volume flow of 167 l/min the temperatures are higher compared to the higher volume flows. However, no significant difference in surface temperature on the inductor side can be found between 240 l/min and 304 l/min. In all cases, the temperature on the inductor side could be maintained below the melting temperature. The heating times to reach the respective welding temperatures t_w on the opposite side, which will be in the bondline in an overlap joint, are not affected by the volume flow and are around 12 s for CF/PEEK and 8 s for CF/PPS.

The temperature gradient between the inductor and opposite side $\Delta T_{s,max}$ is governed by the volume flow and ranges from 64 K (167 l/min) to 93 K (304 l/min) for CF/PEEK

and 66 K to 85 K for CF/PPS. Table 14 summarizes the characteristics of heating with an impinging jet.

Table 14: Times to reach welding temperature and maximum temperature gradient between inductor and opposite side of laminate with surface cooling at inductor side

Distance [mm]	Power [%]	Material	Air volume flow [l/min]	Time to T_w [s]	$\Delta T_{s,max}$ [K]
2	30	CF/PEEK	167	10.5	64
			240	11	80
			304	11	93
		CF/PPS	167	8	66
			240	8	80
			304	8	85

4.2.2. Cross-Sectional Analysis

Figure 29 and Figure 30 show examples of cross sections of inductively heated samples processed at 3mm coupling distance with 20 % generator power because this parameter set shows the cooling effect most distinctively.

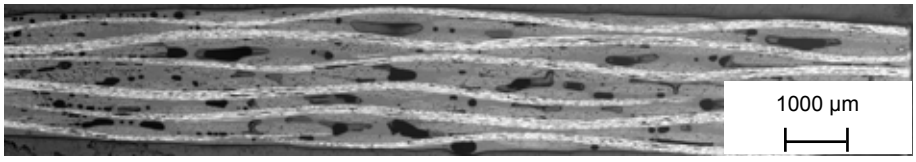

Figure 29: Cross section of induction heating sample (CF/PEEK, 3 mm coupling distance, 20 % generator power)

In Figure 29 voids and delamination between the layers in the sample are visible. By contrast, in Figure 30 the effect of the impinging air jet can be evaluated. The first layers which are in close contact to the impinging jet show no sign of delamination or voids which shows that the temperature did not exceed the melting temperature in this region of the laminate.

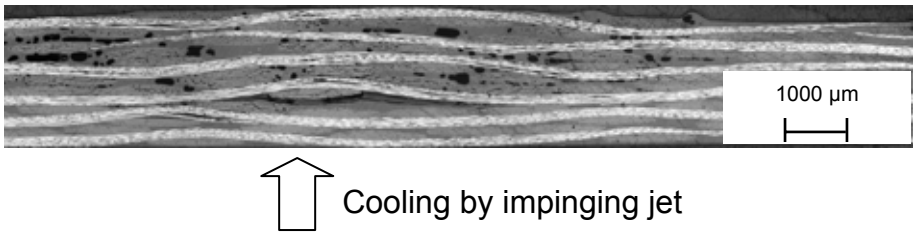

Figure 30: Cross section of induction heating sample (CF/PEEK, 3 mm coupling distance, 20 % generator power, 304 l/min surface cooling on downside)

5. Three-Dimensional Finite Element Induction Heating Model

Due to the complexity of induction heating, process simulation is a powerful tool for process development. In this Chapter, three-dimensional finite elements heating models of static induction heating are developed and validated. Furthermore, a sensitivity analysis is carried out in order to identify the significant processing parameters.

5.1. Underlying Equations

The nominal frequency of the induction generator used in this study is 400 kHz. The resulting wavelength, see Equation (10), is 750 m, which is significantly larger than the composite laminates that have a thickness of a few millimeters. Consequently, a quasi-static approximation can be used and the resulting time-harmonic Maxwell-Ampère formulation is given in Equation (52) [84],

$$\left(\boldsymbol{j}\omega\sigma - \omega^2\varepsilon\right)\boldsymbol{A} + \nabla \times \left(\mu^{-1}\nabla \times \boldsymbol{A}\right) = \boldsymbol{J}_e \tag{52}$$

where **j** is induced current density, ω is angular frequency, ε is electric permittivity, **A** is magnetic vector potential, μ is magnetic permeability and $\mathbf{J}_e$ is external current density.

The thermal model for continuous movement during heating (i. e. for continuous welding of large parts) to be solved is given in Equation (18). For static heating it simplifies to Equation (53),

$$\rho c_p \frac{\partial T}{\partial t} = k\nabla T + Q \tag{53}$$

where ρ is density, c_p specific heat capacity at constant pressure, T is absolute temperature, t is time, k is thermal conductivity, and Q is a heat source.

Due to the architecture of the reinforcement of the material under inspection, sufficient electrical contact between the rovings is assumed and consequently fiber heating is the dominant heating mechanism, see Chapter 2.6.3. Therefore, resistivity is determined by the electrical properties of the fibers, see Equation (44).

Figure 31 gives an overview of the induction heating simulation. After performing a harmonic electromagnetic analysis and determining the eddy current distribution, the transient temperature field is calculated. This is done in individual timesteps t_i, until the heating time t_{ht} is reached.

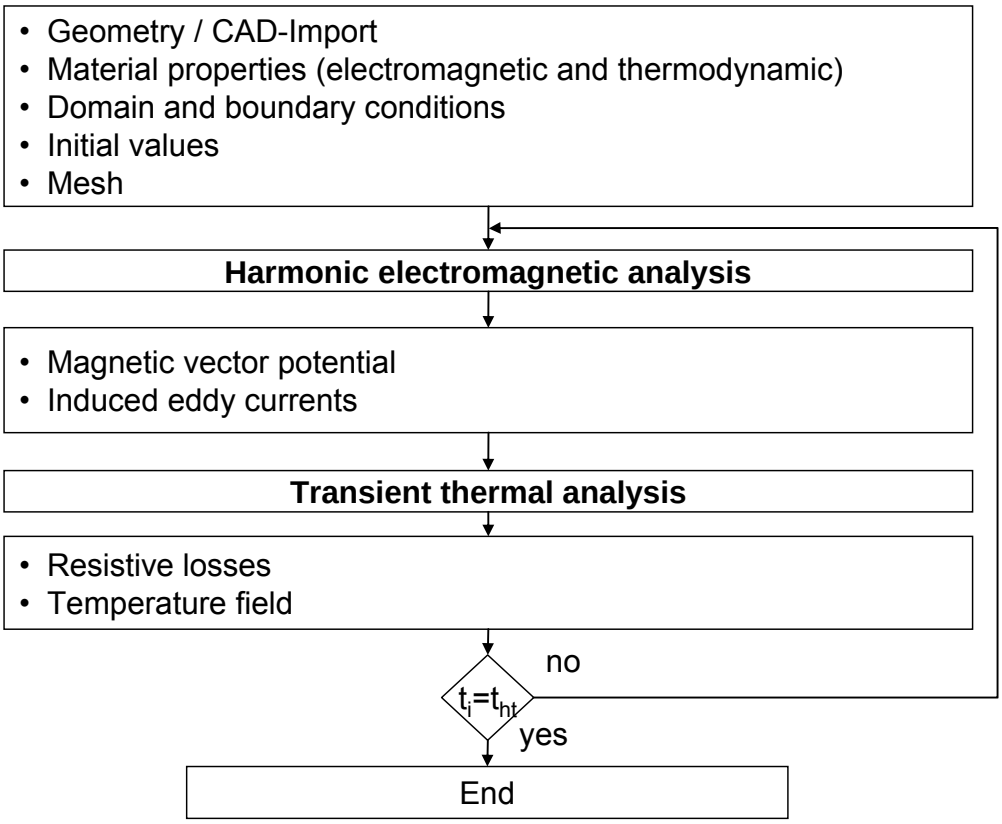

Figure 31: Flow diagram of a typical induction heating simulation

5.2. Simplifications

Reducing the complexity of the physical problem is an important step in the modeling process. Supported by a literature review the following simplifications have been made:

- Latent heat: In several studies, the effect of the latent heat due to crystal melting had a negligible effect on the time to melt of APC-2/PPEK composites [22,93]. It is assumed that this result is tranferable to the composites used in this study. Thus, crystallization kinetics are not implemented into the model.
- Surface roughness: Accounting for the roughness of the contact surface between two adjacent laminates showed no significant influence on the heating model accuracy for power levels from 36 to 120 kW/m^2 [22]. Therefore, perfect contact is implemented.
- Heating mechanism: Resistive heating or fiber heating, respectively, is used as heating mechanism for the woven reinforcement because delamination, which triggers the change of the dominant heating mechanism (see Chapter 2.6.3 and Chapter 3.3.2), is effectively prevented by surface cooling of with an

impinging air jet (see Chapter 4). However, this induces inaccuracies for the model without surface cooling.

- Homogenized material model: Composite materials consist of a large number of elements (e. g. filaments forming the textile structure that is surrounded by polymer matrix). Thus, it is not possible to take the real geometry into account and create a model on the micro-scale. It is rather necessary to use homogenization techniques [83]. In [22] a homogenized material model and a micro model of discrete fiber bundles and matrix, respectively, were compared and similar heating results were found. In this work, the laminates are represented as anisotropic material with homogenized material properties.
- Temperature related material properties: In [22] the use of constant and temperature dependent material properties of APC-2/PEEK for modeling the resistance welding process did not significantly alter the time needed to melt the matrix for power levels above 40 kW/m^2 as both matched the experimental values very closely. The same applied for the resistance values of the heating element. Therefore, constant values are used for the electrical conductivity of the carbon fiber reinforcement.
- Density: The density of the materials is assumed to be constant in the heating simulation.
- Thermal conductivity: Thermal conductivity of composite laminates can be modeled as a constant property [99]. This is supported by the fact that thermal conductivity of the PPS matrix matches the other semi-crystalline thermoplastic materials and is almost independent to temperature changes [95].

5.3. Material Properties

Different properties are necessary to describe the behavior of material subjected to the magnetic field and the resulting heat generation. Where applicable, values where taken from literature; otherwise experimental characterization was applied.

5.3.1. Electromagnetic Material Properties

The electromagnetic properties that are used for quasi-static modeling of induction heating of carbon fiber reinforced thermoplastic composites are [84]:

- Electrical conductivity
- Relative permeability
- Relative permittivity

In general, carbon fiber reinforced composites with woven reinforcement can be treated as anisotropic homogeneous material with respect to electromagnetic properties [94], having no electrical conductivity in thickness direction [83]. The electrical conductivity for both CF/PPS and CF/PEEK can then be calculated by the rule of mixtures if only the fibers in the respective direction are considered, see Equation (54) and Equation (55) [94],

$$\sigma_x = \sigma_f \cdot \phi_{fx} + \sigma_m \cdot \left(1 - \phi_{fx}\right) \tag{54}$$

$$\sigma_y = \sigma_f \cdot \phi_{fy} + \sigma_m \cdot \left(1 - \phi_{fy}\right) \tag{55}$$

where σ_x and σ_y are electrical conductivity of composite in x- and y-direction, σ_f is electrical conductivity of fiber, σ_m is electrical conductivity of matrix, and Φ_{fx} and Φ_{fy} are fiber volume content in x- and y-direction.

The input values for calculating the electrical conductivity as well as numbers for relative permeability and permittivity were taken from literature. The electrical properties are summarized in Table 15 and Table 16.

Table 15: Electrical conductivity of the materials used [94-96]

Property	PPS	PEEK	CF
Electrical conductivity [S/m]	10^{-13}	10^{-14}	$55.56 \cdot 10^{3}$

Table 16: Electrical properties of CF/PPS and CF/PEEK laminates [36,50,94-96]

Property	CF/PPS	CF/PEEK
Fiber volume content in x- direction [%]	25	25
Fiber volume content in y- direction [%]	25	25
Calculated electrical conductivity in x-direction [S/m]	$13.89 \cdot 10^3$	$13.89 \cdot 10^3$
Calculated electrical conductivity in y-direction [S/m]	$13.89 \cdot 10^3$	$13.89 \cdot 10^3$
Relative permeability [H/m]	1	1
Relative permittivity [F/m]	3.7	3.7

Additionally, electrical properties for the induction coil (copper) and surrounding air are needed, see Table 17. For numerical stability reasons, the air is attributed a low electrical conductivity [84].

Table 17: Electrical properties of additional materials [97]

Property	Unit	Air	Copper
Electrical conductivity	S/m	10	$5.99 \cdot 10^7$
Relative permeability	H/m	1	1
Relative permittivity	F/m	1	1

5.3.2. Thermal Material Properties

The following properties are used for thermal modeling of the heating step:

- Density
- Heat capacity
- Thermal conductivity

The density is assumed to be constant in the temperature range under analysis in the model.

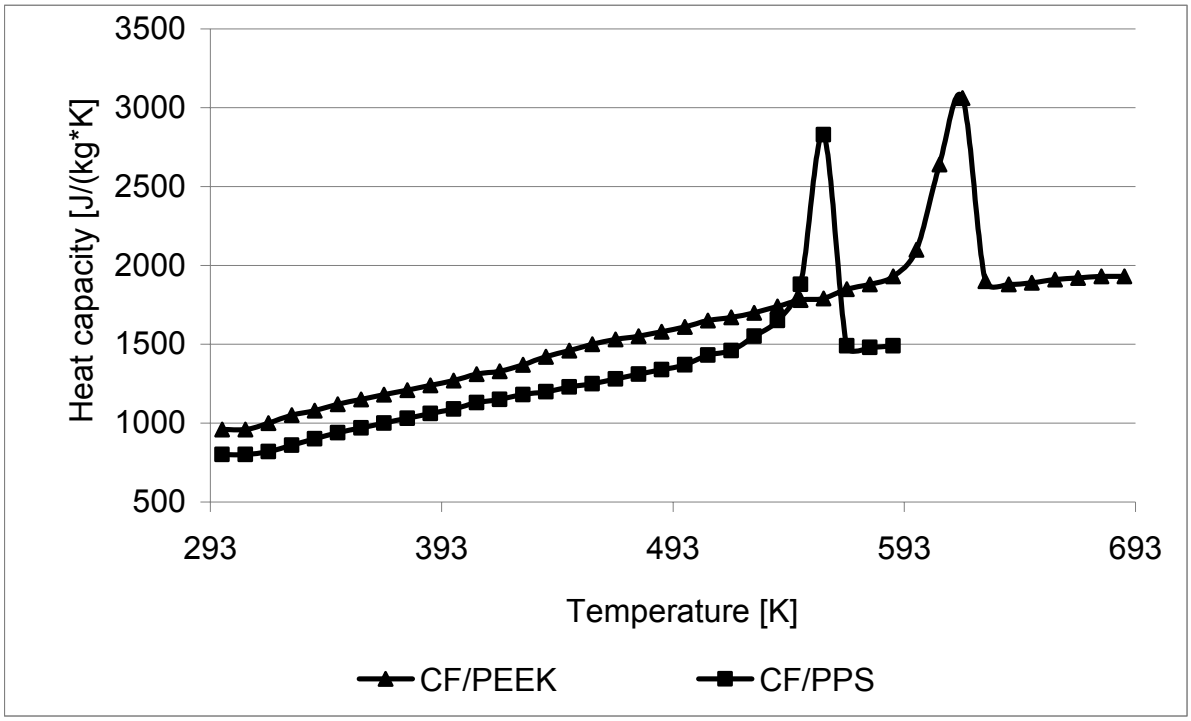

Figure 32: Heat capacity at constant pressure of CF/PEEK and CF/PPS composites

Due to the semi-crystalline matrix polymers the heat capacity undergoes significant changes, especially around the crystallite melting temperature [74]. For both laminates the heat capacity at constant pressure was measured in a Mettler Toledo DSC 821 with sapphire as reference material. The resulting graphs are given in Figure 32. From these results tables with temperature dependent heat capacity were generated and linear interpolation between the values was used.

Due to marked differences in thermal conductivity in-plane and normal, an anisotropic material model is used for thermal conductivity. Similar to the electrical properties, respective values were calculated by the rule of mixture, or the series model, respectively.

A modified series model for the in-plane thermal conductivity (x- and y-direction) accounting for thermal conductivity both parallel and perpendicular to the fibers is derived from Equations (56) and (57). The matrix is assigned each with 50 % in parallel and perpendicular direction, respectively.

$$k_x = \frac{k_{f\parallel} \cdot \phi_f + k_m \cdot (1-\phi_f)}{2} + \frac{\left(\frac{\phi_f}{k_{f\perp}} + \frac{1-\phi_f}{k_m}\right)^{-1}}{2} \tag{56}$$

$$k_y = \frac{k_{f\parallel} \cdot \phi_f + k_m \cdot (1-\phi_f)}{2} + \frac{\left(\frac{\phi_f}{k_{f\perp}} + \frac{1-\phi_f}{k_m}\right)^{-1}}{2} \tag{57}$$

For the out-of-plane thermal conductivity Equation (58) is used.

$$k_z = \left(\frac{\phi_f}{k_{f\perp}} + \frac{1-\phi_f}{k_m}\right)^{-1} \tag{58}$$

Table 18 to Table 20 summarize the thermal properties used for modeling induction heating. The induction coil is not part of the thermal model; therefore no thermal properties are given.

Table 18: Thermal properties of the materials used [22,95,98,100]

Property	Unit	PPS	PEEK	CF
Thermal conductivity	W/(m·K)	0.25	0.25	$\parallel$ 9.1 $\perp$ 0.43
Density	Kg/m^3	1350	1300	1790

Table 19: Properties for thermal simulation of CF/PPS and CF/PEEK laminates

Property	Unit	CF/PPS	CF/PEEK
Fiber volume content in x-direction	%	25	25
Fiber volume content in y-direction	%	25	25
Calculated thermal conductivity in x-direction	W/(m·K)	2.50	2.50
Calculated thermal conductivity in y-direction	W/(m·K)	2.50	2.50
Calculated thermal conductivity in z-direction	W/(m·K)	0.32	0.32
Density	Kg/m^3	1570	1545

Table 20: Thermal properties of additional material [89,97]

Property	Unit	Air
Thermal conductivity	W/(m·K)	0.025
Density	Kg/m^3	1.217
Heat capacity	J/(kg·K)	1006

5.4. Additional Input Values

5.4.1. Coil Current

The coil current relates the induction generator power settings to the model. The generator unit can be set by percentage of power output. Equivalent coil current values related to these power settings of the induction generator, see Table 21, were taken from [101]. Although measured for a different model of the same generator series they are directly applicable to the equipment used [102].

Table 21: Effective coil currents for different power settings

Power setting [%]	10	20	30
Coil current [A]	131.97	193.5	241.54

5.4.2. Convective and Radiation Heat Transfer Coefficients

Heat transfer coefficients following the methodology presented in [87] related to the geometry and ambient conditions are calculated, see Table 22. Fluid properties for air were taken from [87].

Table 22: Heat transfer coefficients for single sheet heating model

Temperature [°C]	Vertical faces [W/(m^2·K)]	Horizontal face, upside [W/(m^2·K)]	Horizontal face, downside [W/(m^2·K)]
40	23.5	5.2	4.0
100	28.8	6.9	5.2
140	30.8	7.4	5.6
180	32.4	7.8	5.9
260	34.9	8.4	6.4
300	36.0	8.6	6.5
380	37.8	9.0	6.8
480	39.8	9.3	7.1

It has to be considered that these values represent averaged heat transfer coefficients for ideally isothermal bodies whereas in induction heating typically non-isothermal temperature profiles occur. However, these values are suitable for an estimation.

Surface cooling with impinging jets involves significantly higher convection coefficients, which are determined by additional parameters such as nozzle type, nozzle diameter, standoff distance, surface area, and volume flow [87]. Table 23 presents the heat transfer coefficients calculated using the approach outlined in [87] for a single round nozzle with a diameter of 6 mm, standoff distance of 17 mm, a surface area radius of 40 mm, and variable air volume flow of 167 l/min, 240 l/min, and 304 l/min.

Table 23: Heat transfer coefficients given with respect to both temperature and volume flow of impinging air jet

Temperature [°C]	Volume flow of impinging air jet [l/min]		
	167	240	304
	[W/(m^2·K)]		
25	313	401	471
95	302	386	453
135	296	377	443
175	290	370	433
255	280	356	418
295	276	350	410

For an estimation of radiation heat transfer, surface-to-ambient heat transfer is implemented with emissivity ε_e of carbon fiber reinforced composites of 0.95 [87,89,103]. Equation (20) comprises the related terms for convection and radiation.

5.5. Single Sheet Induction Heating Model

Induction heating of a single composite sheet is used for evaluation of the material properties and the heating model. Laminates made from both CF/PPS and CF/PEEK are modeled and compared to experimental results.

5.5.1. Geometry

The composite sheet in the model has dimensions of 100 mm length, 100 mm width, and 2 mm thickness. A volume model of the two-turn pancake induction coil used for the characterization experiments (outer diameter 25 mm, inner diameter 13.4 mm, tube diameter 3 mm), is applied at different coupling distances, see Figure 33. The heating head of the generator is not modeled; instead the connectors are closed to allow the current to flow. Due to the connector geometry approximately one quarter of one turn has only one turn, compare Figure 14.

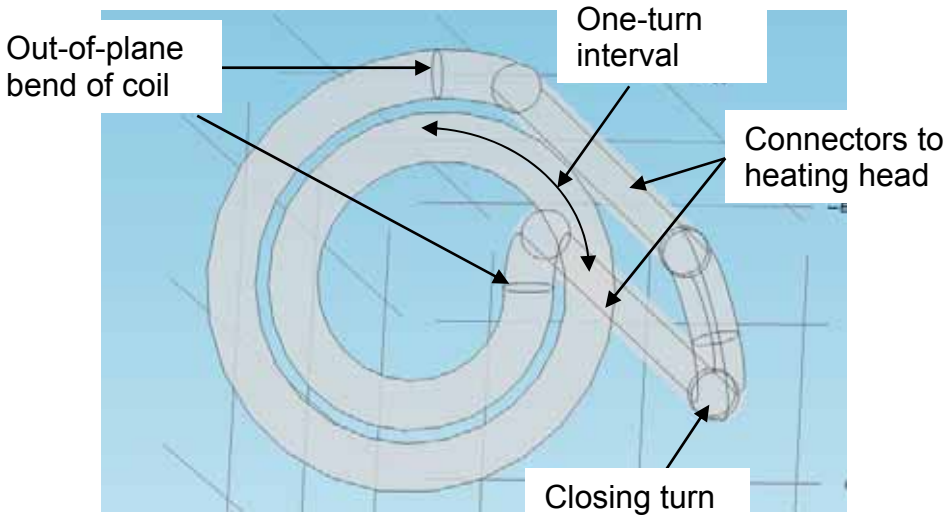

Figure 33: Induction coil model geometry

The air domain surrounding the induction heating setup is a cube with a 150 mm edge length. An overview is shown in Figure 34.

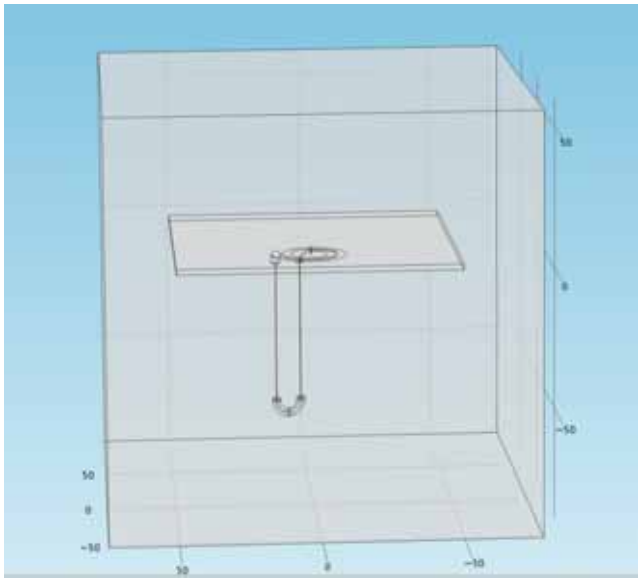

Figure 34: Geometry of single sheet model

5.5.2. Material Properties and Boundary Conditions

Different materials are used in the model. The material properties of copper, air, and CF/PPS as well as CF/PEEK composites are attributed to the coil, air domain, and sheet, respectively; see values given in Table 16 to Table 19

The coil current, see Table 21, is applied via a surface current boundary. The outer faces of the air domain represent a magnetic insulation boundary, i. e. no magnetic flux over these boundaries is possible. The induction coil is loaded with a surface current boundary. For the thermal model, the outer faces of the composite sheet are at-

tributed both a convective cooling and a surface-to-ambient radiation boundary condition, see Table 22.

5.5.3. Mesh

At least two linear elements per skin depth are necessary to capture the variation of the magnetic field [84]. The skin depth was calculated as 4.7 mm, using Equation (4), and values from Table 16.

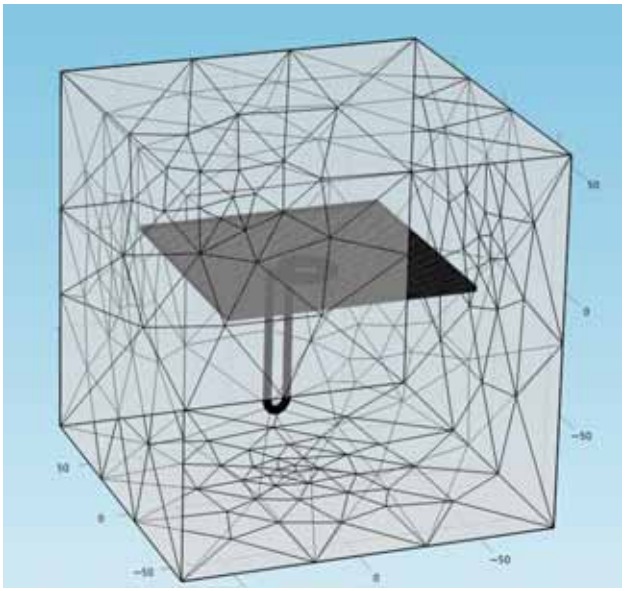

Figure 35: Mesh of single sheet model

The composite sheet was meshed using square elements with 4 elements in thickness direction. For compatibility reasons with the tetrahedral mesh of the air domain, the surface of the composite sheet was converted to triangles. Since only boundary conditions need to be applied to the coil and internal heating effects in the coil itself are not required, the surface of the coil was also meshed with triangles, whereas the air domain was meshed using tetrahedral elements. Both the magnetic vector potential and the temperature are discretized using quadratic elements. Figure 35 shows the resulting mesh of the model.

5.5.4. Validation

For validation of the induction heating model the parameters used for experimental characterization, see Table 4, were used as input parameters. Point temperature readings identical to the induction heating experiments, see Figure 15, and areal images of the in-plane heat distribution are used for evaluation of the accuracy of the model.

Through-the-Thickness Temperature Distribution

Figure 36 to Figure 38 show the comparison between experimental and simulation results of the 2 mm coupling distance and the 10 %, 20 %, and 30 % generator power for CF/PEEK. The graphs for the 3 mm coupling distance for CF/PEEK as well as the graphs for the 2 mm and the 3 mm coupling distance for CF/PPS are given in Figure 73 to Figure 81 in the Appendix,

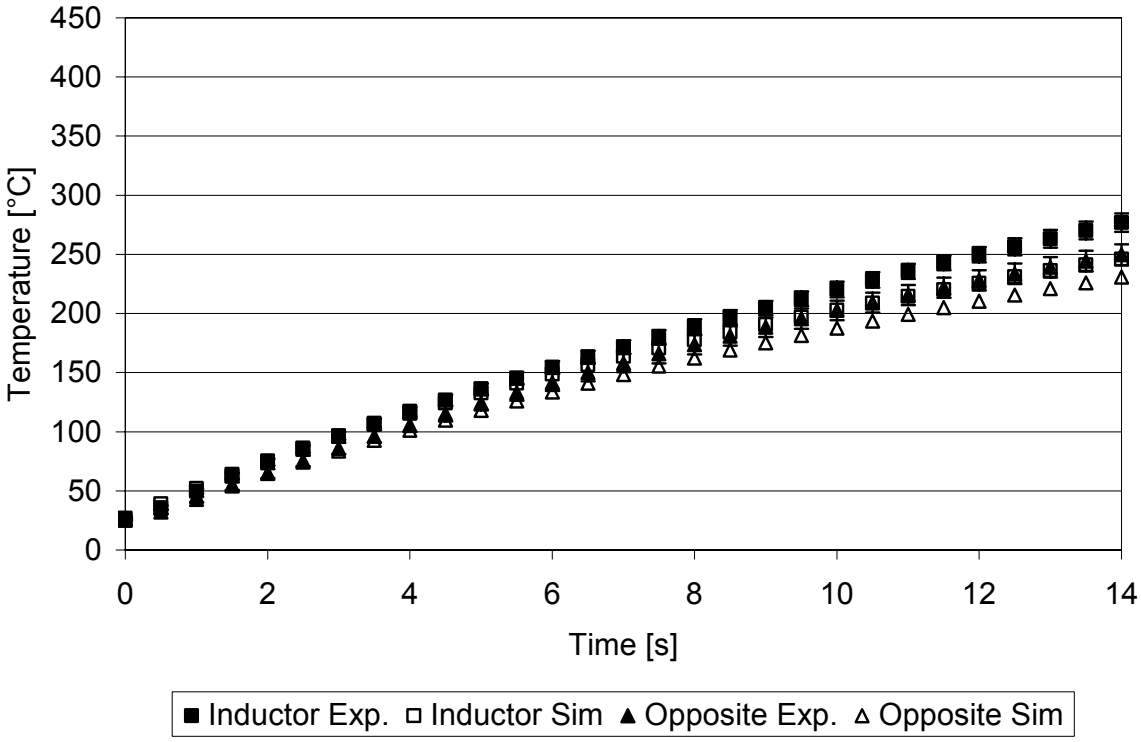

Figure 36: Validation of induction heating simulation, CF/PEEK, 2 mm coupling distance, 10 % generator power

The temperature curves show a good correlation between the experiments and the simulations despite some case, where the temperature gradient between the inductor and opposite side is underestimated.

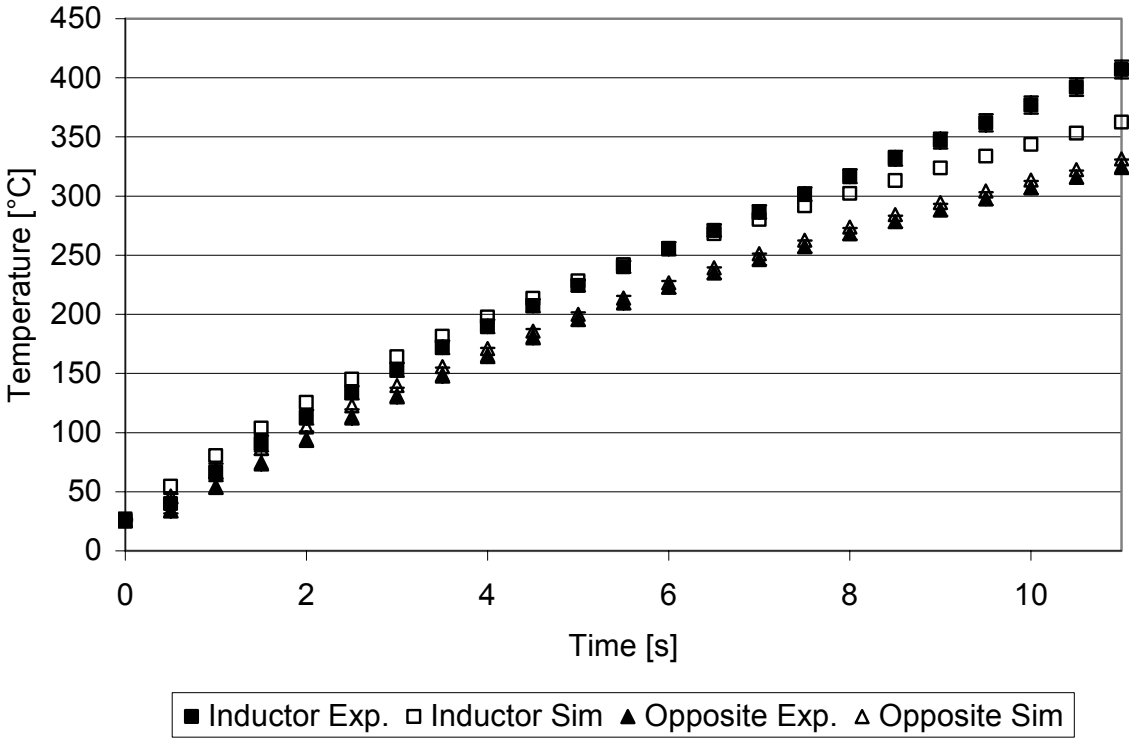

Figure 37: Validation of induction heating simulation, CF/PEEK, 2 mm coupling distance, 20 % generator power

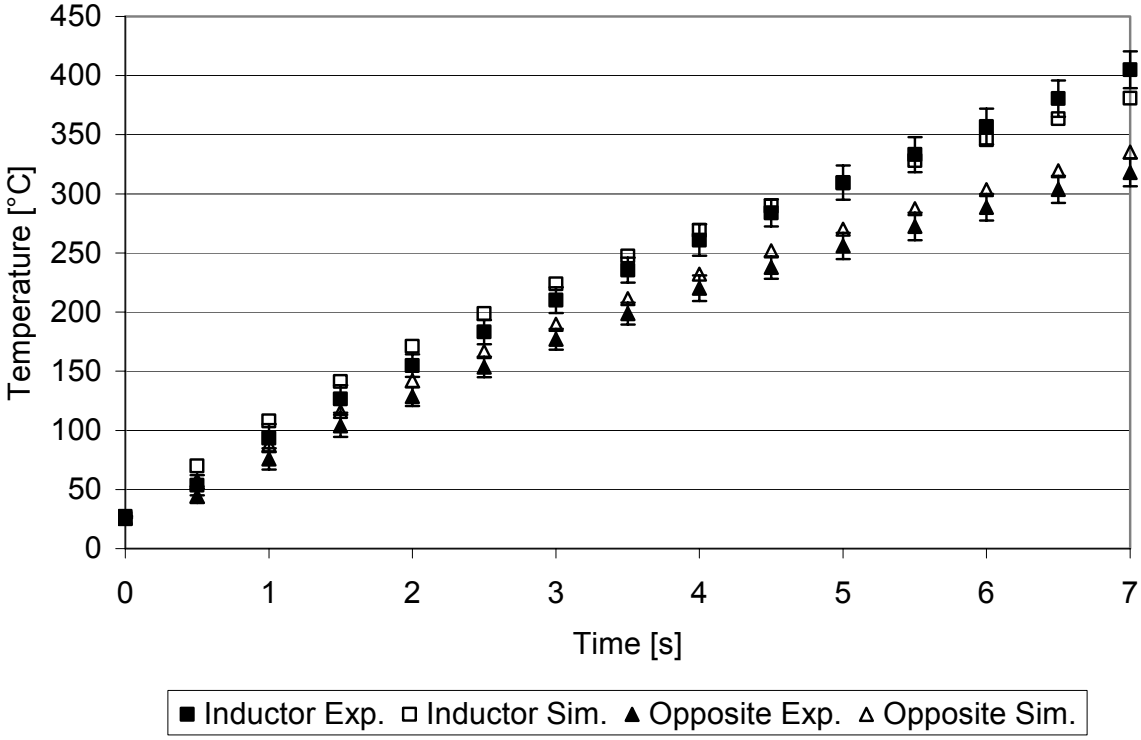

Figure 38: Validation of induction heating simulation, CF/PEEK, 2 mm coupling distance, 30 % generator power

Table 24 summarizes the maximum deviation at welding temperature t_w. For CF/PEEK the deviation is constantly negative whereas for CF/PPS it is positive. Except one parameter set (CF/PPS, 3 mm coupling distance, 30 % generator power) with a deviation of 25 % all curves show deviations below 20 %, mostly between 10 % and 20 %. Two parameter sets (CF/PEEK, 2 mm coupling distance, 30 % generator power, and CF/PPS, 2 mm coupling distance, 10 % generator power) are below 10 % deviation. Comparing the coupling distances, the results for 2 mm exhibit a lower deviation for both CF/PEEK and CF/PPS (absolute average of 10 %) compared to the 3 mm coupling distance (absolute average of 17 %).

Table 24: Temperature deviation between experimental and simulation single sheet heating

Coupling Distance [mm]	Power [%]	CF/PEEK	CF/PPS
		ΔT [%]	ΔT [%]
2	10	-11	6
	20	-11	15
	30	-6	12
3	10	-13	10
	20	-17	20
	30	-14	25

In-Plane Temperature Pattern

Table 25 shows the comparison of the opposite side surface heating patterns of the experiments and the respective model for CF/PEEK at 2 mm coupling distance in two second intervals. The results for CF/PEEK at 3 mm coupling distance as well as for CF/PPS at 2 mm and 3 mm coupling distance are given in Table 31 to Table 33 in the Appendix. Similar to the through-the-thickness validation results, the temperature patterns show good correlation between experiment and model and the overall characteristics such as the cold spot in the center, hot region in the area of the global current loop and colder surrounding material are fully met. The effect of the coil geometry having one quarter with only one effective turn is also modeled accurately for the 2 mm but overestimated for the 3 mm coupling distance. The shape of the heating

pattern shows variations. The experimental shape is more square-like whereas the modeled one is circular, which is founded in the homogenized material model. Due to the heating model that is implemented in the simulation, junction heating effects are not accounted for.

Table 25: Comparison of heating patterns of experimental characterization and induction heating model, CF/PEEK, 2 mm coupling distance

Time [s]	Power [%]					
	10		20		30	
	Experiment	Model	Experiment	Model	Experiment	Model
2	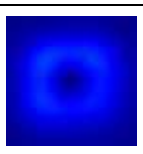	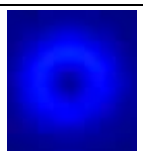	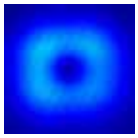	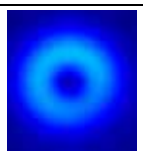	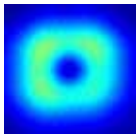	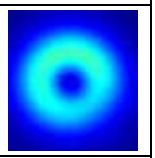
4	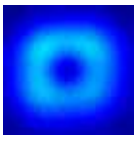	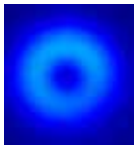	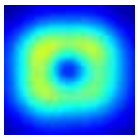	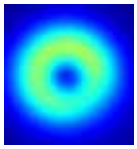	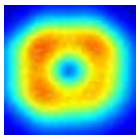	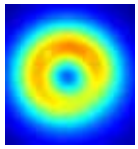
6	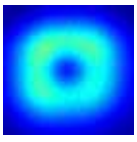	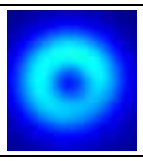	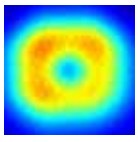	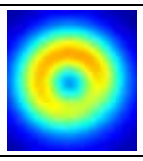	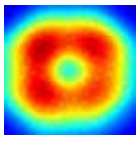	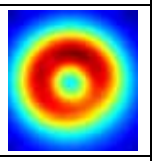
8	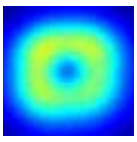	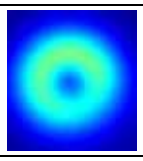	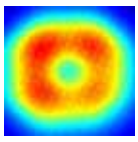	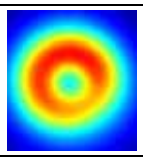		
10	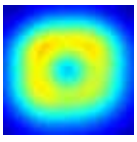	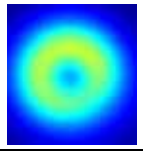	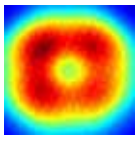	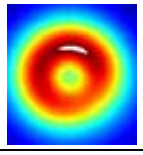		
12	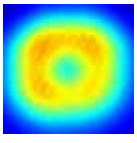	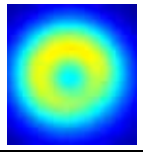				
14	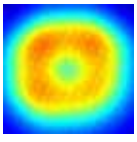	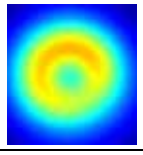				

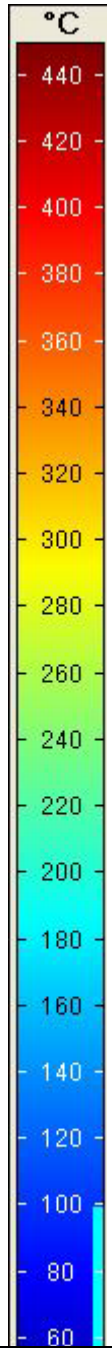

5.6. Sensitivity Analysis

5.6.1. Input Parameters

Numerous properties are needed as input parameters for the induction heating model. Many of these are difficult to measure and reliable data is not always accessible in the open literature. In order to identify the significant parameters that should be measured thoroughly, a sensitivity analysis is performed. Small variations of significant parameters change the result considerably whereas even great variations of non-significant parameters yield no or little impact on the simulation results. Concentrating on the assessment of the significant parameters enables cost and time savings without loss in accuracy of the simulation model. Each parameter is varied by 2.5 %, 5 %, and 10 % around the initial value.

The basis of for the evaluation of the parameter variations on the heating behavior is the induction heating model of CF/PEEK with a 2 mm coupling distance and 30 % generator power. Each parameter was varied according to Table 25 and the mean temperature deviations of the point measurements were normalized with respect to the base model. The results are given in Figure 39 to Figure 47. The input parameters are categorized into four different groups, depending on the maximum mean temperature deviation, having high (> 10 % deviation), medium (5 %< deviation ≤ 10 %), low (1 % < deviation ≤ 5 %), and no significance (≤ 1 % deviation).

Table 26: Parameter variations for sensitivity analysis (Base CF/PEEK laminate, 2mm coupling distance, 30 % generator power)

Variation [%]	Coil current [A]	Electrical conductivity [10^3 S/m]	Rel. permittivity	Rel. permeability	Coupling distance [mm]	Thermal conductivity in-plane [W/m·K]	Thermal conductivity out-of-plane [W/m·K]	Frequency [kHz]	Heat capacity [J/kg·K][2]
-10	217.39	12.50	3.33	0.9	1.8	2.25	0.288	378	864
-5	229.46	13.20	3.515	0.95	1.9	2.375	0.304	399	912
-2.5	235.50	13.54	3.6075	0.975	1.95	2.4375	0.312	410	936
0	241.54	13.89	3.7	1	2	2.50	0.32	420	960
+2.5	247.58	14.24	3.7925	1.025	2.05	2.5625	0.328	431	984
+5	253.62	14.58	3.885	1.05	2.1	2.625	0.336	441	1008
+10	265.69	15.28	4.07	1.1	2.2	2.75	0.352	462	1056

5.6.2. Results

Coil current

Figure 39 shows the influence of the coil current, which has a disproportionately high effect on the mean temperature deviation. A variation of 10 % of the current yields a mean deviation of approximately 13 %. This effect on both the inductor and the opposite side is almost identical. Thus, the coil current is a parameter of high significance for the induction heating simulation.

Electrical conductivity

Figure 40 illustrates the effect of variations of the electrical conductivity, which is disproportionately low. The maximum mean temperature deviation for a 10 % variation is between 4 % and 5 %. Positive parameter variations yield comparable deviations for the inductor and opposite sides, whereas negative variations show differences

[2] The values for heat capacity given in Table 26 are exemplary for room temperature. For the simulations temperature dependent variations of the initially generated tables, see Chapter 5.3.2, were used.

with the inductor side having a slightly higher deviation. Consequently, the electrical conductivity may be categorized as parameter of medium significance.

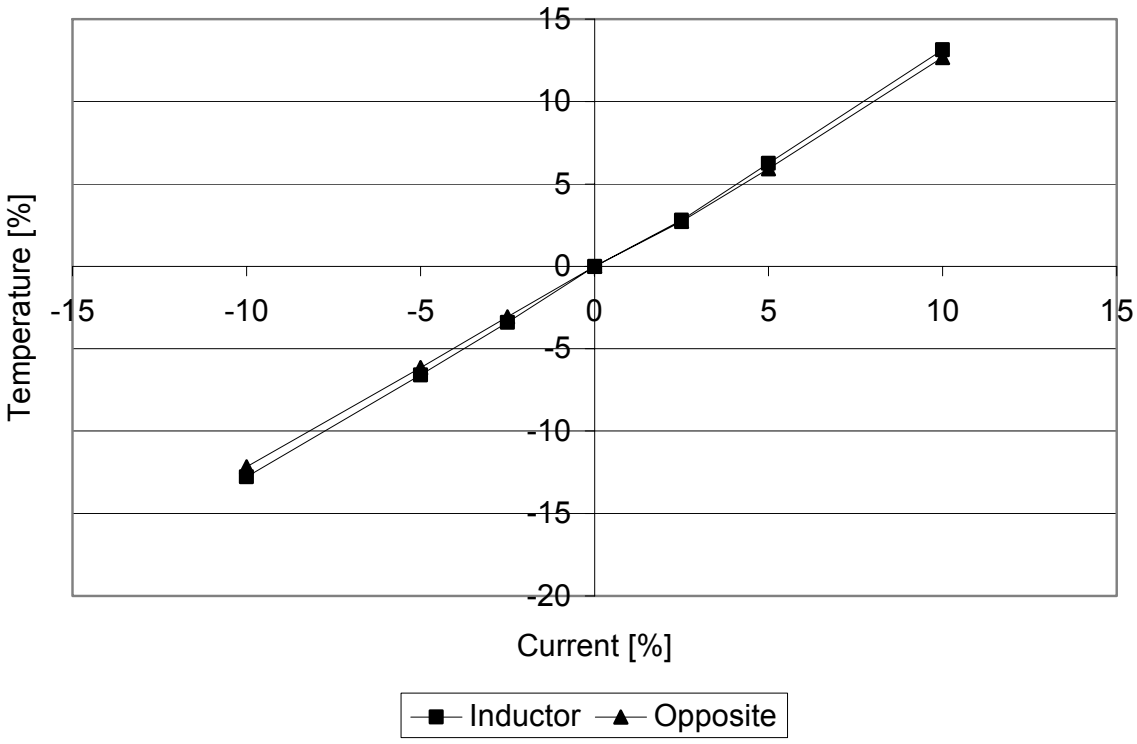

Figure 39: Sensitivity analysis of coil current

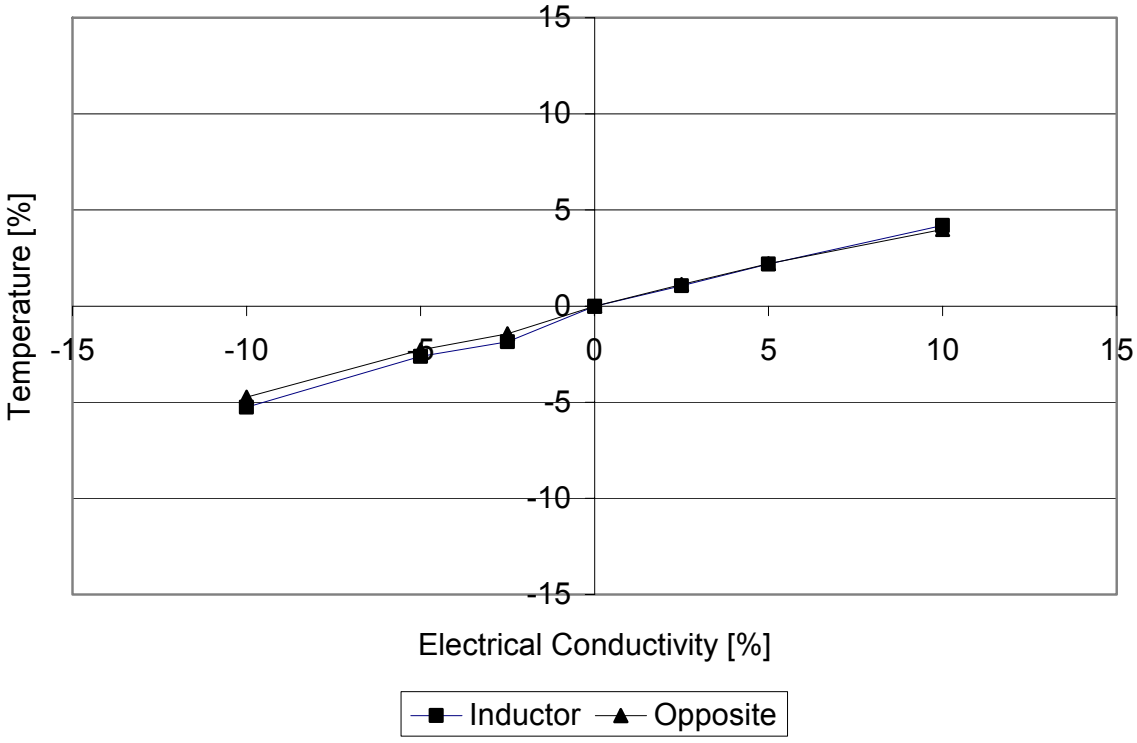

Figure 40: Sensitivity analysis of electrical conductivity

Relative permittivity

Figure 41 presents the effect of the relative permittivity, which is negligible. Variations in the defined range of -10 % to +10 percent show no influence on the mean temperature deviation.

Relative permeability

The impact of the relative permeability is illustrated in Figure 42. The significance of this parameter is low, yielding a maximum mean temperature deviation of 2 % for a variation of 10 %. However, the effect on the temperature on the inductor side is higher compared to the opposite side.

Coupling distance

The coupling distance is an input parameter of low significance, see Figure 43. The maximum deviation is 3 % for a variation of 10 percent. A non-linearity in the graph can be seen at + 2.5 % variation which is attributed to numerical problems.

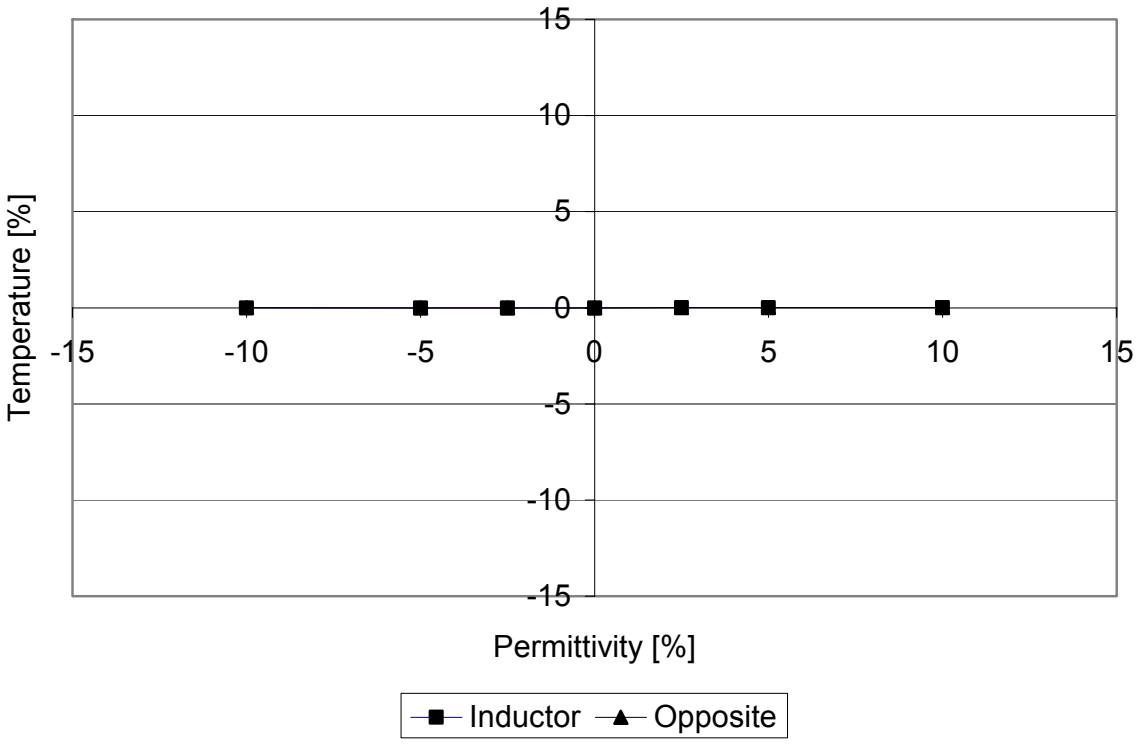

Figure 41: Sensitivity analysis of relative permittivity

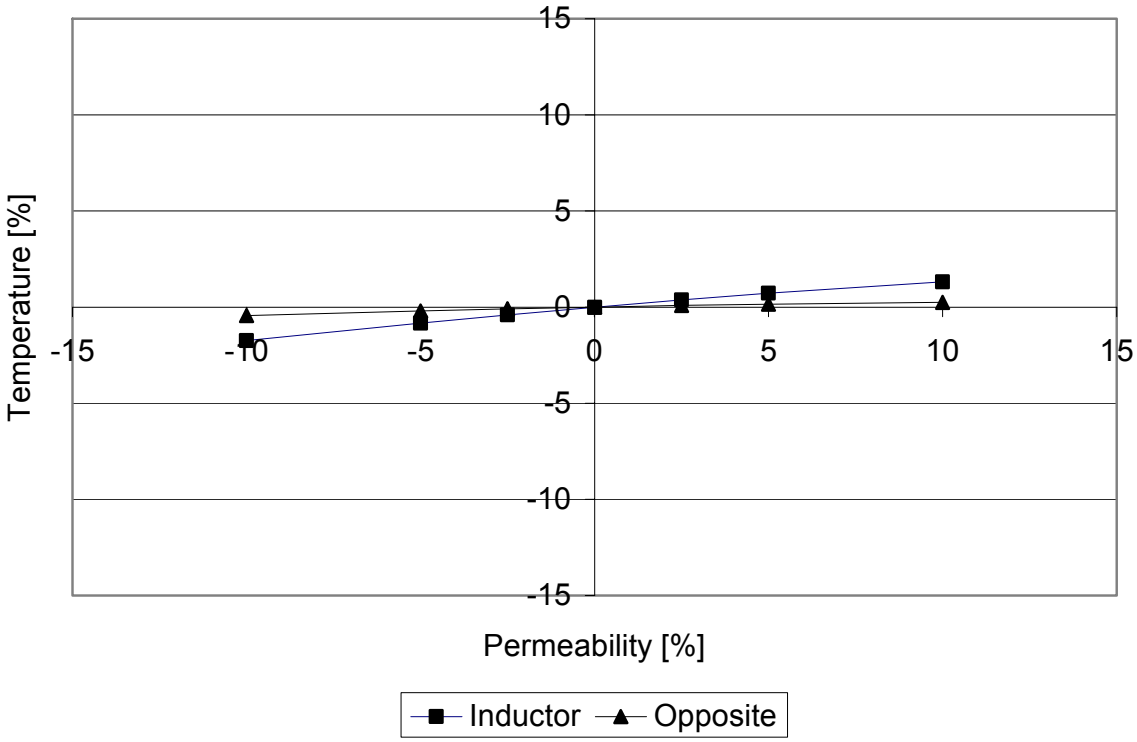

Figure 42: Sensitivity analysis of relative permeability

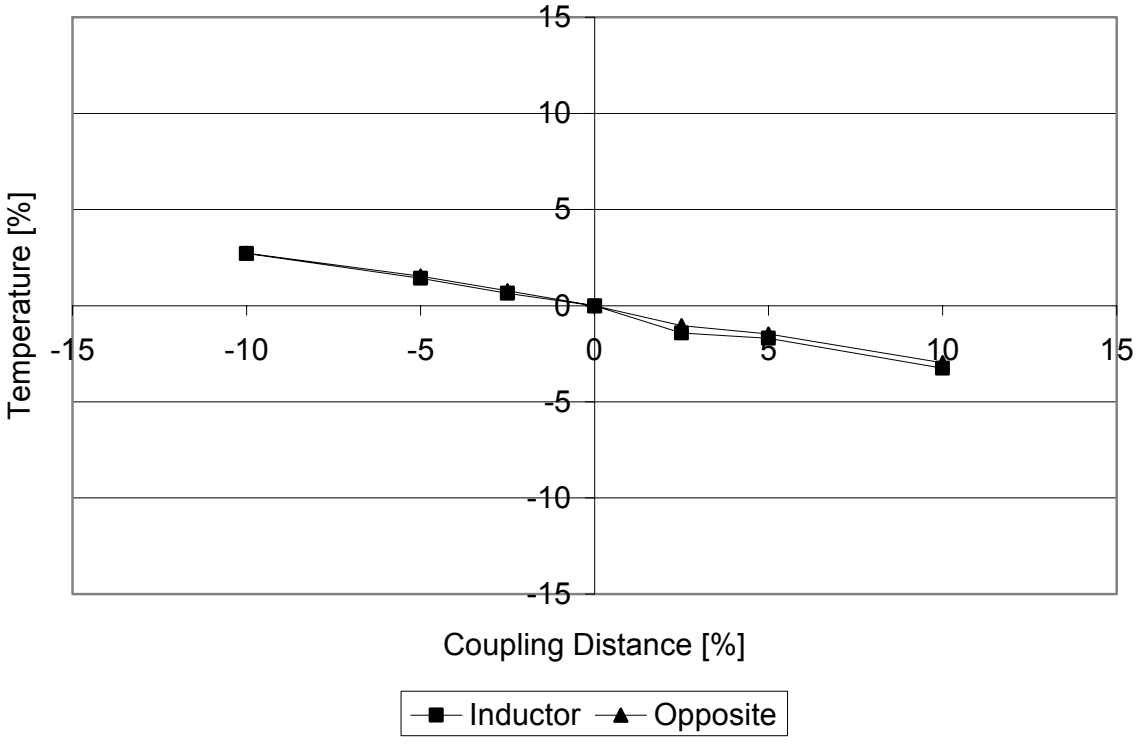

Figure 43: Sensitivity analysis of coupling distance

Thermal conductivity

The thermal conductivity both in- and out-of-plane is a parameter of no significance on the mean temperature deviation (based on the categorization given above), see Figure 44 and Figure 45. The effect of a 10 % variation is a deviation below 1 %.

Frequency

The impact of parameter variations of the field frequency on the mean temperature deviation is given in Figure 46. The maximum deviation is 11 % for a 10 % variation; therefore the frequency is a parameter of high significance.

Heat capacity

Figure 47 illustrates the changes of the mean temperature deviation depending on variations of the heat capacity. It has to be pointed out that the variations were calculated from the temperature related values (see Figure 32 for an examples), which means that the variations illustrated in Figure 47 are based on these values instead of the values at room temperature. A variation of 10 % yields a deviation of 7 %, making the heat capacity a parameter of medium significance in the range under analysis here.

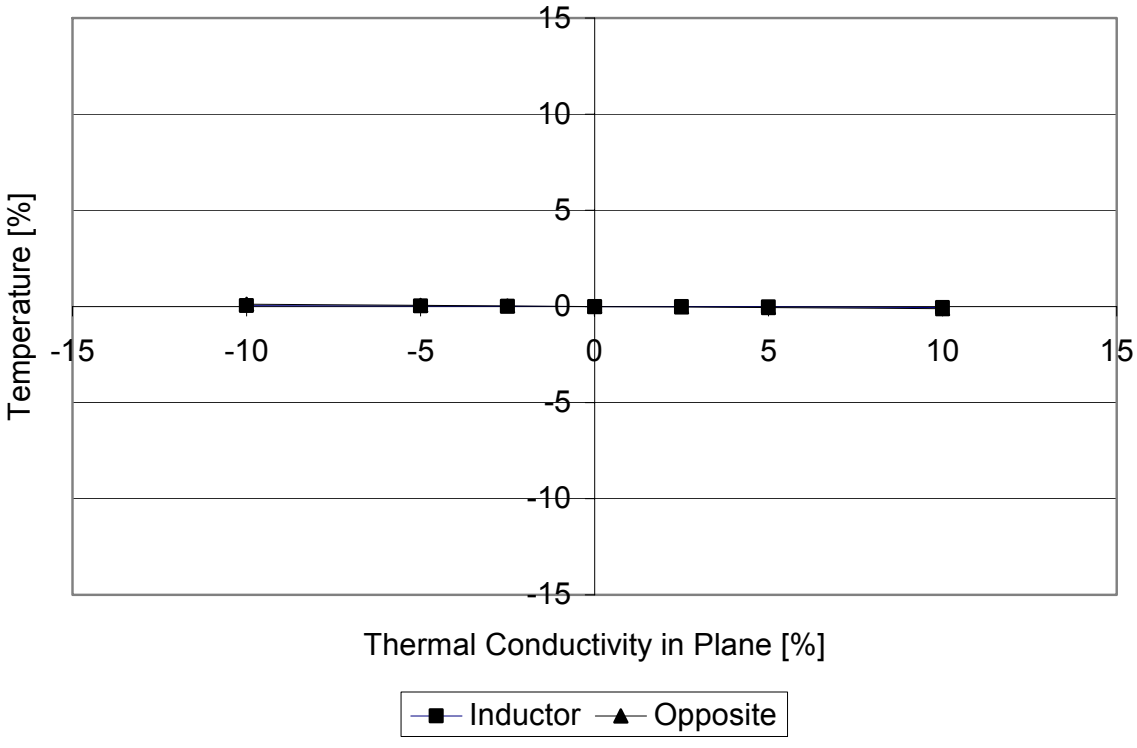

Figure 44: Sensitivity analysis of thermal conductivity in-plane

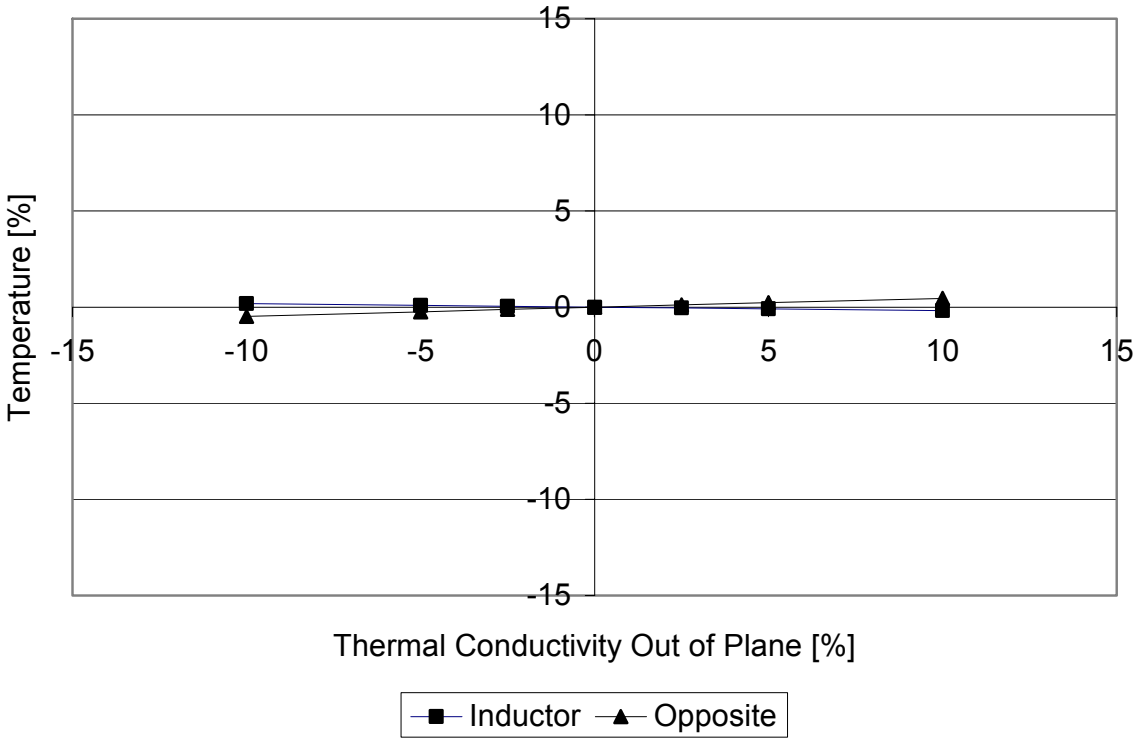

Figure 45: Sensitivity analysis of thermal conductivity out-of-plane

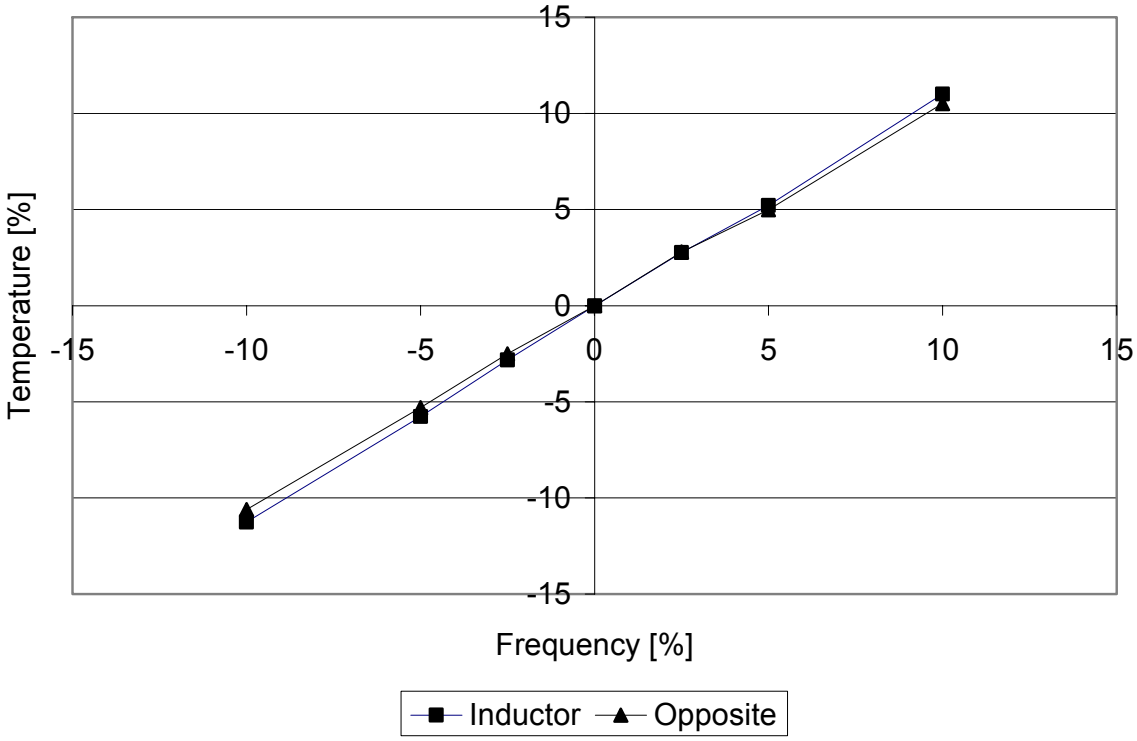

Figure 46: Sensitivity analysis of frequency

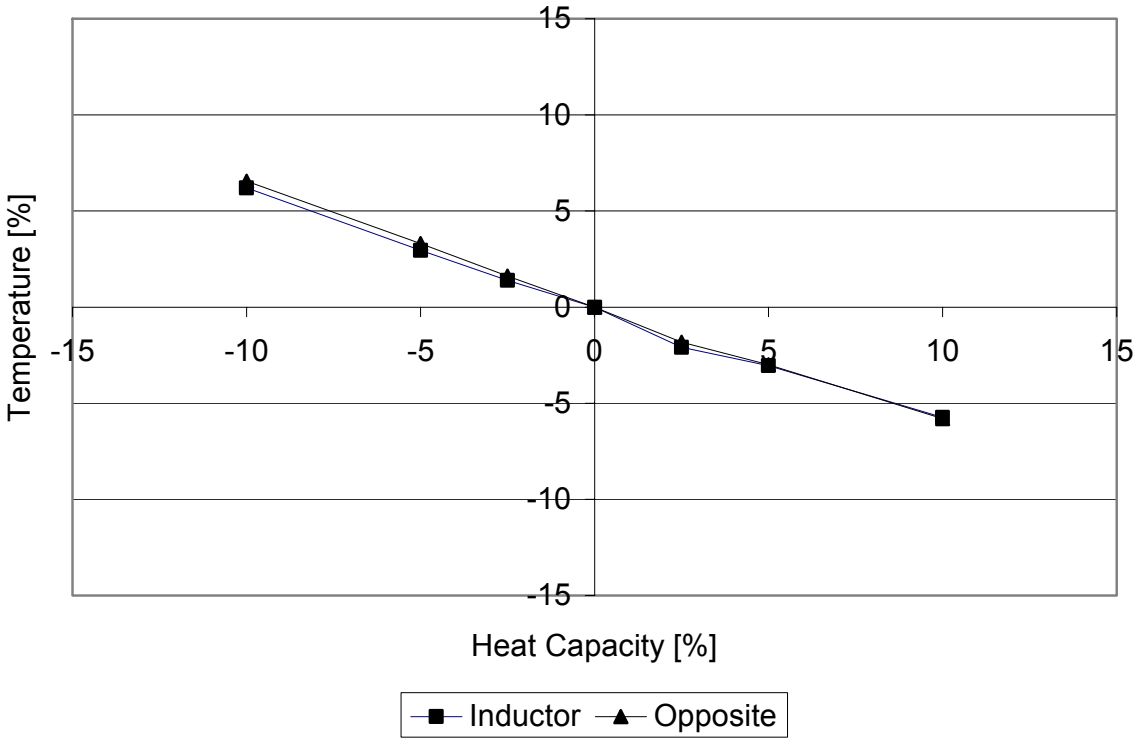

Figure 47: Sensitivity analysis of heat capacity

Table 27 summarizes the effect of the variations of the input parameters and gives their significance for the accuracy of the induction heating model.

Table 27: Effect and significance of input parameters on the mean temperature deviation for CF/PEEK, 2 mm coupling distance, 30 % generator power

	Coil Current	Electrical conductivity	Rel. permittivity	Rel. permeability	Coupling distance	Thermal conductivity in-plane	Thermal conductivity out-of-plane	Frequency	Heat capacity
Maximum deviation [absolute %]	13	5	< 1	2	3	< 1	< 1	11	7
Significance	+++	+	0	+	+	0	0	+++	++

All findings of the sensitivity study are based on the simplifications made in Chapter 5.2. The parameters tested, see Table 26, show an inhomogeneous effect on the model accuracy. The two parameters with the most significant effect on the calcu-

lated temperature are the coil current and the operating frequency, which are machine parameters of the generator. Both show a disproportionately high influence on the induction heating model. Depending on the generator manufacturer, these parameters may be directly accessible to the user or difficult to measure (see [101] for the measurement of the generator current). Arranged in order of significance, see Table 27, the next parameter is the heat capacity with medium significance, which is a material parameter and easy to measure by differential scanning calorimetry. The next parameters are the electrical conductivity, the relative permeability and the coupling distance showing low significance. The first two are material parameters that are assessable with some effort whereas the latter one is a machine parameter that is easy to measure. The parameters which have a negligible effect on the accuracy are the relative permittivity and the thermal conductivity, which are material parameters.

The parameters having the most significant influence are machine parameters which are easily accessible if a suitable generator is available. However, for the generator used in this study, the current is not available and the frequency can only be read out after the experiment. Therefore, a decrease in accuracy of the predicted simulation results is the consequence. The next important parameter is the heat capacity, which is unproblematic to assess. Following this comes the electrical conductivity which is not as easy to measure, see Chapter 2.3.1, but taking into account the low significance it may be adequate to use calculated values for the given system. The same applies to the relative permeability. In contrast, the coupling distance is simple to measure with high accuracy.

Summarizing the observations above, the choice of an appropriate generator model with directly accessible current and frequency values will be the most efficient way to yield high accuracy, especially in combination with easy to perform DSC-measurements of the heat capacity.

5.7. Current Density and Volumetric Heating

A general characteristic of the susceptorless induction heating process is the strong localization of the heating in the laminate. Figure 49 shows a cross section of the induced current density in the laminate; see Figure 48 for the position of the plane. It has to be noted that the plane is in the transitional zone between the in-plane and the out-of-plane parts of the coil, which is at the out-of-plane bend of the coil tube. Start-

ing here, approximately one quarter turn of the coil has only one effective turn, see Chapter 3.2, and consequently shows a different heating effect, with lower induced current densities and power dissipation.

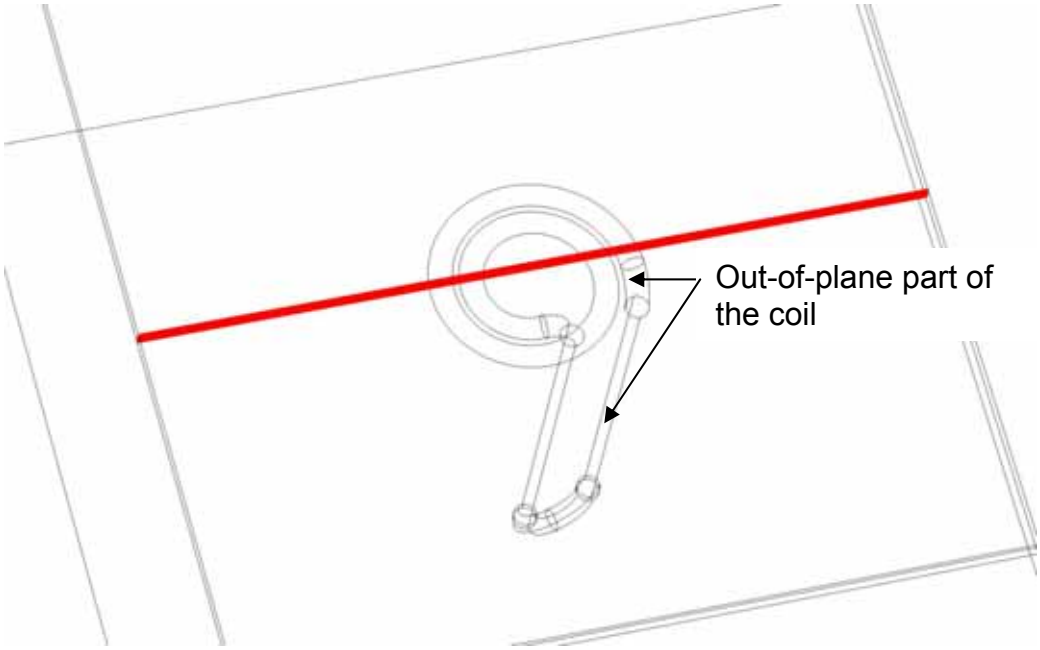

Figure 48: Position of cut plane

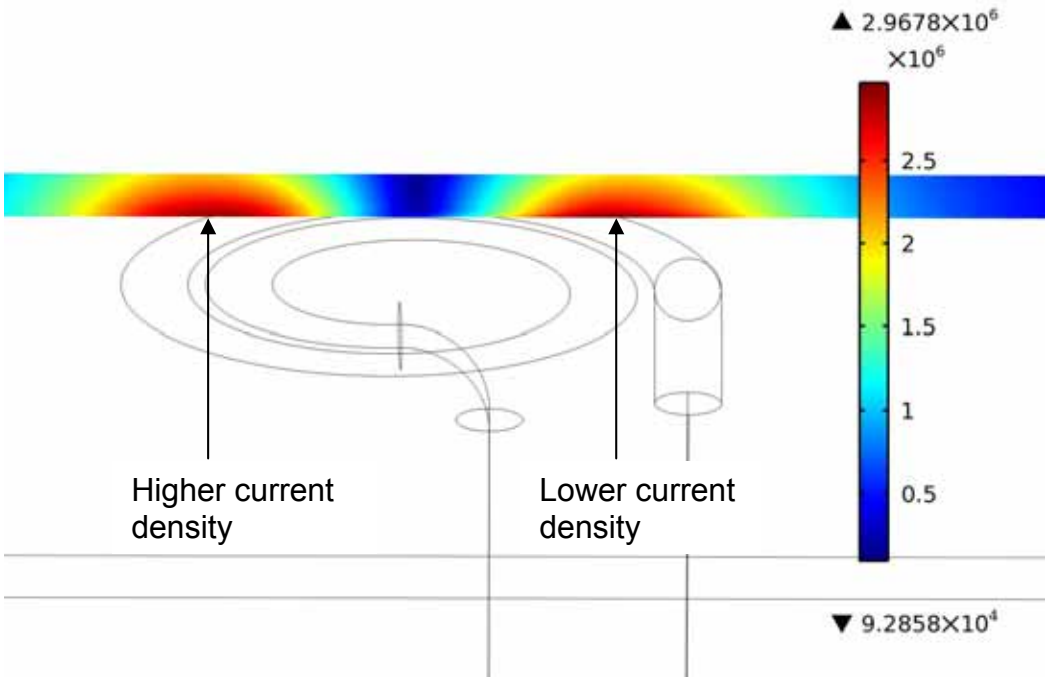

Figure 49: Induced eddy current density [A/ m^2]

The highest current density is in the areas closest to the coil, which is in the global current loop, with a maximum value of approximately $3 \cdot 10^6$ A/m^2. Additionally, the effect of the out-of-plane parts of the coil is visible. The right side of the plane (in the

transitional zone between one and two effective turns), the average current density is lower.

The power dissipation distribution is comparable to the current density distribution, see Figure 50. Analogous, the maximum heating is present in the area below the coil tube, which is in the global current loop with a maximum value of approximately $3.2 \cdot 10^8$ W/m^3.

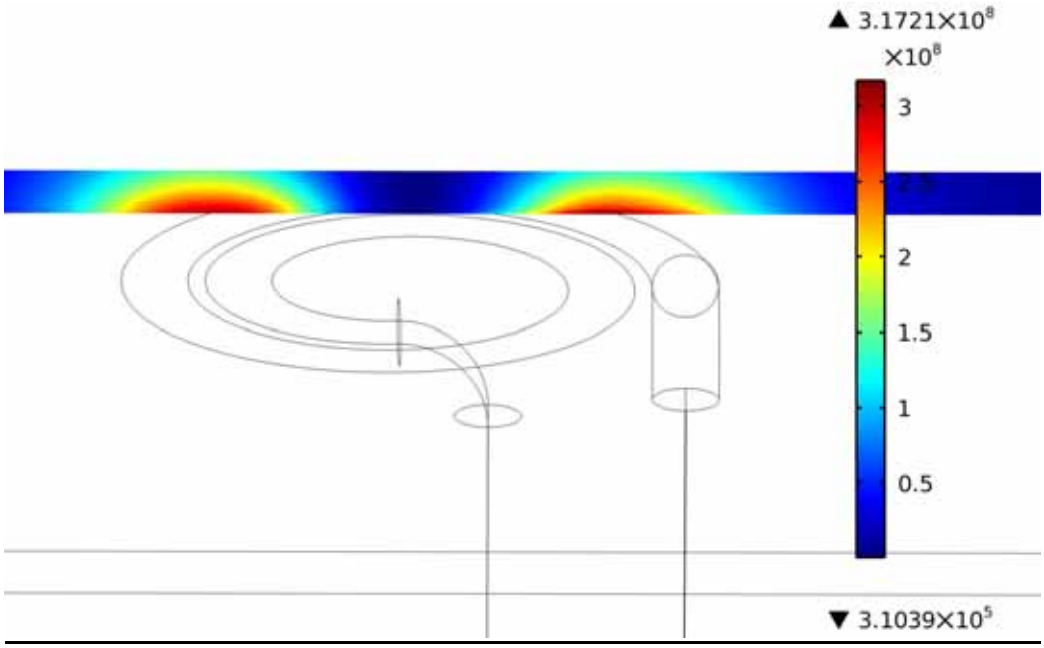

Figure 50: Total power dissipation in the laminate [W/m^3]

5.8. Edge Effect

In order to analyze the edge effect the single sheet induction heating model was applied. The pancake coil was positioned with three different displacements (8.5 mm, 13.5 mm, and 18.5 mm) between the outer edge of the coil and the laminate, see Figure 51. All the other input parameters, such as material properties or boundary conditions were identical to the single sheet model, see Chapter 5.5.

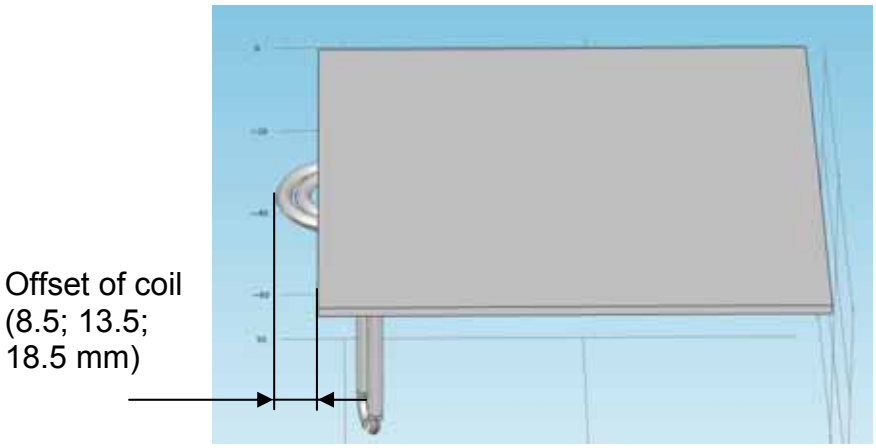

Figure 51: Displacement between coil and laminate in edge effect model

Figure 52 to Figure 54 show the surface power dissipation on the inductor side and the temperature after 1 s heating time. Additionally, the surface current density is indicated by arrows, which have lengths proportional to the magnitude of the density. The most distinct edge effect, characterized by high heating rates and temperature gradients, is visible for 8.5 mm displacement, where more than 50 % of the coil area covers the laminate. The power dissipation of $6.1 \cdot 10^8$ W/m^3 is almost double of the power dissipation without coil displacement, which yields $3.2 \cdot 10^8$ W/m^3, see Figure 50. In case of 13.5 mm displacement, which correlates with approximately 50 % of the coil area covering the laminate, the power dissipation and the temperature are lower compared to 8.5 mm displacement. The power dissipation is $2.6 \cdot 10^8$ W/m^3 and thus lower compared to the non-displaced case. For 18.5 mm displacement, which means that less than 50 % of the coil cover the laminate the power dissipation is considerably lower, showing a maximum of $3.7 \cdot 10^7$ W/m^3, which is around one magnitude lower than the non displaced case.

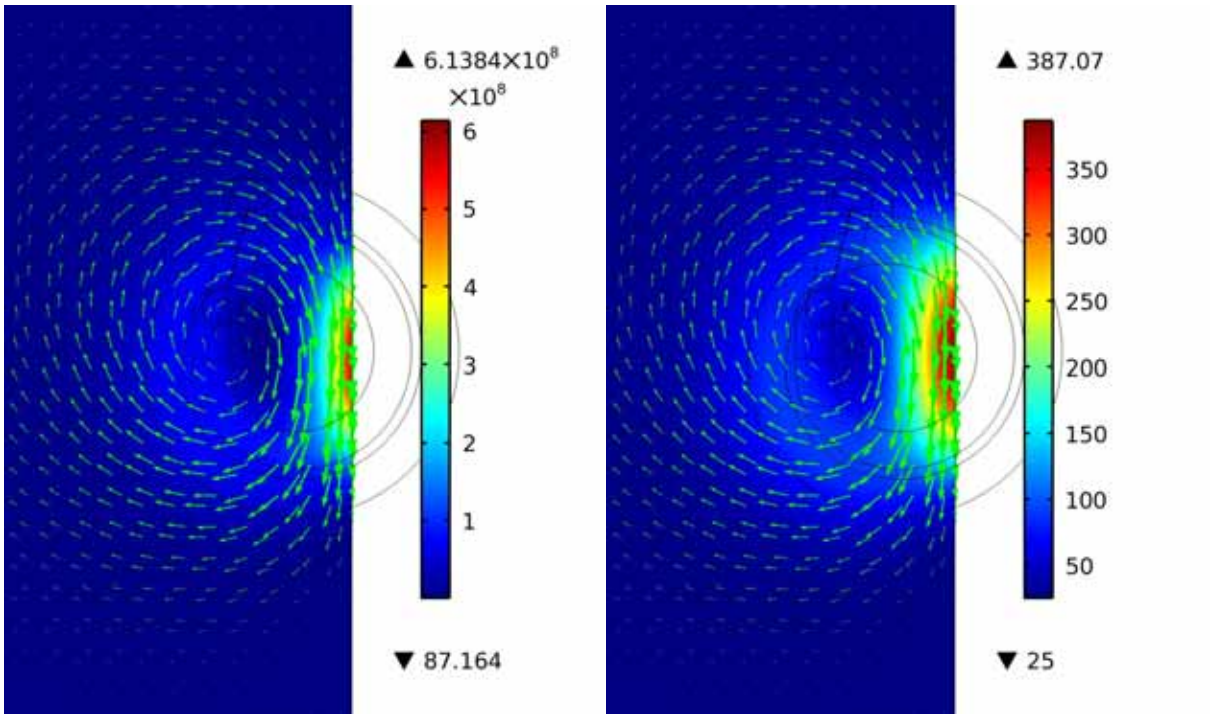

Figure 52: Power dissipation (W/m^3) (left), temperature (°C) (right) and current density (arrows) on inductor side, 8.5 mm displacement, 2 mm coupling distance, 30 % generator power, 1 s heating time

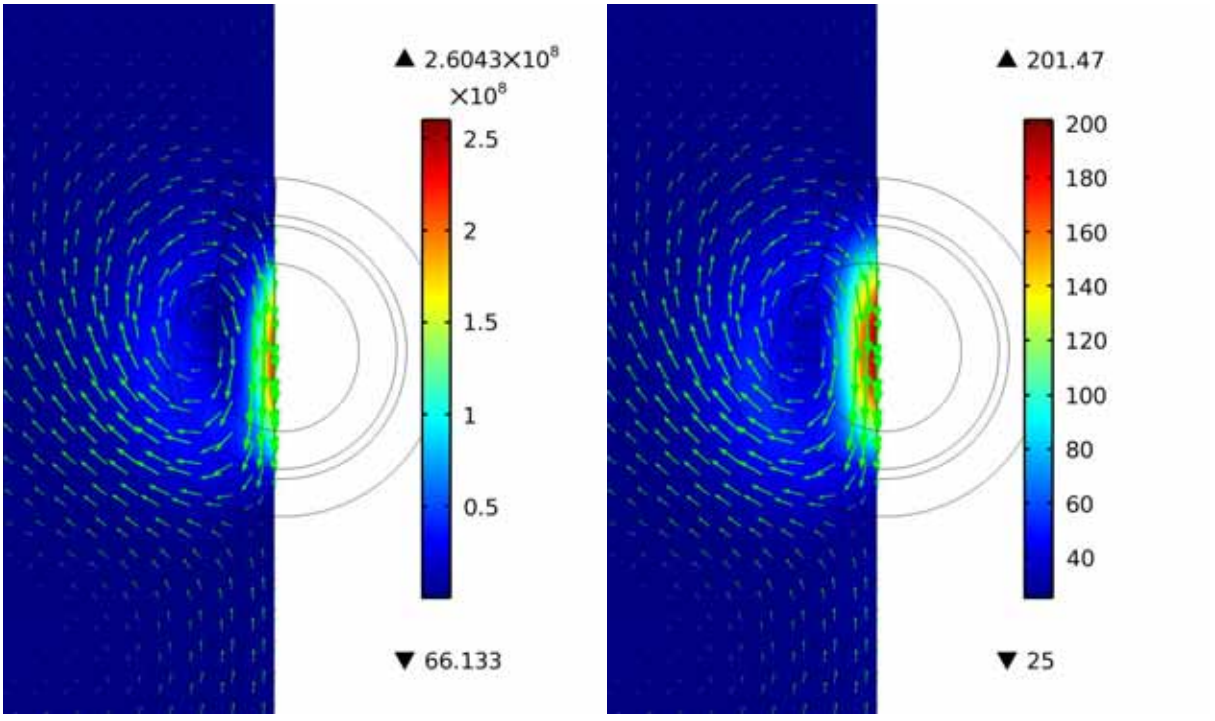

Figure 53: Power dissipation (W/m^3) (left), temperature (°C) (right) and current density (arrows) on inductor side, 13.5 mm displacement, 2 mm coupling distance, 30 % generator power, 1 s heating time

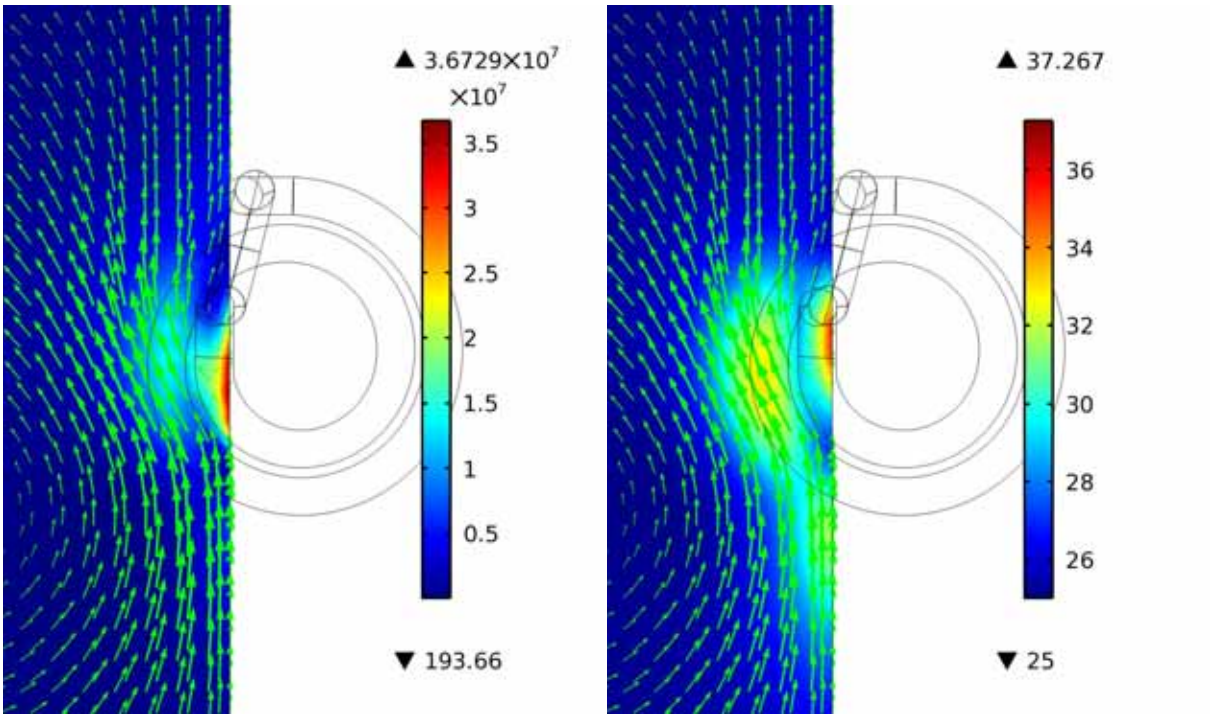

Figure 54: Power dissipation (W/m^3) (left), temperature (°C) (right) and current density (arrows) on inductor side, 18.5 mm displacement, 2 mm coupling distance, 30 % generator power, 1 s heating time

5.9. Single Sheet Induction Heating Model with Localized Surface Cooling

The induction heating model with localized surface cooling uses the approach presented in Chapter 2.6.2. The cooling effect due to the impinging jet is accounted for by a circular area with a convection coefficient calculated according to the nozzle type, the standoff distance, and the volume flow, see Chapter 5.9.2.

5.9.1. Geometry

The geometry is based on the single sheet induction heating model, see Chapter 5.5.1, with the addition of a circular element of 80 mm diameter, representing the area the convective cooling boundary is attributed to, see Figure 55.

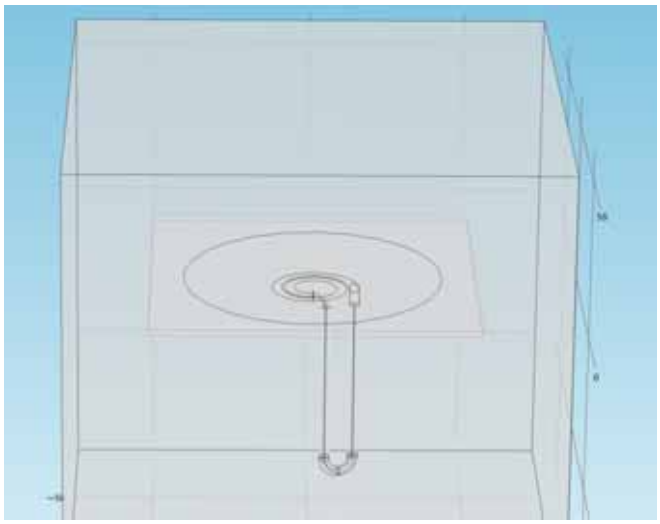

Figure 55: Geometry of single sheet model with impinging jet

5.9.2. Material Properties and Boundary Conditions

The materials used in the model are identical with the single sheet induction heating model, see Chapter 5.5.2. The boundary conditions are also based on the previous model. The only difference is a twofold convective boundary condition on the upside of the laminate, i. e. below to the coil. There, the inside of the circle is attributed the heat transfer coefficient for the impinging jet, see Table 23, whereas the outside is attributed the heat transfer coefficient for ambient conditions, see Table 22.

5.9.3. Mesh

The composite sheet was meshed using free quadratic elements with 4 elements in the thickness direction. Identical to the single sheet induction heating model, the surface of the composite sheet was converted to triangular elements in order to maintain compatibility to the tetrahedral mesh of the air domain. The mesh of the induction coil as well as the discretization of magnetic vector potential and temperature is identical to the previous model. Figure 56 shows the mesh of the induction heating model with the impinging air jet.

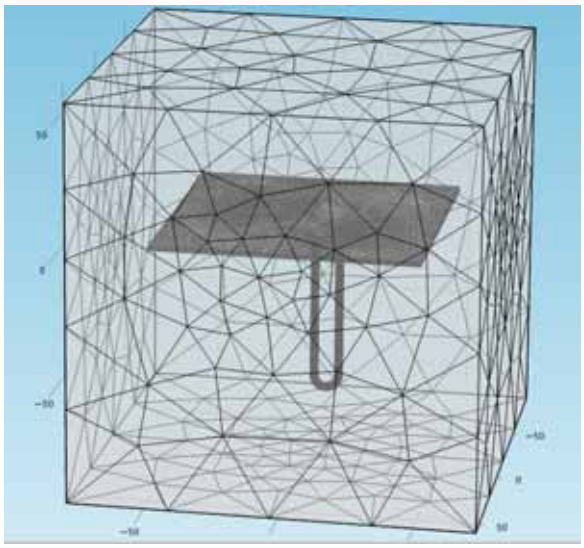

Figure 56: Mesh of single sheet model with impinging jet

5.9.4. Validation

For validation of the model the parameters used for experimental characterization were used as input parameters. Point temperature readings identical to the induction heating experiments, see Figure 15, are used for evaluation of the accuracy of the model.

Figure 57 to Figure 59 show the comparison between experimental and simulation results of the 2 mm coupling distance, 30 % generator power, and air volume flows of 304 l/min, 240 l/min, and 167 l/min for CF/PEEK. The graphs for CF/PPS are given in Figure 82 to Figure 84 in the Appendix.

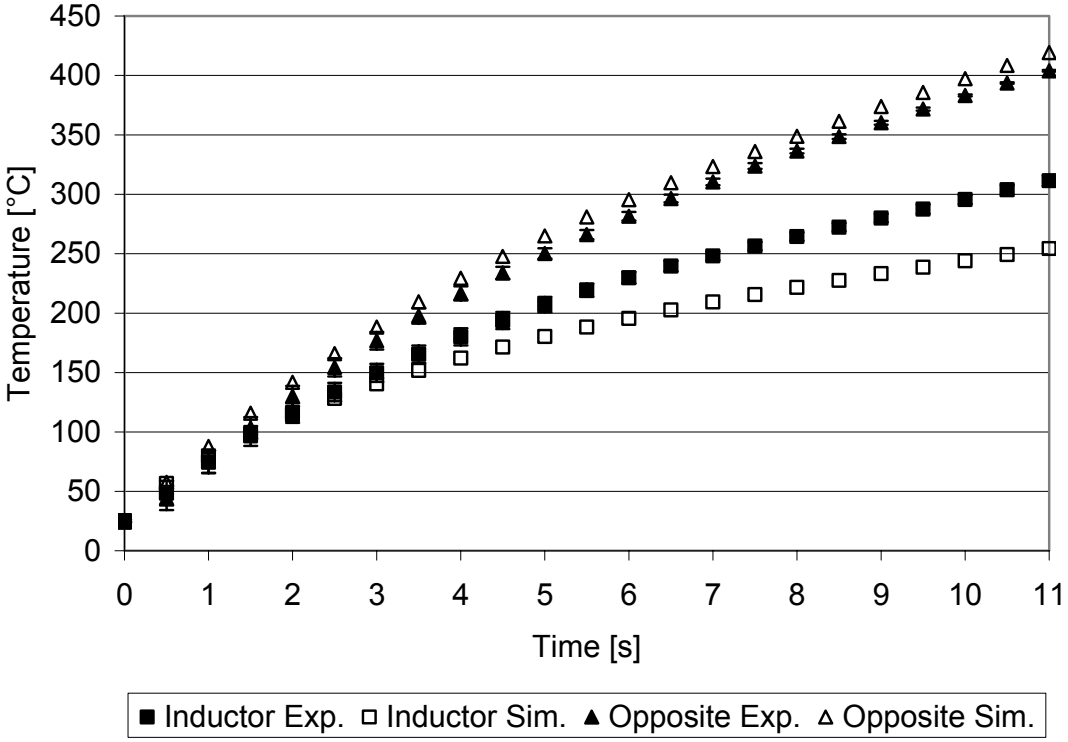

Figure 57: Validation of induction heating simulation with impinging jet, CF/PEEK, 2 mm coupling distance, 30 % generator power, 304 l/min air volume flow

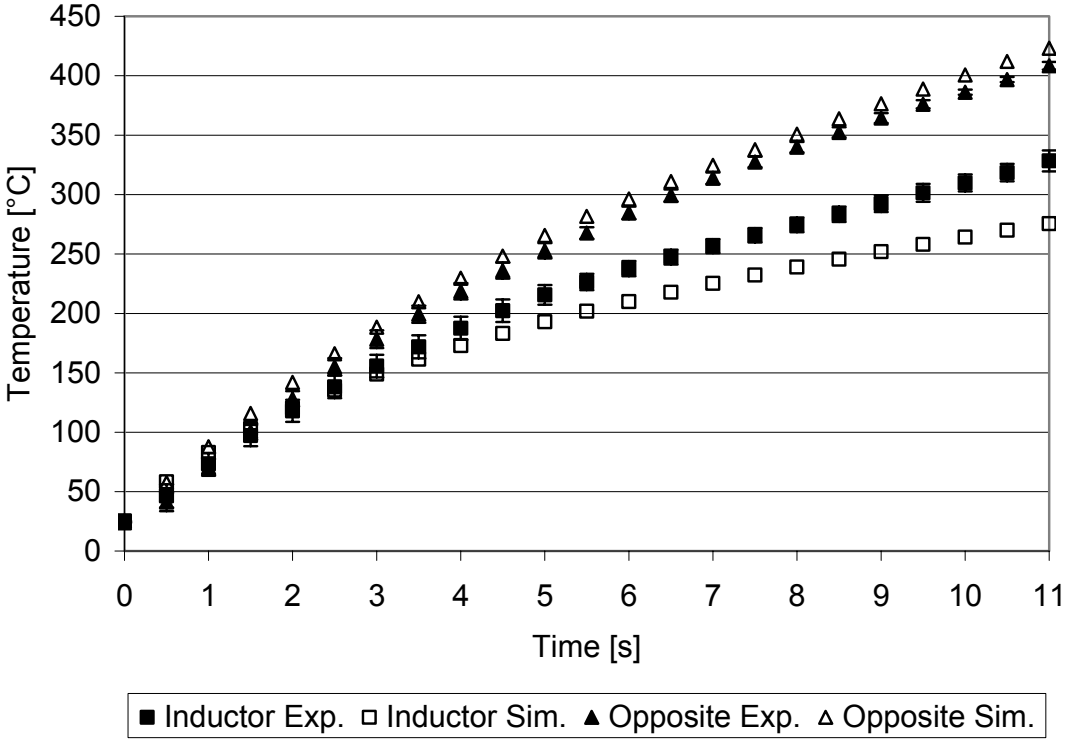

Figure 58: Validation of induction heating simulation with impinging jet, CF/PEEK, 2 mm coupling distance, 30 % generator power, 240 l/min air volume flow

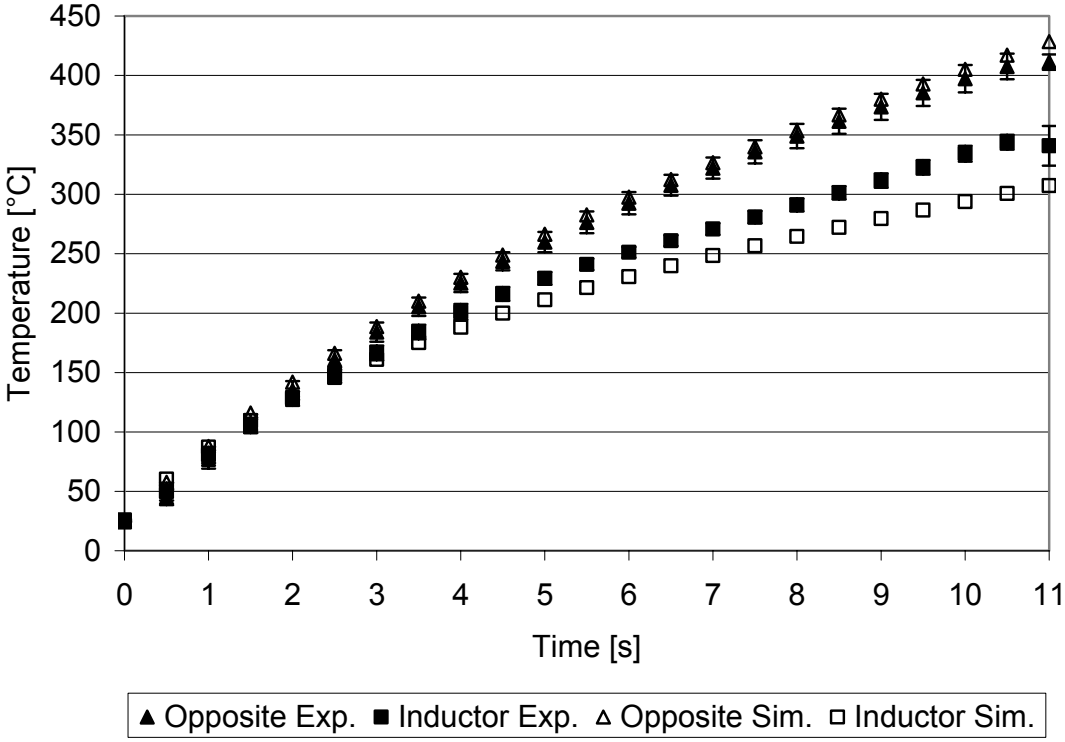

Figure 59: Validation of induction heating simulation with impinging jet, CF/PEEK, 2 mm coupling distance, 30 % generator power, 167 l/min air volume flow

In case of CF/PEEK, the opposite side is modeled very accurately with a maximum deviation of 4 % whereas the inductor side shows a maximum deviation of -18 %. For CF/PPS the inductor side temperature curve is closer to the experiment with a maximum deviation of 12 % compared to the opposite sides with a maximum of 18 %. Table 28 summarizes the deviation of the induction heating model with impinging jet.

Table 28: Temperature deviation between experimental and simulation single sheet heating, 2 mm coupling distance and 30 % generator power

Air volume flow [l/min]	CF/PEEK		CF/PPS	
	Inductor	Opposite	Inductor	Opposite
	ΔT [%]	ΔT [%]	ΔT [%]	ΔT [%]
304	-18	4	-5	16
240	-16	4	2	18
167	-10	4	12	18

6. Continuous Induction Welding Process with Localized Surface Cooling

Induction welding is a complex process involving numerous input and processing parameters, making experimental optimization studies cumbersome, time-consuming and expensive. Therefore, the modeling technique outlined in Chapter 5 was used for the development of the heating step of a novel continuous induction welding process with localized surface cooling. A parameter set suitable for welding was defined and experimentally verified. The intention was to give a proof of concept; thus the process was not optimized. The parameter set was used for induction welding of CF/PEEK overlap joints which were characterized by lap shear testing, fracture surface and cross-sectional analysis.

6.1. Geometry

Similar to the single sheet models, see Chapter 5.5 and Chapter 5.9, the continuous induction heating model consists of an induction coil, two laminates in an overlap configuration, surrounded by an airbox of 250 mm length, 250 mm width, and 150 mm height. The dimensions of the two laminates are 150 mm length, 100 mm width, and 1.95 mm thickness. Due to the strong influence of the edge effect on the power dissipation in the laminate, the overlap of the laminates to be welded was set to 32 mm.

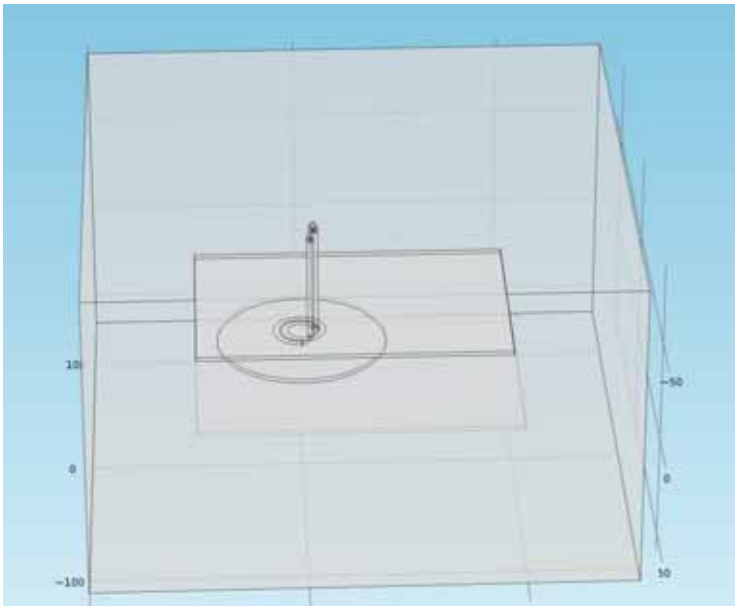

Figure 60: Geometry of the continuous induction heating model

Identical to the previous models, a volume model of the induction coil is used and the heating head of the generator is not modeled; see Figure 33 for the geometry of the

coil. A circular element of 80 mm diameter represents the area the convective cooling boundary is attributed to.

6.2. Material Properties and Boundary Conditions

The material properties for the CF/PEEK material used in the model are identical to the single sheet induction heating model, see Chapter 5.5.2. Similarly, the boundary conditions are based on the previous models; see Chapter 5.5.2 for the general and Chapter 5.9.2 for the impinging jet boundary conditions. Continuous movement of 0.088 m/min is attributed to the two laminates (see Equation (18) for the implementation in the heating model). To take into account the importance of the field frequency as analyzed in the sensitivity study, the generator operating frequency was experimentally determined using the welding setup. A value of 497 kHz was read out from the generator and used as an input parameter for the simulation.

6.3. Mesh

The two overlapping laminates are meshed using three tretrahedal elements in the thickness direction. The mesh of the induction coil and the airbox as well as the discretization of magnetic vector potential and temperature is identical to the previous models. The mesh of the continuous heating model is given in Figure 61.

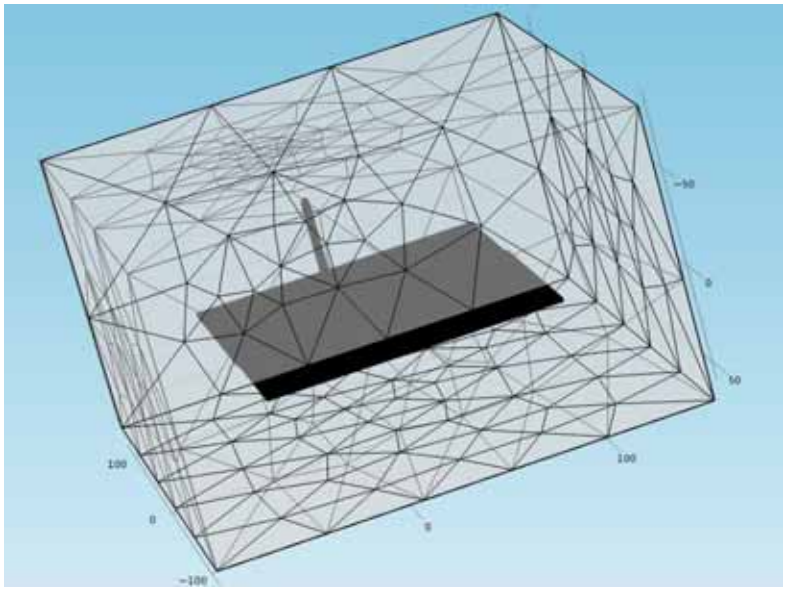

Figure 61: Mesh of continuous induction welding heating model

6.4. Parameter set

The model described above was used to determine a suitable processing parameter set. Based on the previous static heating experiments the coupling distance of 2 mm and the air volume flow of 304 l/min were used as fixed parameters whereas the generator power and the feed velocity were altered in order to yield a suitable temperature field, resulting in a parameter set consiting of 12 % generator power and 0.088 m/min feed velocity. Figure 62 shows the temperature pattern in the bondline between the two laminates using this parameter combination (2 mm coupling distance, 12 % generator power, 0.088 m/min feed velocity, and 304 l/min air volume flow). It can be seen that the temperature field behind the coil is well within the processing window and enables consolidation of the bond by a roller following the coil.

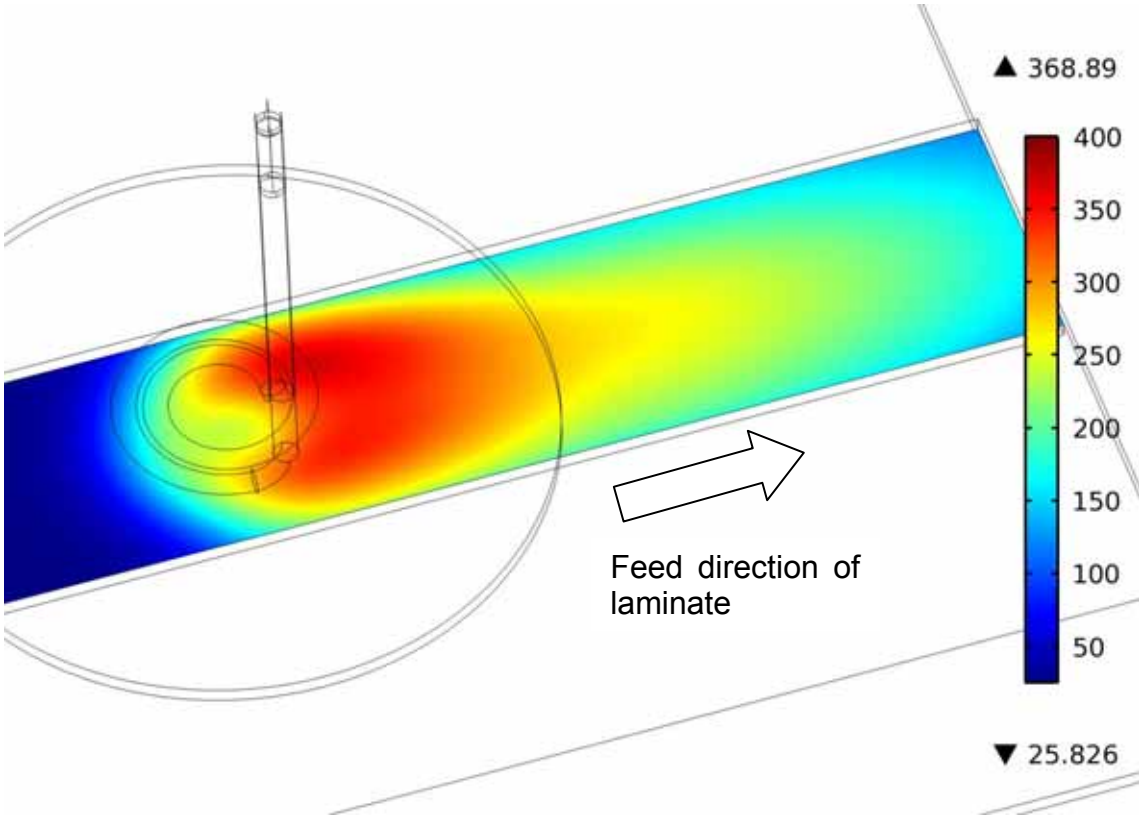

Figure 62: Calculated bondline temperature profile (°C) in the bondline of continuous welding with an impinging jet, CF/PEEK, 2 mm coupling distance, 12 % generator power, 0.088 m/min feed velocity, 304 l/min air volume flow

The related surface temperature is given in Figure 63. The calculated surface temperature is considerably lower than the melting temperature of the PEEK matrix, avoiding the defects discussed in Chapter 2.4. The surface outside the impinging jet can be seen to heat up due to the internal heat that surfaces from the bondline.

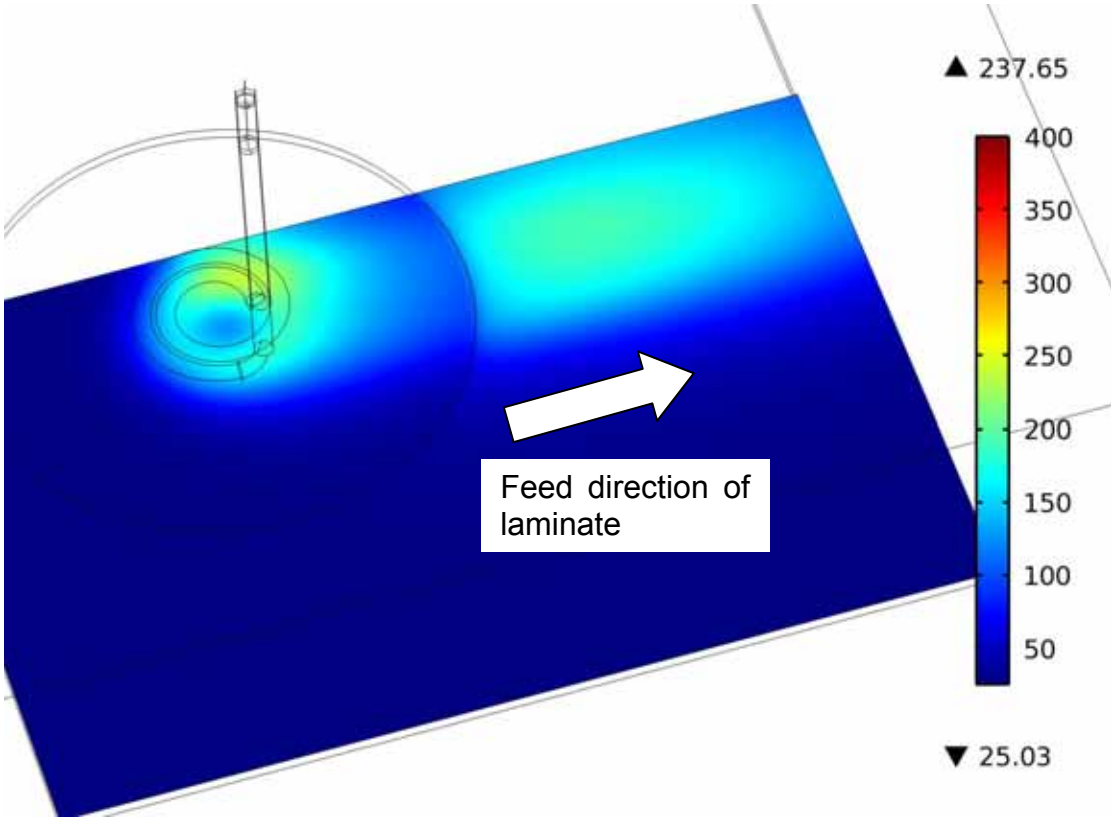

Figure 63: Calculated top surface temperature profile (°C) in the bondline of continuous welding with impinging jet, CF/PEEK, 2 mm coupling distance, 12 % generator power, 0.088 m/min feed velocity, 304 l/min air volume flow

6.5. Validation

For experimental validation of the modeling results the IVW induction welding machine was used, see Figure 64. It consists of a static induction coil holder, a fixed consolidation roller and linear guide carrying the welding fixture or tool, respectively. Continuous welding is realized by relative movement of the welding tool, see Figure 7 for a schematic and [35] for a detailed description. The other equipment such as generator, induction coil, and thermal camera were identical to the previous experiments. The pneumatic tube was positioned above the center of the coil, identical to the static heating experiments with impinging air jet, see Chapter 5.9.

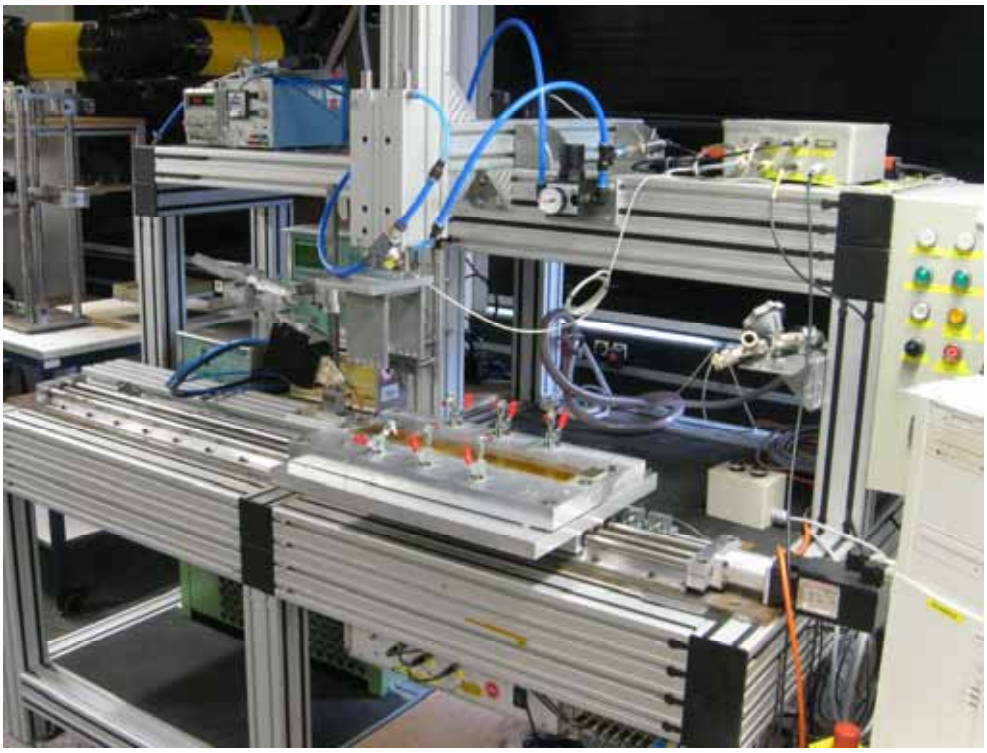

Figure 64: IVW induction welding machine

The consolidation roller consisted of a single aluminum roller with a diameter of 20 mm; the consolidation force was set to 250 N, which is comparable to the consolidation force used in other studies [105]. The roller frame was aligned with the rear edge of the coil in order to have the minimum distance between the coil and the contact line of the roller. An overview of the setup is shown in Figure 65.

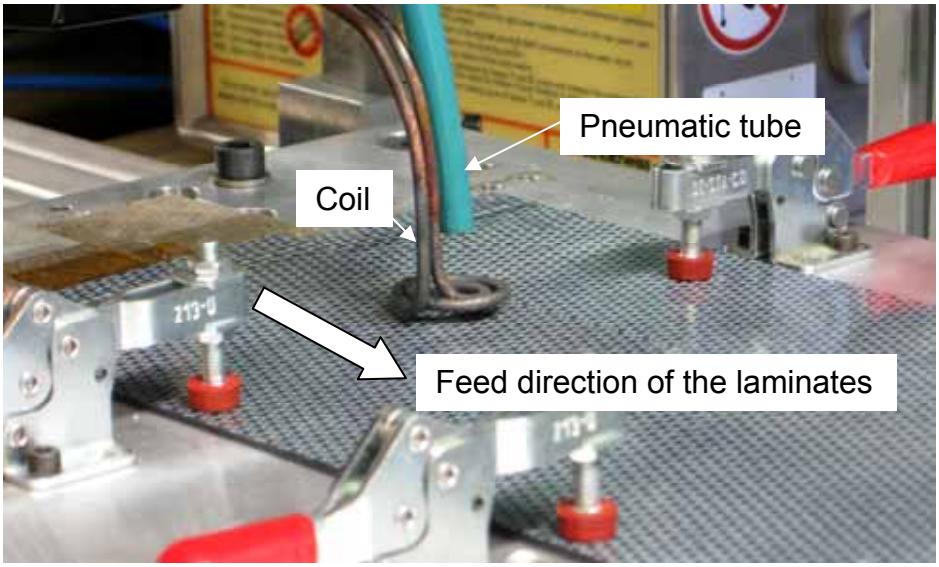

Figure 65: Continuous welding with surface cooling using an impinging jet, CF/PEEK, 2 mm coupling distance, 12 % generator power, 0.088 m/min feed velocity, 304 l/min air volume flow

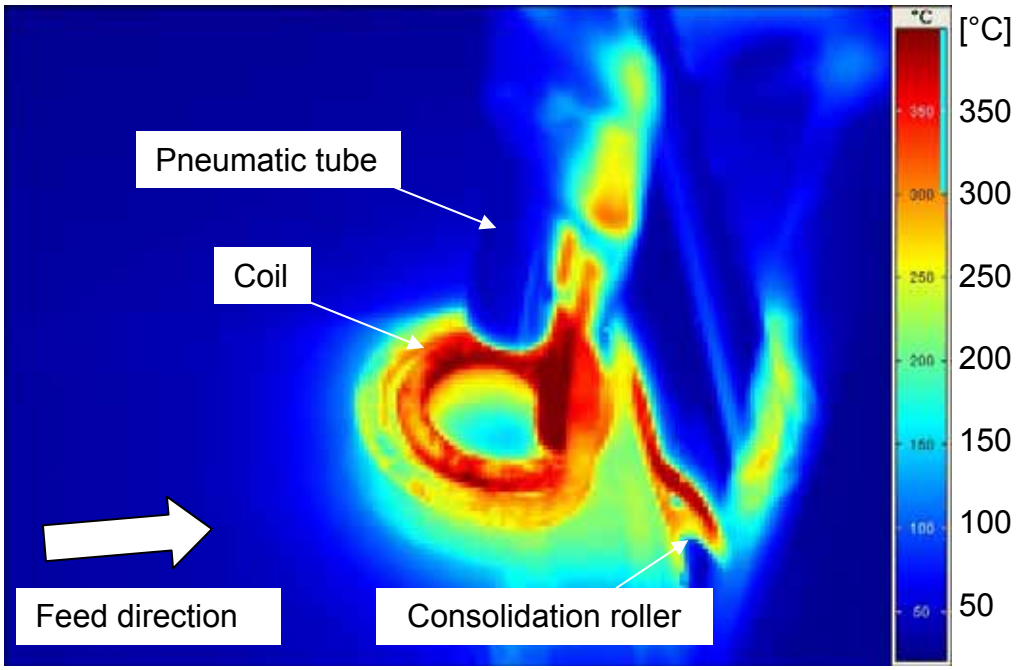

Figure 66: Measured surface temperature pattern (°C) of continuous welding with an impinging jet, CF/PEEK, 2 mm coupling distance, 12 % generator power, 0.088 m/min feed velocity, 304 l/min air volume flow

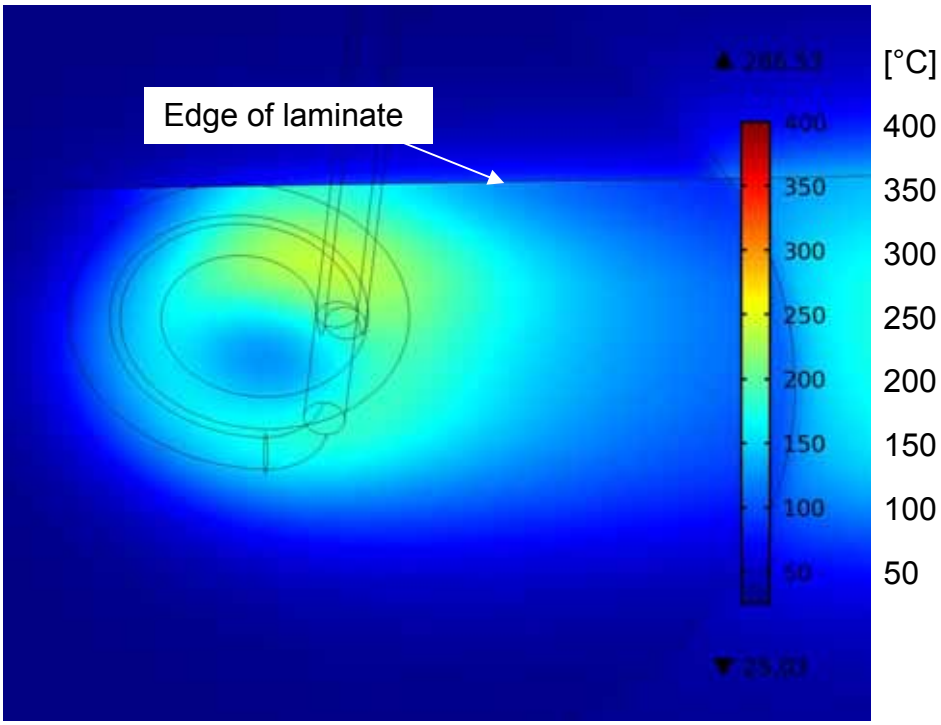

Figure 67: Calculated surface temperature pattern (°C) of continuous welding with an impinging jet, CF/PEEK, 2 mm coupling distance, 12 % generator power, 0.088 m/min feed velocity, 304 l/min air volume flow

Figure 66 and Figure 67 show a thermal image of the welding process and the related calculated temperature pattern, respectively. In the experimental thermal image, the coil and the consolidation roller are included. The induction coil is significantly heated by the carried current (liquid cooling is necessary to prevent desoldering). The consolidation roller is not directly heated but reflects the radiation of the coil and the laminate that leads to the apparent high temperature. In the simulation, neither the coil nor the roller are represented in the thermal model; therefore these objects with high temperature are not included in the image, see Figure 67.

The patterns show good correlation, with the modeling results having slightly lower temperatures. For a quantitative comparison, two point measurements were taken from the thermal images and the model solution, respectively. The measurement locations are indicated in Figure 68. Point P1 is at the cold spot in the center of the coil; point P2 is located in between the coil and the consolidation roller. The results are given in Table 29.

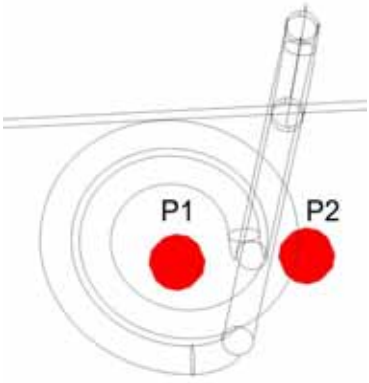

Figure 68: Point measurement locations for the validation of the continuous induction welding model

Table 29: Comparison of point measurements of the continuous model

Point	Model	Experiment	Temperature deviation	
	Temperature [°C]		[°C]	[%]
P1	129	154	-25	-16
P2	189	221	-30	-14

The deviation of the continuous process model is 16 % for the cold spot in the center and 14 % for the measurement behind the coil, which is consistent with the determined accuracy of the static heating models, see Chapter 5.

6.6. Mechanical Characterization

The induction welding machine equipped with the setup and the parameters described above was used for manufacturing of single overlap specimens from CF/PEEK laminates. In order to maintain comparability of the lap shear test results to other studies using the DIN EN 1465 sample geometry with 12.5 mm overlap, the fusion bonding area was decreased by masking 19.5 mm of the overlap length with temperature resistant tape prior to welding. The resulting geometry is shown in Figure 69.

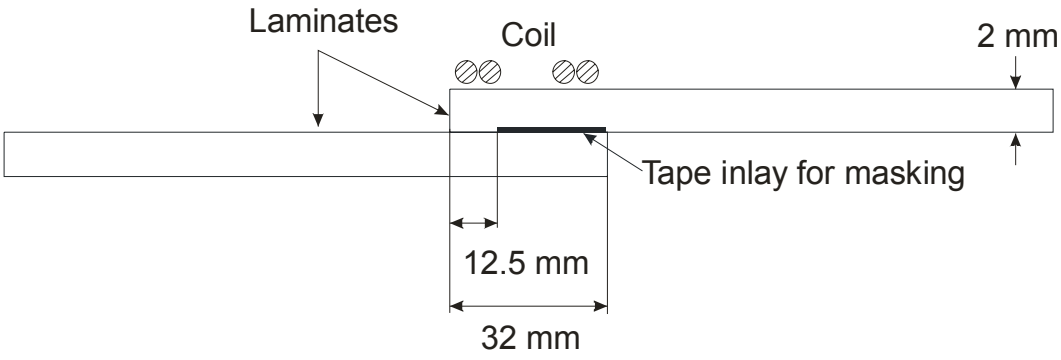

Figure 69: Geometry of single overlap specimens for tensile tests (width 25 mm)

Tensile shear testing according to DIN EN 1465 using the altered overlap were performed on a Zwick 1465 universal testing machine. Hydraulic jaws with adjustable offset were used for the alignment of the samples. Six samples were tested and the maximum tensile shear strength was calculated according to Equation (59)

$$\tau_{\max} = \frac{F_{\max}}{A_w} \tag{59}$$

where τ_{max} is maximum tensile shear strength, F_{max} is force at failure, and A_w is the non-masked overlap weld area. The results are summarized in Table 30.

Table 30: Results of shear tensile tests of CF/PEEK

Specimen	τ_{max} [MPa]
1	33.6
2	31.0
3	33.4
4	34.4
5	34.5
6	34.3
Mean value and standard deviation	33.5±1.3

The mean lap shear strength is 33.5±1.3 MPa and is within the range reported in other studies, which is between 27 MPa and 48 MPa [25].The low scatter of 4 % is an indicator for sufficient process stability and reproducibility.

Figure 70 shows the fracture surface of Specimen 6. The area masked by the adhesive tape shows no signs of bonding. The non-masked area is characterized by the absence of non-bonded areas and cohesive failure.

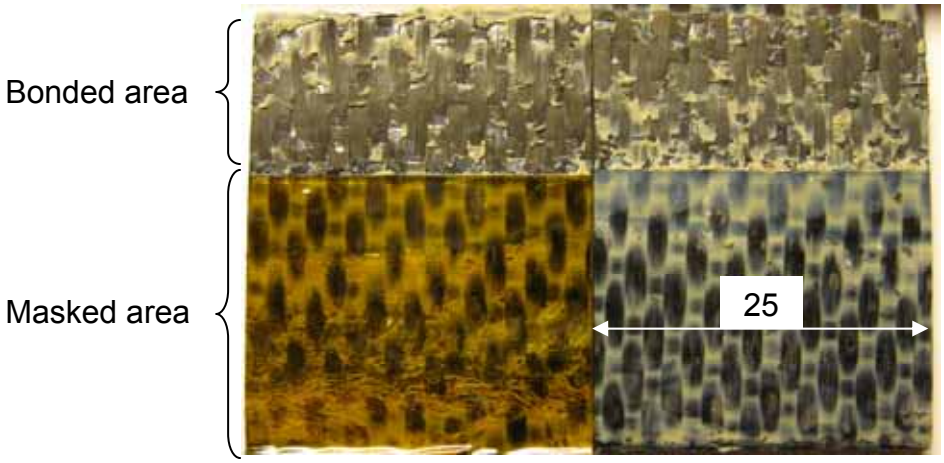

Figure 70: Fracture surfaces of CF/PEEK lap shear test sample, 2 mm coupling distance, 12 % generator power, 0.088 m/min feed velocity, 304 l/min air volume flow

Cross-sectional inspection of the weld, see Figure 71, shows a low void content in the welded joint.

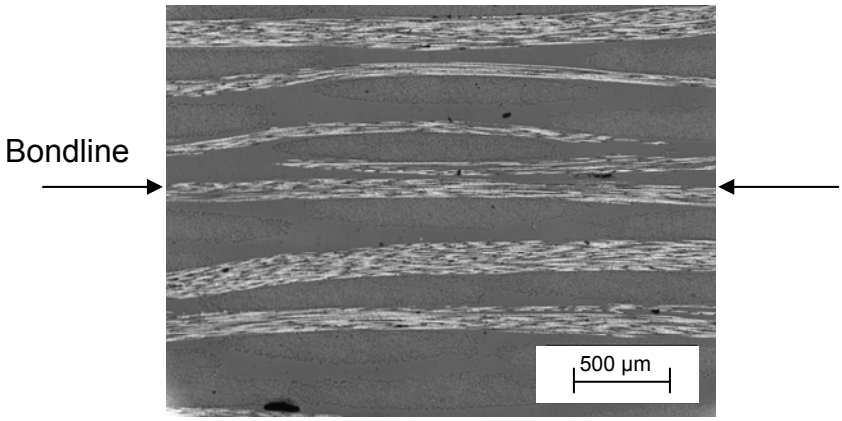

Figure 71: Cross-section of CF/PEEK lap shear test sample

The lap shear strength as well as the fracture surface and the cross-sectional analysis of the sample show that the processing parameters determined by the processing model yielded a suitable parameter set.

Figure 72 gives a comparison of two samples welded without and with localized surface cooling, respectively. It can be seen that the sample welded without surface cooling shows unwanted material transitions on the top surface whereas the sample that was welded with cooling by an impinging air jet shows no signs of undesired temperature effects.

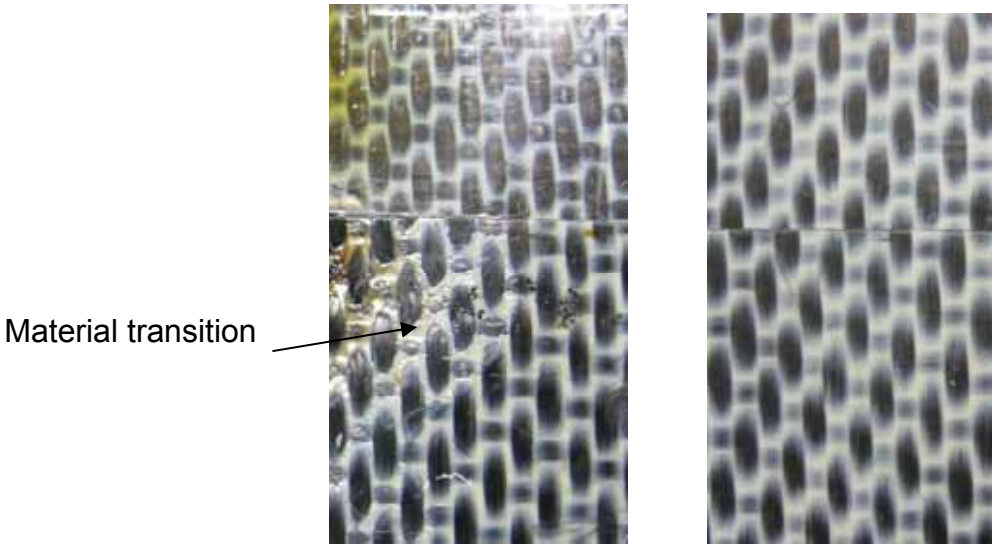

Figure 72: Comparison of CF/PEEK specimen without localized surface cooling (left) and surface cooling with impinging air jet, 2 mm coupling distance, 12 % generator power, 0.088 m/min feed velocity, 304 l/min air volume flow (right)

7. Summary

The susceptorless induction heating process of high performance thermoplastic polymer composites was analyzed in this study and a novel processing technique as well as a suitable modeling approach were introduced.

In the experimental part, induction heating of continuously reinforced CF/PEEK and CF/PPS laminates with a single pancake coil was characterized. The temperature field was found to be highly localized and anisotropic both through-the-thickness and in-plane. The upper side of a laminate in the vicinity of the induction coil is subject to significantly higher temperature compared to the lower side which will form the bondline in an overlap joint. The temperature gradients between the surface facing the inductor and the opposite side depend on the processing parameters such as coupling distance, generator power and the matrix material. Values up to 104 K in case of CF/PEEK and 89 K in case of CF/PEEK were measured. Taking into account the processing window that theoretically spans between the melting temperature of the matrix and the degradation temperature (in practice a welding temperature of 50 K above the melting temperature is recommended), welding may be difficult. For the materials used in this study, the processing windows were calculated to 50 K - 100 K (different values for the degradation temperature are reported in the open literature) in case of CF/PEEK and 40 K in case of CF/PPS.

In order to avoid unwanted heating of the surface close to the induction coil a novel process variant was developed utilizing localized surface cooling by an impinging air jet. This enables the surface temperature on the inductor side of the laminate to remain well below the melting temperature whereas the opposite side can be heated to the necessary welding temperature. Thus, the bondline in an overlap configuration can be melted while delamination effects on the top surface are prevented. The temperature difference between the inductor (lower temperature) and the opposite side (higher temperature) is dependent on the volume flow of the impinging jet and could be established up to 99 K in case of CF/PEEK and 85 K in case of CF/PPS.

Because of the complexity of the induction heating, process development is complex. Systematic studies that are necessary for determining the effect of processing parameters are time consuming and expensive. Process modeling can be a useful tool since it allows the determination of parameters that cannot be directly measured,

such as the bondline temperature. Furthermore, the significance of processing parameters can be evaluated in a fast and cost efficient way.

A three-dimensional fully coupled electromagnetic/thermal finite element model of static induction heating using the commercial FEM code Comsol Multiphysics was developed. The accuracy of the model is good with deviations mostly in the range between 10 % and 20 %. A sensitivity analysis of the processing and input parameters was performed. The most significant parameters were the coil current and the field frequency, followed by the heat capacity. The enhanced processing technique with localized surface cooling by using an impinging air jet was implemented in the model. The chosen approach of locally increased heat transfer coefficients yielded good accuracy with deviations below 20 % which is in the range of the base model.

Based on the previous models, a model of the continuous process with two laminates in an overlap configuration utilizing localized surface cooling by the impinging air jet was developed. It was applied for the determination of a parameter set for continuous welding of CF/PEEK laminates and used for manufacturing of lap shear strength specimens, which yielded a mean lap shear strength of 33.5 MPa and avoided unwanted heating on the surface in the vicinity of the induction coil. The measured lap shear strength as well as the fracture surface inspection and the cross-sectional analysis indicated that a weld of good quality could be manufactured. However, taking into account that the parameters were not optimized, further improvements in weld quality can be expected.

The developed induction heating technique opens up the possibility of continuous induction welding without thermally induced damage and eliminates the need for sophisticated tooling. Possible applications include the manufacturing of complex aerospace components or automotive parts.

8. References

1. Hull, D.; Clyne, T. W.: An Introduction to Composite Materials. Cambridge: Cambridge University Press, 1996.
2. Beral, B.: Airbus Composite Innovation - Current and Future Perspectives; in: SAMPE Europe 1st Symposium on Automation in Composite Technology, Munich, June 9-10, 2010, 196-210.
3. Räckers, B.: Verbundwerkstoffe im Airbus A380; in Kunststoffe im Automobilbau 2006, Mannheim, March 29-30, 2006, 397-400.
4. Räckers, B.: Entwicklung und Perspektiven von CFK-Einsatz in modernen Luftfahrzeugen; in: IVW-Kolloquium 2008, Kaiserslautern, September 16-17, 2008, 3-8.
5. Breuer, U. P.: Herausforderungen an die CFK-Forschung aus Sicht der Verkehrsflugzeug-Entwicklung und -fertigung; in: 10. Nationales Symposium SAMPE Deutschland e. V., Darmstadt, March 3-4, 2005, 1-11.
6. Offringa, A. R.: Thermoplastic Composites – Rapid Processing Applications. Composites Part A: Applied Science and Manufacturing 27 (1996), Issue 4, 329-336.
7. Neitzel, M.; Mitschang, P: Handbuch Verbundwerkstoffe. Munich: Hanser, 2004.
8. Harper, C. A.: Handbook of Plastics, Elastomers, and Composites. New York: McGraw-Hill, 2002.
9. Hou, M.; Ye, L.; Mai, Y.-W.: An Experimental Study of Resistance Welding of Carbon Fibre Fabric Reinforced Polyetherimide (CF Fabric/PEI) Composite Material. Applied Composite Materials 6 (1999), Issue 1, 35-49.
10. Colak, Z. S.; Sonmez, F. O.; Kalenderoglu, V.: Process Modeling and Optimization of Resistance Welding for Thermoplastic Composites. Journal of Composite Materials 36 (2002), Issue 6, 721-744.
11. Gutowski, T. G.: Advanced Composites Manufacturing. New York: Wiley, 1997.
12. Bersee, H. E. N.: Diaphragm Forming of Continuous Fibre Reinforced Thermoplastics – Process Analysis and Development. TU Delft: Faculty of Aerospace Engineering, 1996.

13. Schwartz, Mel M.: Joining of Composite Matrix Materials. Materials Park: ASM International, 1994.

14. Ageorges, C.; Ye, L.: Resistance Welding of Metal/Thermoplastic Composite Joints. Journal of Thermoplastic Composite Materials 14 (2001), Issue 6, 449-475.

15. Ageorges, C.; Ye, L.: Fusion Bonding of Polymer Composites. London – Berlin – Heidelberg: Springer, 2002.

16. Todd, S. M.: Joining Thermoplastic Composites; in: 22nd International SAMPE Technical Conference, Boston, November 6-8, 1990, 383-392.

17. Ageorges, C.; Ye, L.; Hou, M.: Advances in Fusion Bonding Techniques for Joining Thermoplastic Matrix Composites: A Review. Composites Part A: Applied Science and Manufacturing 32 (2001), Issue 6, 839-857.

18. Silverman, E.; Griese, R.: Joining Methods for Graphite/PEEK Thermoplastic Composites. SAMPE Journal 25 (1989), Issue 5, 34-38.

19. Eveno, E. C.; Gillespie, J. W., Jr.: Resistance Welding of Graphite Polyetheretherketone Composites: An Experimental Investigation. Journal of Thermoplastic Composite Materials 1 (1988), Issue 4, 322-338.

20. Maguire, D. M.: Joining Thermoplastic Composites. SAMPE Journal 25 (1989), Issue 1, 11-14.

21. Ye, L.; Chen, Z.-R.; Lu, M.; Hou, M.: De-Consolidation and Re-Consolidation in CF/PPS Thermoplastic Matrix Composites. Composites Part A: Applied Science and Manufacturing 36 (2005), Issue 7, 915-922.

22. Ageorges, C.; Lin, Y.; Mai, Y.-W.; Meng, H.: Characteristics of Resistance Welding of Lap Shear Coupons. Part I: Heat Transfer. Composites Part A: Applied Science and Manufacturing 29 (1998), Issue 8, 899-909.

23. Miller, A., K.; Chang, C.; Payne, A.; Gur, M.; Menzel, E.; Peled, A.: The Nature of Induction Heating in Graphite-Fiber, Polymer-Matrix Composite Materials. SAMPE Journal 26 (1990), 37-54.

24. Yousefpour, A.; Hojjati, M.; Immarigeon, J. P.: Fusion Bonding/Welding of Thermoplastic Composites. Journal of Thermoplastic Composite Materials 17 (2004), Issue 4, 303-341.

25. Ahmed, T.; Stavrov, D.; Bersee, H. E. N.; Beukers, A.: Induction Welding of Thermoplastic Composites – An Overview. Composites Part A: Applied Science and Manufacturing 37 (2006), Issue 10, 1638-1651.

26. Stokes, V. K.: Joining Methods for Plastics and Plastic Composites: An Overview. Polymer Engineering and Science 29 (1989), Issue 19, 1310-1324.

27. Grewell, D. A.; Benatar, A.; Park, J. B.: Plastics and Composites Welding Handbook. Munich: Hanser, 2003.

28. Benatar, A.; Gutowski, T. G.: Methods for Fusion Bonding Thermoplastic Composites. SAMPE Quarterly 18 (1986), Issue 1, 35-42.

29. Lin, W.: Induction Heating Model for High Frequency Induction Joining and Repair of Complex-Shape Graphite Fiber/Polymer Matrix Composites. Stanford University: Department of Material Science and Engineering, 1993.

30. Yarlagadda, S.; Kim, H. J.; Gillespie, J. W., Jr.; Shevchenko, N. B.; Fink, B. K.: A Study on the Induction Heating of Conductive Fiber Reinforced Composites. Journal of Composite Materials 36 (2002), Issue 4, 401-421.

31. Mitschang, P.; Rudolf, R.; Neitzel, M.: Continuous Induction Welding Process, Modelling and Realisation. Journal of Thermoplastic Composite Materials Journal of Thermoplastic Composite Materials 15 (2002), Issue 2, 127-153.

32. Moser, L.; Mitschang, P.; Schlarb, A. K.: Induction Welding of Thermoplastic Polymer Composites Using Robotic Techniques. SAMPE Journal 44 (2008), Issue 5, 43-48.

33. van Ingen, J. W.; Buitenhuis, A.; van Wijngaarden, M.; Simmons III, F.: Development of the Gulfstream G650 Induction Welded Thermoplastic Elevators and Rudder; in: SAMPE 2010 International Conference, Seattle, May 17-20, 2010.

34. Patent WO 2008/133507 A2.

35. Rudolf, R.: Entwicklung einer neuartigen Prozess- und Anlagentechnik zum wirtschaftlichen Fügen von thermoplastischen Faser-Kunststoff-Verbunden. Kaiserslautern: Institut für Verbundwerkstoffe, 2000.

36. Rudolf, R.; Mitschang, P.; Neitzel, M.: Induction Heating of Continuous Carbon-Fibre-Reinforced Thermoplastics. Composites Part A: Applied Science and Manufacturing 31 (2000), Issue 11, 1191-1202.

37. Grimm, R. A.: Fusion Welding Techniques for Plastics. Welding Journal 69 (1990), Issue 3, 23-28.

38. Mantell, S. C.; Springer, G. S.: Manufacturing Process Models for Thermoplastic Composites. Journal of Composite Materials 26 (1992), Issue 16, 2348-2377.

39. Sonmez, F. O.; Hahn, H. T.: Analysis of the On-Line Consolidation Process in Thermoplastic Composite Tape Placement. Journal of Thermoplastic Composite Materials 10 (1997), Issue 6, 543-572.

40. Xiao, X. R.; Hoa, S. V.; Street, K. N.: Processing and Modeling of Resistance Welding of APC-2 Composite. Journal of Composite Materials 26 (1992), Issue 7 (1992), 1031-1049.

41. Wool, R. P.; O'Connor, K. M.: Time Dependence of Crack Healing. Journal of Polymer Science: Polymer Letters Edition 20 (1982), Issue 1, 7-16.

42. Loos, A. C.; Dara, P. H.: Processing of Thermoplastic Matrix Composites; in: Review of Progress in Quantitative Nondestructive Evaluation, La Jolla, August 3-8, 1987, 1257-1265.

43. Lorrain, P.; Corson, D. R.: Electromagnetism: Principles and Applications. San Francisco: Freeman, 1979.

44. Orfeuil, M.: Electric Process Heating: Technologies/Equipment/Applications. Columbus: Battelle, 1987.

45. Christopoulos, C.: An Introduction to Applied Electromagnetism. Chichester: Wiley, 1990.

46. Metaxas, A. C.: Foundations of Electroheat: A Unified Approach. Chichester: Wiley, 1996.

47. Rudnev, V.; Loveless, D.; Cook, R.; Black, M: Handbook of Induction Heating. New York–Basel: Marcel Dekker, 2003.

48. Linse, H.; Fischer, R.: Elektrotechnik für Maschinenbauer. Stuttgart: Teubner, 2000.

49. Küpfmüller, K.; Bosse, G.: Einführung in die theoretische Elektrotechnik. Berlin: Springer, 1984.

50. Fink, B. K.: Heating of Continuous-Carbon-Fiber-Reinforced Thermoplastic by Magnetic Induction. University of Delaware: Center for Composite Materials, 1991.

51. Fink, B. K.; McCullough, R. L.; Gillespie, J. W., Jr.: A Local Theory of Heating in Cross-Ply Carbon Fiber Thermoplastic Composites by Magnetic Induction. Polymer Engineering & Science 32 (1992), Issue 5, 357-369.

52. Fink, B. K.; McCullough, R. L.; Gillespie, J. W., Jr.: A Model to Predict the Through-Thickness Distribution of Heat Generation in Cross-Ply Carbon-Fiber Composites Subjected to Alternating Magnetic Fields. Composites Science and Technology 55 (1995), Issue 2, 119-130.

53. Border, J.; Salas, R.: Induction Heated Joining of Thermoplastic Composites Without Metal Susceptors; in: 34th International SAMPE Symposium, Reno, May 8-11, 1989, 2569-2578.

54. Nichols, R. J.: Advances in the Emabond Induction Welding Process for High Performance Assembly of Demanding Thermoplastics; in: 24th Annual Assembly Technical Expo, Rosemont, September 23-25, 2003, 1-10.

55. Kagan, V. A.; Nichols, R. J.: Recent Advances and Challenges in Induction Welding of Reinforced Nylon in Automotive Applications; in: SAE World Congress, Detroit, March 8-11, 2004.

56. Nichols, R. J.; LaMarca, D. P.; Agosto, B.: Performance of Susceptor Materials in High Frequency Magnetic Fields; in: ANTEC 2006, Charlotte, May 7-11, 2006.

57. Suwanwatana, W.; Yarlagadda, S.; Gillespie, J. W., Jr.: Influence of Particle Size on Hysteresis Heating Behavior of Nickel Particulate Polymer Films. Composites Science and Technology 66 (2006), Issue 15, 2825-2836.

58. Suwanwatana, W.; Yarlagadda, S.; Gillespie, J. W., Jr.: Hysteresis Heating Based Induction Bonding of Thermoplastic Composites. Composites Science and Technology 66 (2006), Issue 11-12, 1713-1723.

59. Hodges, W. T.; Tyeryar, J. R.; Berry, M.: Bonding and Nondestructive Evaluation of Graphite/PEEK Composite and Titanium Adherends with Thermoplastic

Adhesives; in: Society of Manufacturing Engineers Conference on Fabricating Composites, Hartford, June 11-13, 1985, MF85-511-MF85-511-13.

60. Wedgewood, A. R.; Hardy, P. E.: Induction Welding of Thermoset Composite Adherends Using Thermoplastic Interlayers and Susceptors; in: 28th International SAMPE Technical Conference, Seattle, November 4-7, 1996, 850-861.

61. Williams, G.; Green, S.; McAfee, J.; Heward, C. M.: Induction Welding of Thermoplastic Composites; in: 4th International Conference on Fiber Reinforced Composites, Liverpool, March 27-29, 1990, 133-136.

62. Lin, W.; Miller, A. K.; Buneman, O.: Predictive Capabilities of an Induction Heating Model for Complex-Shape Graphite Fiber/Polymer Matrix Composites; in: 24th International SAMPE Technical Conference, Toronto, October 20-22, 1992, T606-T620.

63. Xiao, X. R.: A Model for the Deconsolidation Phenomenon in Induction Heating of Thermoplastic Resin Composites; in: 9th International Conference on Composite Materials (ICCM/9), Madrid, July 12-16, 1993, 243-250.

64. Fink, B. K.; McCullough, R. L.; Gillespie, J. W., Jr.: Experimental Verification of Models for Induction Heating of Continuous-Carbon-Fiber Composites. Polymer Composites 17 (1996), Issue 2, 198-209.

65. Lin, W.; Buneman, O.; Miller, A. K.: Induction Heating Model for Graphite Fiber/Thermoplastic Matrix Composites. SAMPE Journal 27 (1991), Issue 6, 45-51.

66. Lee, S.-E.; Park, K.-Y.; Oh, K.-S.; Kim, C.-G.: The Use of Carbon/Dielectric Fiber Woven Fabrics as Filters for Electromagnetic Radiation. Carbon 47 (2009), Issue 8, 1896-1904.

67. Kupke, M.; Schulte, K.; Schüler, R.: Non-Destructive Testing of FRP by D.C. and A.C. Electrical Methods. Composites Science and Technology 61 (2002), Issue 6, 837-847.

68. Sauder, C.; Lamon, J.; Pailler, R.: Thermomechanical Properties of Carbon Fibres at High Temperatures (up to 2000 °C). Composites Science and Technology 62 (2002), Issue 4, 499-504.

69. Wen, S.; Wang, S.; Chung, D. D. L.: Carbon Fiber Structural Composites as Thermistors. Sensors and Actuators A: Physical 78 (1999), Issue 2-3, 180-188.

70. Zinn, S.; Semiatin, S. L.: Coil Design and Fabrication: Basic Design and Modifications. Heat Treating (1988), Issue June 32-41.

71. Miller, A. K.; Gur, M.; Peled, A.; Payne, A.; Menzel, E.: Die-Less Forming of Thermoplastic- Matrix, Continuous-Fiber Composites. Journal of Composite Materials 24 (1990), Issue 4, 346-381.

72. Beyler, C; Hirschler, M: Thermal Decomposition of Polymers; in: DiNenno, P. J. (Ed.): SFPE Handbook of Fire Protection Engineering. Quincy – Bethesda: National Fire Protection Association, Society of Fire Protection Engineers, 2002, 110-131.

73. Standard ASTM E 176.

74. Menges, G; Haberstroh, E.; Michaeli, W.; Schmachtenbergs, E.: Werkstoffkunde Kunststoffe. Studientexte Kunststofftechnik. München – Wien: Hanser, 2002.

75. Talbot, E.; Yousefpour, A.; Hubert, P.; Hojjati, M.: Thermal Behavior During Thermoplastic Composites Resistance Welding; in: ANTEC 2005, Boston, May 1-5, 2005.

76. Ten Cate Advanced Composites: Safety Data Sheet Carbon - PPS Doc. 4050.007, (2007).

77. Cogswell, F. N.: Thermoplastic Aromatic Polymer Composites: A Study of the Structure, Processing, and Properties of Carbon Fibre Reinforced Polyetheretherketone and Related Materials. Oxford: Butterworth-Heinemann, 1992.

78. Atreya, A.; Agrawal, S.: An Experimental and Theoretical Investigation Into Burning Charcteristics of PPS-Glass Fiber Composites; in: 8th AIAA/ASME Joint Thermophysics and Heat Transfer Conference, St. Louis, June 24-26, 2002.

79. Ye, L.; Lu, M.; Mai, Y.-W.: Thermal De-Consolidation of Thermoplastic Matrix Composites – I. Growth of Voids. Composites Science and Technology 62 (2002), Issue 16, 2121-2130.

80. Rudolf, R.; Mitschang, P.; Neitzel, M.; Rückert, C.: Welding of High-Performance Thermoplastic Composites. Polymer & Polymer Composites 7 (1999), Issue 5, 309-315.

81. van Wijngaarden, M. J.: Robotic Induction Welding of Carbon Fiber Reinforced Thermoplastics; in: SAMPE 2005 Fall Technical Conference, Seattle, October 31 - November 3, 2005.

82. Bay, F.; Labbe, V.; Favennec, Y.; Chenot, J. L.: A Numerical Model for Induction Heating Processes Coupling Electromagnetism and Thermomechanics. International Journal for Numerical Methods in Engineering 58 (2003), Issue 6, 839-867.

83. Bensaid, S.; Trichet, D.; Fouladgar, J.: 3-D Simulation of Induction Heating of Anisotropic Composite Materials. IEEE Transactions on Magnetics 41 (2005), Issue 5, 1568-1571.

84. COMSOL AB: AC/DC Module User's Guide Version 4.1, (2010).

85. Cheng, D. K.: Field and Wave Electromagnetics. Reading: Addison-Wesley, 1983.

86. COMSOL AB: COMSOL Multiphysics User's Guide Version 4.1, (2010).

87. Verein Deutscher Ingenieure (Hrsg.): VDI-Wärmeatlas. Berlin: Springer, 2006.

88. Incropera, F. P.; DeWitt, D. P.: Fundamentals of Heat and Mass Transfer. Hoboken: Wiley, 2002.

89. Lienhard, J. H. IV; Lienhard, J. H. V: A Heat Transfer Textbook. Cambridge: Phlogiston Press, 2011.

90. Gillespie, J. W., Jr.; McCullough, R. L.; Fink, B. K.: Induction Heating of Cross-ply Carbon-Fiber Composites. ANTEC 1992, Detroit, May 4-7, 1992, 2106-2109.

91. Kim, H.; Yarlagadda, S.; Gillespie, J. W., Jr.; Shevchenko, N. B.; Fink, B. K.: A Study on the Induction Heating of Carbon Fiber Reinforced Thermoplastic Composites. Advanced Composite Materials 11 (2002), Issue 1, 71-80.

92. Velthuis, R.: Induction Welding of Fiber Reinforced Thermoplastic Polymer Composites to Metals. Kaiserslautern: Institut für Verbundwerkstoffe, 2007.

93. Jakobsen, T. B.; Don, R. C.; Gillespie Jr., J. W.: Two-Dimensional Thermal Analysis of Resistance Welded Thermoplastic Composites. Polymer Engineering & Science 29 (1989), Issue 23, 1722-1729.

94. Gaier, J. R.; YoderVandenberg, Y.; Berkebile, S.; Stueben, H.; Balagadde, F.: The Electrical and Thermal Conductivity of Woven Pristine and Intercalated Graphite Fiber-Polymer Composites. Carbon 41 (2003), Issue 12, 2187-2193.

95. Ticona GmbH: Fortron Polyphenylensulfid (PPS), (2007).

96. Ensinger GmbH: TECAPEEK Material Data Sheet, (2011).

97. COMSOL AB: Material Data Base Version 4.1, (2010).

98. Kroschwitz, J. I. (Ed.): Concise Encyclopedia of Polymer Science and Engineering. New York: Wiley, 1990.

99. Carbone, R.; Langella, A.: Numerical Modeling of Resistance Welding Process in Joining of Thermoplastic Composite Materials Using Comsol Multiphysics; in: COMSOL Conference 2009, Milan, October 14-16, 2009.

100. Lu, M.; Ye, L.; Mai, Y.-W.: Thermal De-Consolidation of Thermoplastic Matrix Composites – II. Migration of Voids and Re-Consolidation. Composites Science and Technology 64 (2004), Issue 2, 191-202.

101. Wörz, K.: Simulation des Einflusses elektromagnetischer Felder auf die induktive Erwärmung von kohlenstofffaserverstärkten Kunstoffen. IVW-Bericht, Vol. 00-26. Kaiserslautern: Institut für Verbundwerkstoffe, 2000.

102. Bachofer, K.: LTB Bachofer GmbH & Co. KG, Personal communication, (2011).

103. Holmes, S. T.; Gillespie, J. W., Jr.: Thermal Analysis for Resistance Welding of Large-Scale Thermoplastic Composite Joints. Journal of Reinforced Plastics and Composites 12 (1993), Issue 6, 723-736.

104. Ageorges, C.; Lin, Y.; Mai, Y.-W.; Hou, M.: Characteristics of Resistance Welding of Lap Shear Coupons. Part II. Consolidation. Composites Part A: Applied Science and Manufacturing 29 (1998), Issue 8, 911-919.

105. Moser, L.; Mitschang, P.Schlarb, A. K.: Automated Welding of Complex Composite Structures; in: The 6th Asia-Australasian Conference on Composite Materials, Kumamoto, September 23-26, 2008.

9. Appendix

9.1. Induction Heating Model Validation

9.1.1. Single Sheet Induction Heating

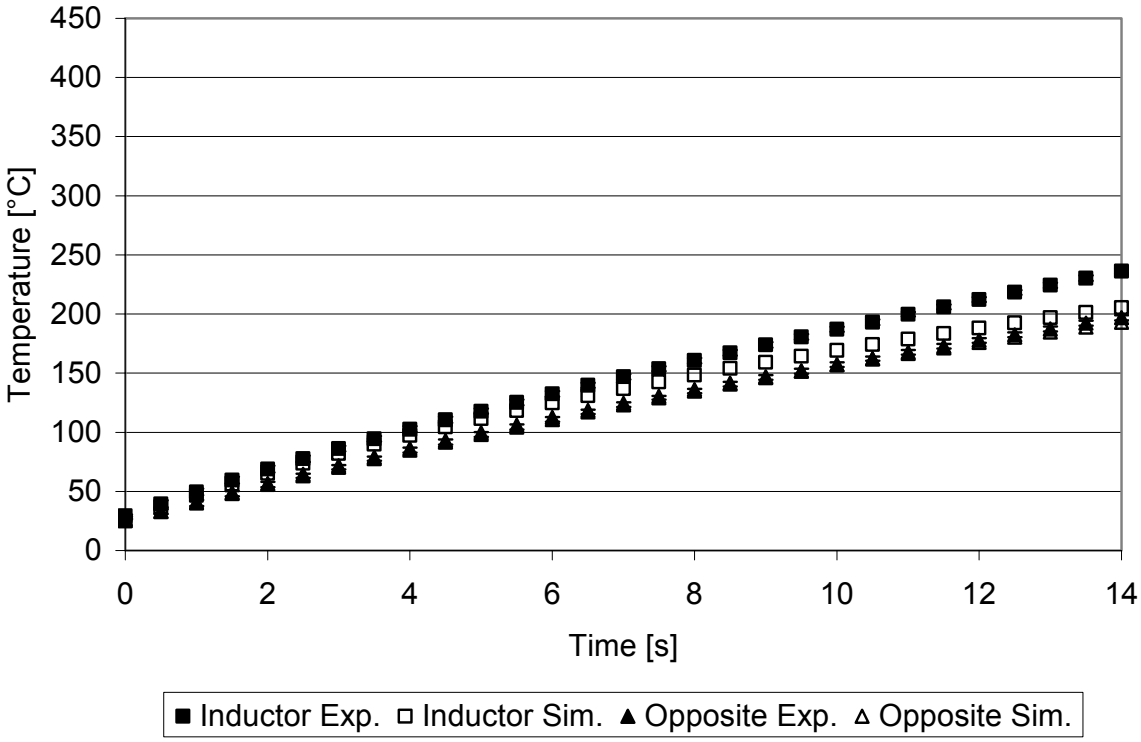

Figure 73: Validation of induction heating simulation, CF/PEEK, 3 mm coupling distance, 10 % generator power

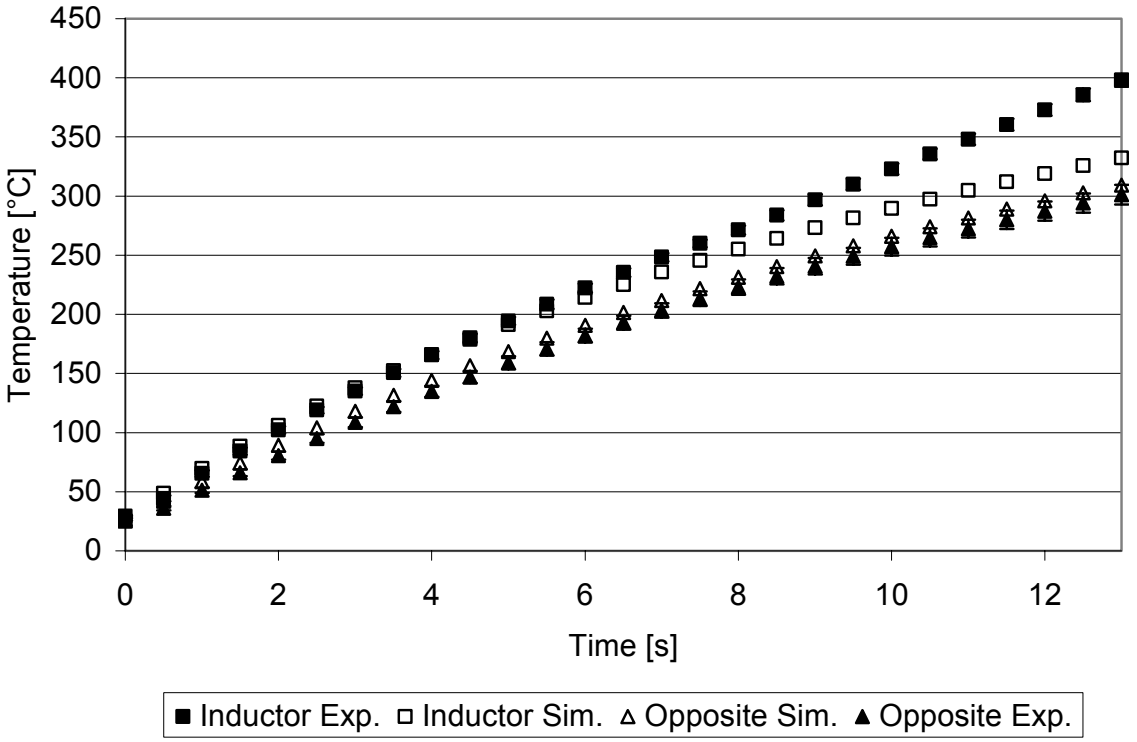

Figure 74: Validation of induction heating simulation, CF/PEEK, 3 mm coupling distance, 20 % generator power

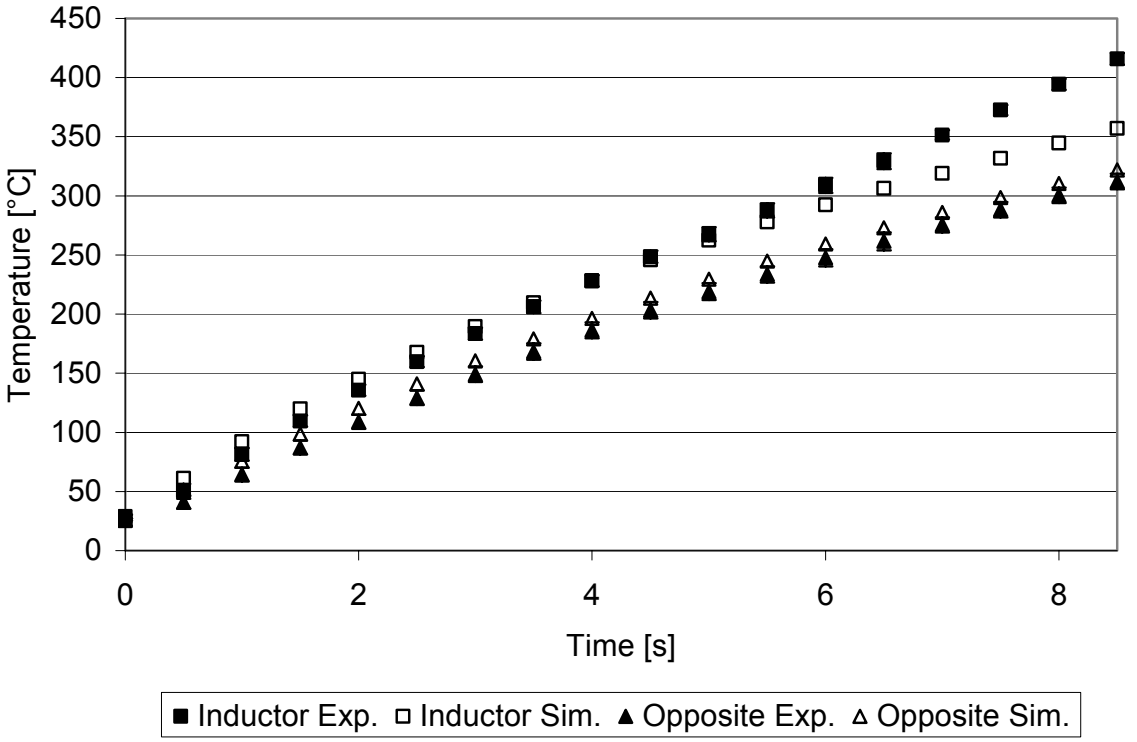

Figure 75: Validation of induction heating simulation, CF/PEEK, 3 mm coupling distance, 30 % generator power

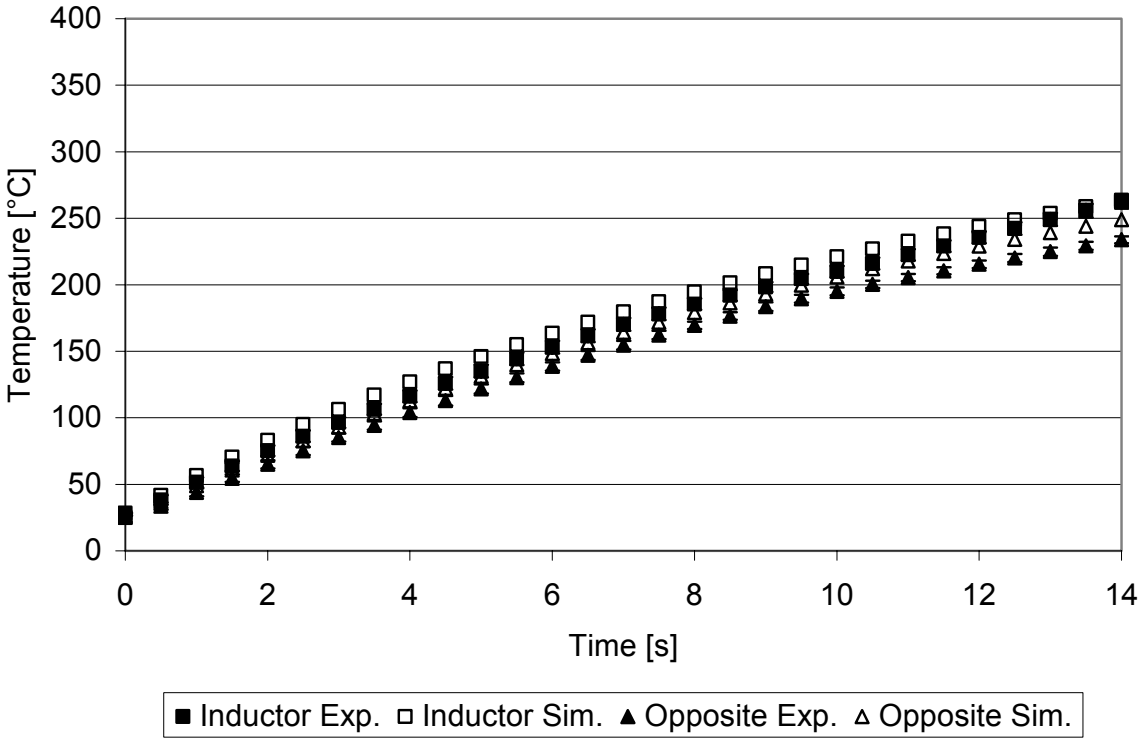

Figure 76: Validation of induction heating simulation, CF/ PPS, 2 mm coupling distance, 10 % generator power

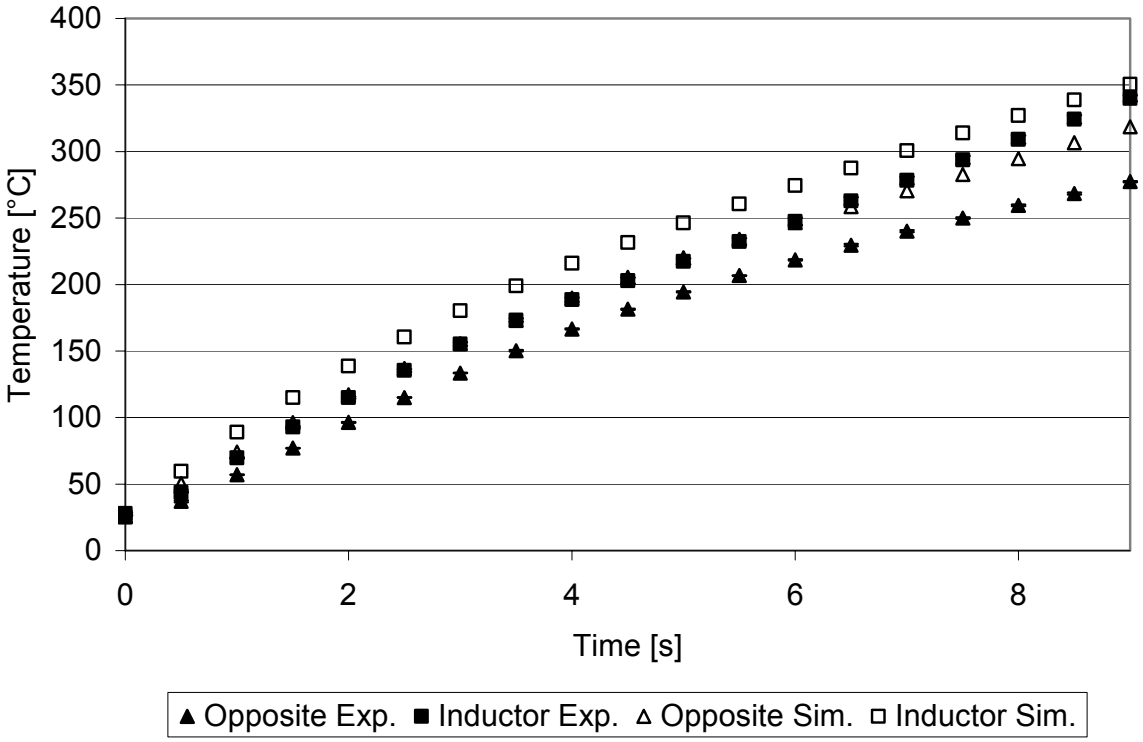

Figure 77: Validation of induction heating simulation, CF/ PPS, 2 mm coupling distance, 20 % generator power

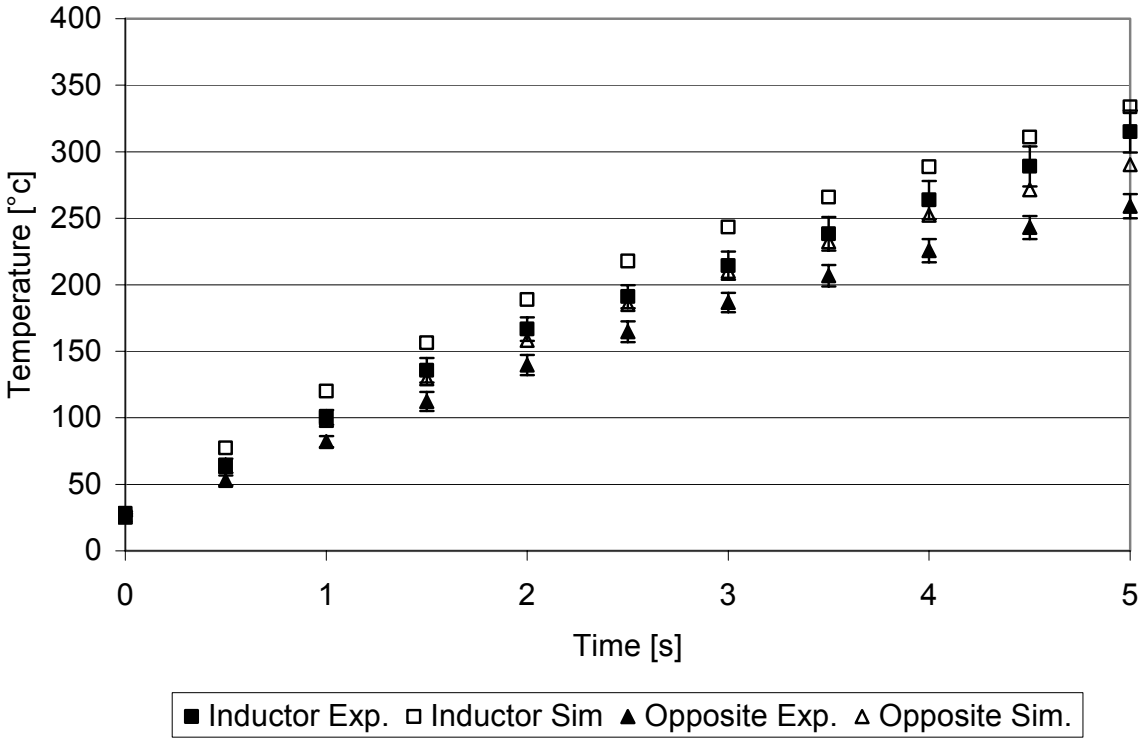

Figure 78: Validation of induction heating simulation, CF/ PPS, 2 mm coupling distance, 30 % generator power

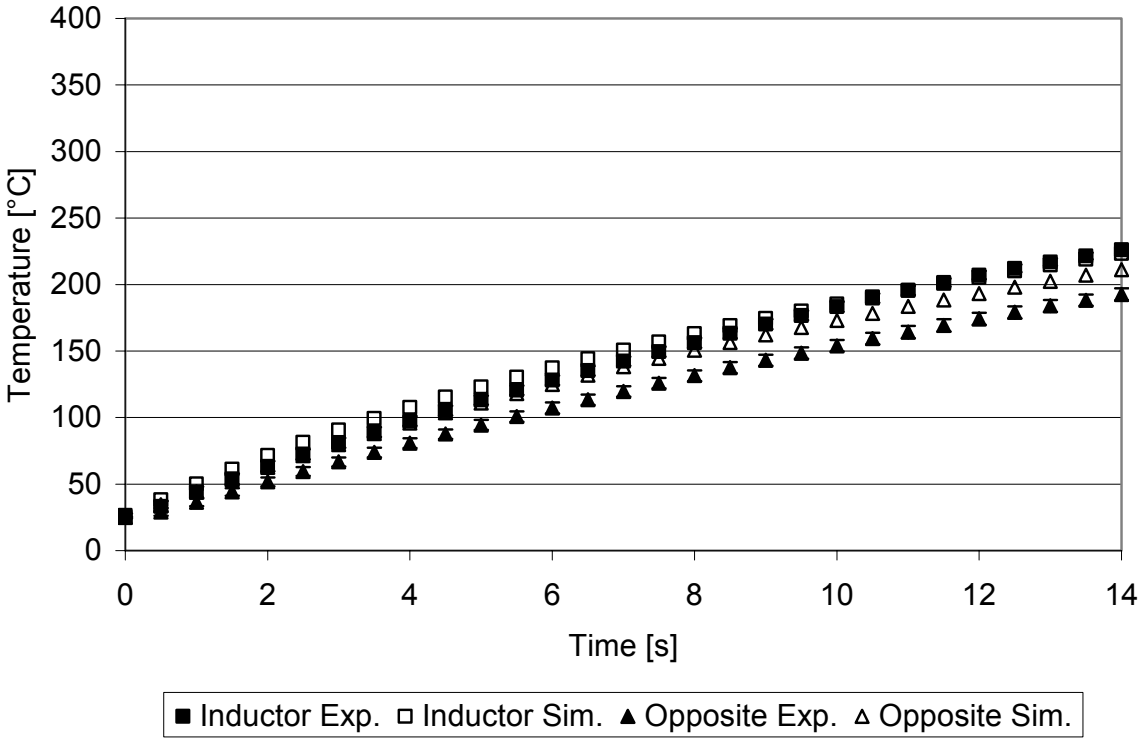

Figure 79: Validation of induction heating simulation, CF/ PPS, 3 mm coupling distance, 10 % generator power

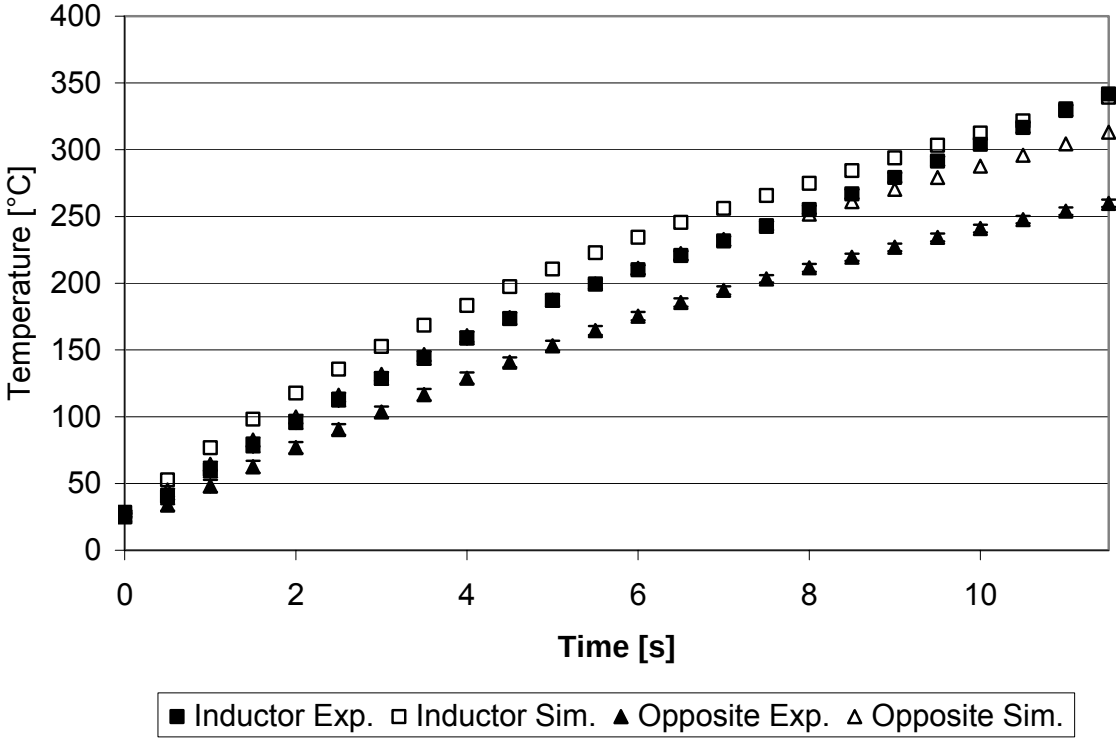

Figure 80: Validation of induction heating simulation, CF/ PPS, 3 mm coupling distance, 20 % generator power

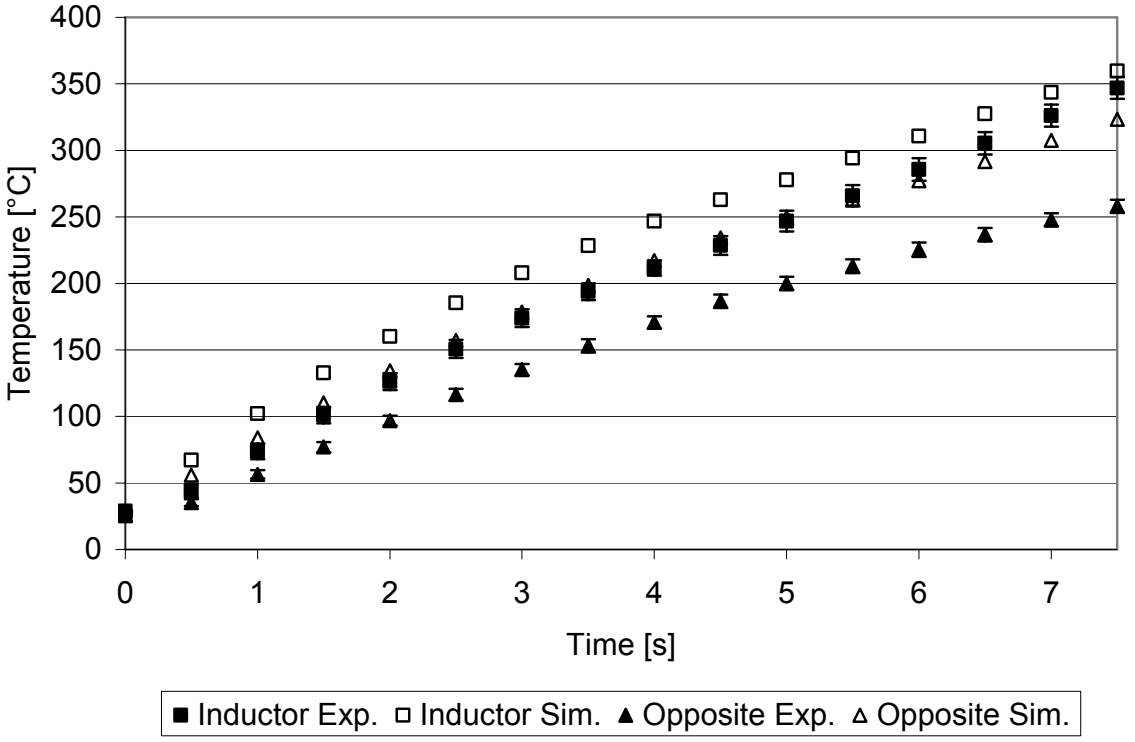

Figure 81: Validation of induction heating simulation, CF/ PPS, 3 mm coupling distance, 30 % generator power

Table 31: Comparison of heating patterns of experimental characterization and induction heating model, CF/PEEK, 3 mm coupling distance

Time [s]	Power [%]					
	10		20		30	
	Experiment	Model	Experiment	Model	Experiment	Model
2	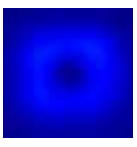	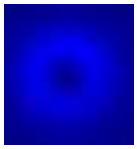	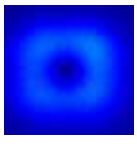	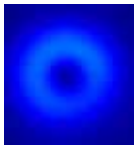	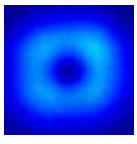	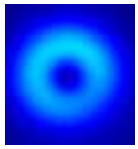
4	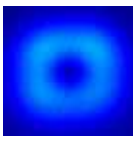	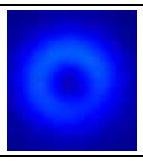	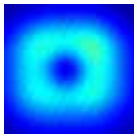	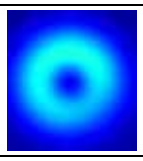	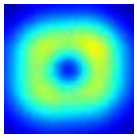	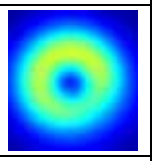
6	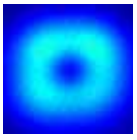	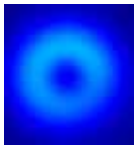	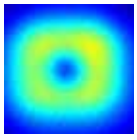	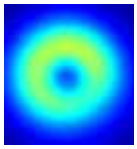	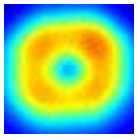	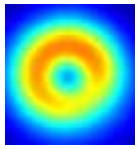
8	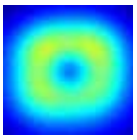	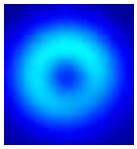	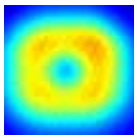	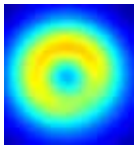	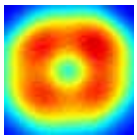	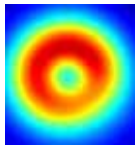
10	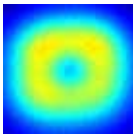	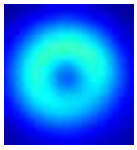	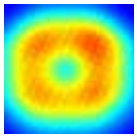	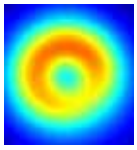		
12	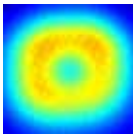	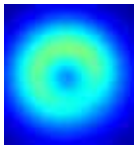	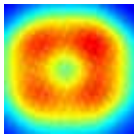	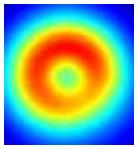		
14	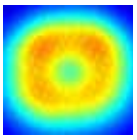	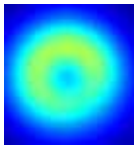	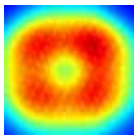	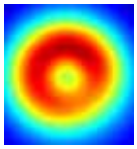		

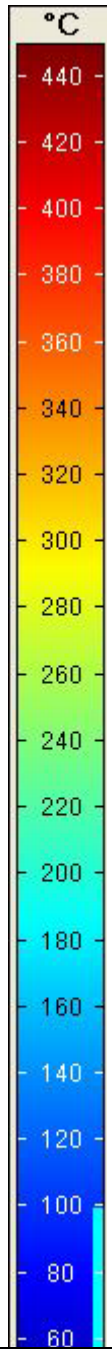

Table 32: Comparison of heating patterns of experimental characterization and induction heating model, CF/PPS, 2 mm coupling distance

Time [s]	Power [%]					
	10		20		30	
	Experiment	Model	Experiment	Model	Experiment	Model
2	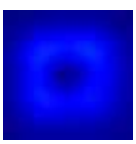	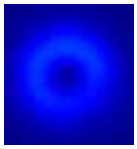	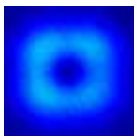	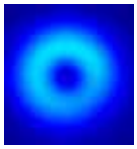	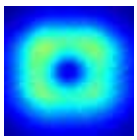	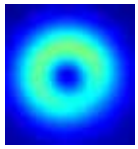
4	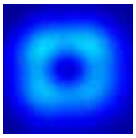	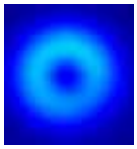	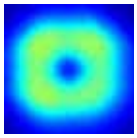	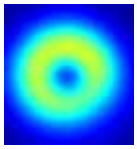	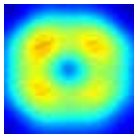	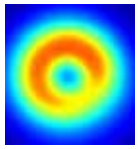
6	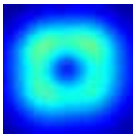	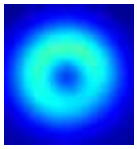	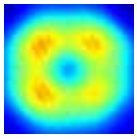	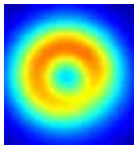		
8	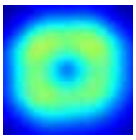	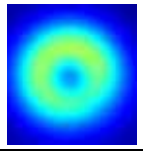				
10	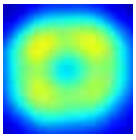	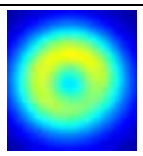				
12	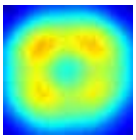	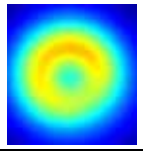				
14						

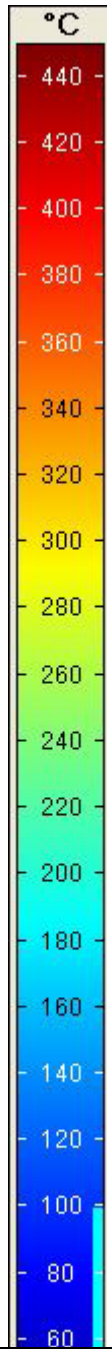

Table 33: Comparison of heating patterns of experimental characterization and induction heating model, CF/PPS, 3 mm coupling distance

Time [s]	Power [%]					
	10		20		30	
	Experiment	Model	Experiment	Model	Experiment	Model
2	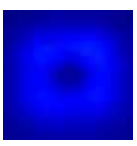	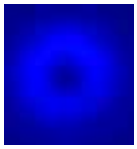	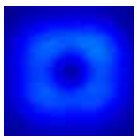	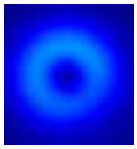	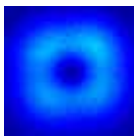	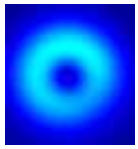
4	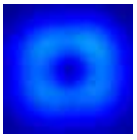	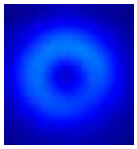	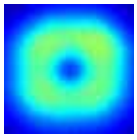	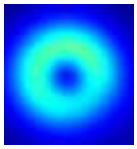	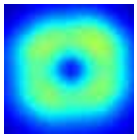	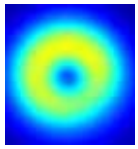
6	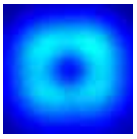	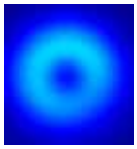	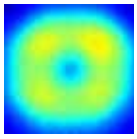	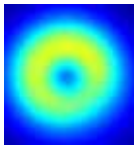	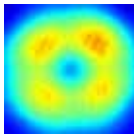	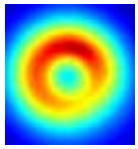
8	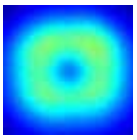	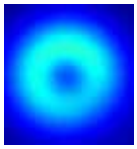	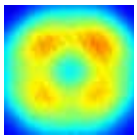	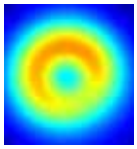	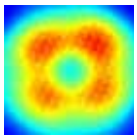	
10	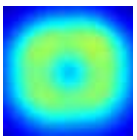	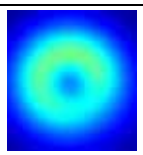	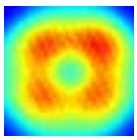	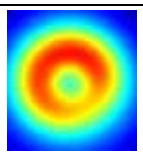		
12	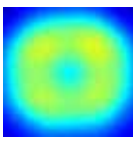	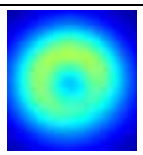				
14	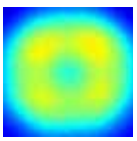	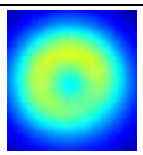				

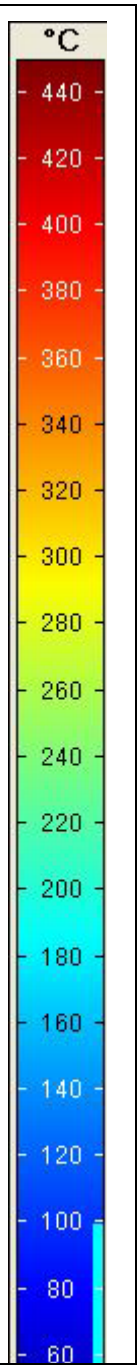

9.1.2. Single Sheet Induction Heating with Impinging Jet

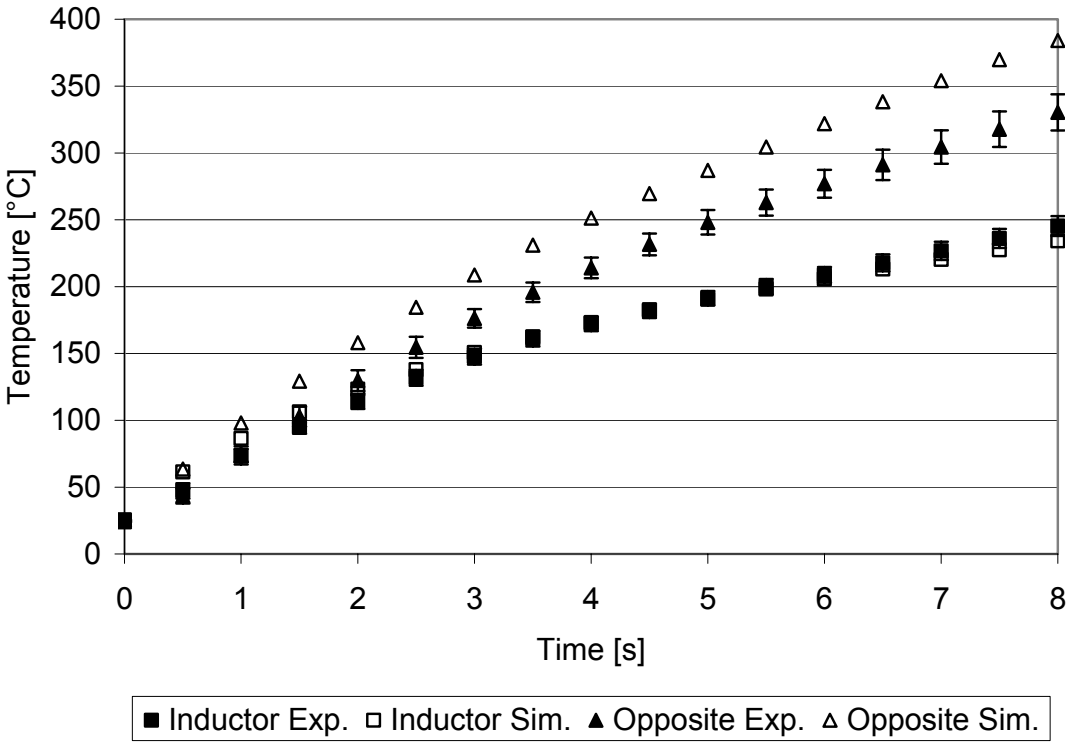

Figure 82: Validation of induction heating simulation with impinging jet, CF/PPS, 2 mm coupling distance, 30 % generator power, 304 l/min air volume flow

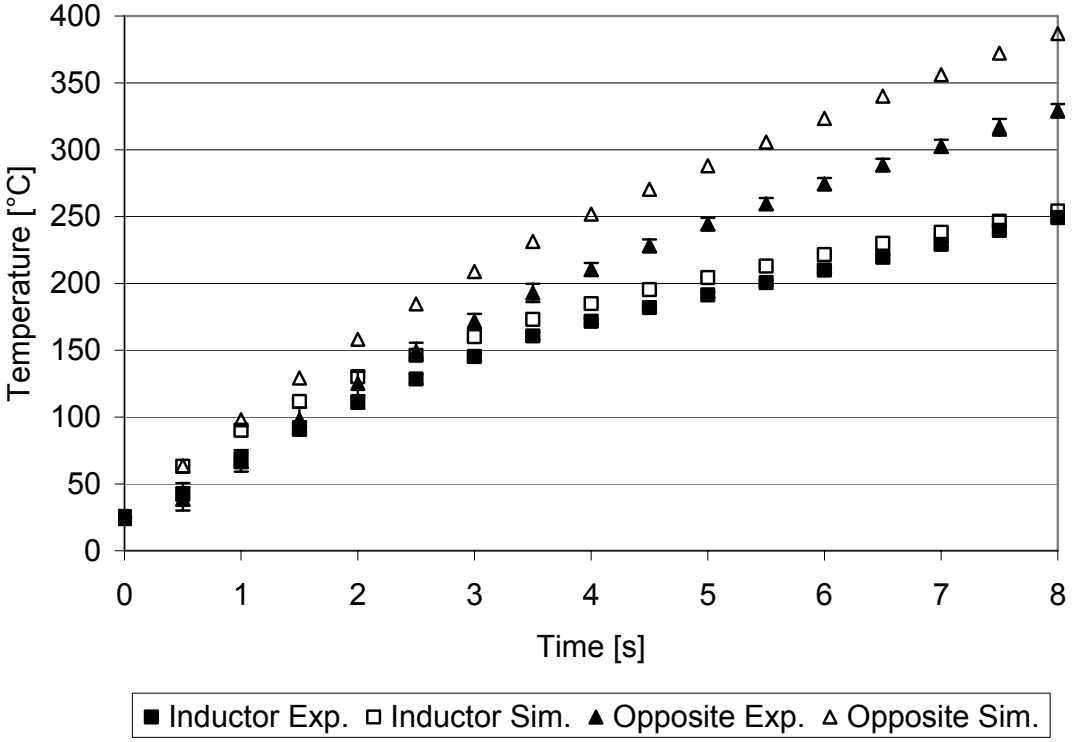

Figure 83: Validation of induction heating simulation with impinging jet, CF/PPS, 2 mm coupling distance, 30 % generator power, 240 l/min air volume flow

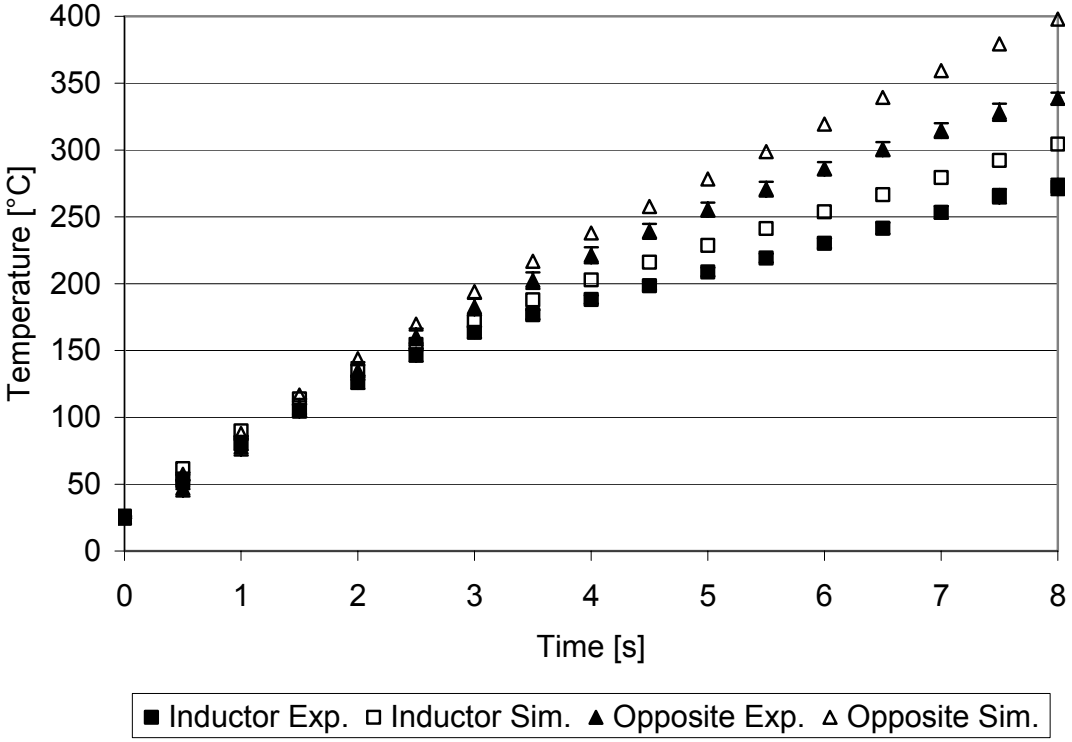

Figure 84: Validation of induction heating simulation with impinging jet, CF/PPS, 2 mm coupling distance, 30 % generator power, 167 l/min air volume flow

List of Supervised Student Research Projects

Timo Grieser, Analysis of inductive heating of carbon reinforced high performance polymer composites, 2010.

Jeffry Fransiskus Budiman, Analyse der thermischen Schädigung beim Induktionsschweißen von faserverstärkten PA6- und PPS-Laminaten, 2010.

Johannes Heyn, Finite-Elemente-Simulation der induktiven Erwärmung von Faser-Kunststoff-Verbunden, 2010.

Georgi Bonev, Finite-Elemente-Simulation der induktiven Erwärmung von Faser-Kunststoff-Verbunden, 2010.

Meng Guo, Modellbasierte Parameteroptimierung beim Induktionsschweißen von Faser-Kunststoff-Verbunden, 2010.

Sven Hennes, Konstruktion eines Haltearms für einen Induktor mit sechs Freiheitsgraden, 2010.

Andrea Ecker, Experimentelle Untersuchung und mechanische Charakterisierung von Nahttypen beim Induktionsschweißen von kohlenstofffaserverstärkten PPS-Laminaten, 2011.